ELECTRON EMISSION FROM FAST PROTON AND CARBON ION INTERACTIONS WITH GOLD NANOPARTICLES AND AMORPHOUS SOLID WATER

by

Wilson Hawkins

July 2021

Director of Dissertation: Jefferson L. Shinpaugh

Major Department: Physics

Widely used in the treatment of cancer, radiation therapy delivers a lethal dose of energy to malignant tissue. Modeling the deposition of energy in the interactions of the radiation with biological material is important to accurately predict the dosimetry and the subsequent biological outcomes. Recently, nanoparticles have been observed to increase the effective damage during radiation therapy. In this study, charged particle interactions with biological materials were studied to model energy deposition and electron transport, as well as a comparison study of fast ion interactions with gold nanoparticles acting as radiosensitizers.

Electron emission from metal and hydrated metal surfaces was measured for irradiation by protons and carbon ions in an energy range of maximum energy deposition, 1 to 6 MeV (near the so-called Bragg peak). Doubly differential electron emission yields were measured under ultra-high vacuum conditions using the spectroscopic technique time-of-flight analysis for low-energy electrons. This study included targets that are relevant for biological modeling, such as amorphous solid water, as well as for nanoparticle radiosensitizers, such as gold nanostructures, for which surface plasmon resonances have been proposed to contribute to the secondary electron emission.

The goal of our research group is to investigate charged particle interactions with

various biologically relevant targets applicable to the therapeutic treatment of malignancies. Monte Carlo electron transport codes use theoretical doubly differential cross sections, with respect to emission angle θ and electron energy ε, to model these interactions. In order to test and improve the Monte Carlo code, doubly differential electron yields from various solid state targets are measured experimentally in ultra-high vacuum conditions.

Previously, the time-of-flight electron detection method has been used to measure doubly differential electron yields from fast ion interactions with metallic, amorphous solid water, and hydrocarbon targets with high energy resolution at low electron energies (0.1 - 100 eV) [1–3]. This project has extended the energy range and complexity of the targets used to measure electron emission with high resolution by measuring doubly differential electron yields for proton and carbon ion beam interactions with gold foil, silicon-embedded gold nanoparticles, and thin gold nanoparticle films with and without amorphous solid water environments.

ELECTRON EMISSION FROM FAST PROTON AND CARBON ION INTERACTIONS WITH GOLD NANOPARTICLES AND AMORPHOUS SOLID WATER

A Dissertation
Presented to the Faculty of the Department of Physics
East Carolina University

In Partial Fulfillment of the Requirements for the Degree
Doctor of Philosophy in Biomedical Physics

by
Wilson Hawkins
July 2021

ELECTRON EMISSION FROM FAST PROTON AND CARBON ION INTERACTIONS WITH GOLD NANOPARTICLES AND AMORPHOUS SOLID WATER

by

Wilson Hawkins

APPROVED BY:

DIRECTOR OF
DISSERTATION: ______________________________
Jefferson Shinpaugh, PhD

COMMITTEE MEMBER: ______________________________
Michael Dingfelder, PhD

COMMITTEE MEMBER: ______________________________
Regina DeWitt, PhD

COMMITTEE MEMBER: ______________________________
Robert McLawhorn, PhD

COMMITTEE MEMBER: ______________________________
David Pravica, PhD

CHAIR OF THE
DEPARTMENT OF PHYSICS: ______________________________
Jefferson Shinpaugh, PhD

DEAN OF THE
GRADUATE SCHOOL: ______________________________
Paul J. Gemperline, PhD

ACKNOWLEDGEMENTS

I would like to thank Dr. Jefferson Shinpaugh for the tremendous amount of time and energy he has invested in my life. Without his expertise and vision, this project would have been impossible. His ability to manage the physics department, multiple research projects, and a half dozen graduate students all while finding the time to troubleshoot electronics, maintain funding, and invent creative techniques to solve highly specific problems in the lab is beyond commendable. His advice and guidance have been invaluable to my development as a scientist and a person.

Secondly, I want to thank my lab partner, roommate, and friend Dr. Eric Maertz. We spent years together in the trenches learning how to build, design, and operate atomic physics experiments. His attention to detail, organizational skills, and positive attitude contributed heavily to this work in ways that only I can fully appreciate. He offered invaluable support, motivation, and wisdom at critical moments in my life that made this accomplishment possible.

Lastly, I would like to thank the ECU staff William Holland, Gene Oakley, and Chris Bonnerup for their technical support. William's wealth of knowledge in modern electronics constantly proved invaluable in troubleshooting and designing custom electronics vital to data collection. Gene is a world-class machinist who fabricated a wide variety of custom high-precision beamline, chamber, and detector components. Chris's engineering expertise spans vacuum systems, beam optics, accelerator physics, and custom software development. Drinking coffee and exchanging banter early in the morning with Chris and Gene was the best part of every day working in the lab and will be sorely missed.

Contents

List of Tables

List of Figures

1 Introduction

The study of ionizing radiation and its effects on biological material is directly applicable to radiation therapy for the treatment of cancer. Half of all cancer patients' treatment plans involve the use of radiation therapy in conjunction with surgery, chemotherapy, and immunotherapy. X-rays are the most commonly used form of ionizing radiation in cancer treatment plans and have proven useful for suppressing tumor growth rates, extending patient survival times, and completely eliminating malignancies. The use of X-rays for radiation therapy dates back to 1899 after Dr. Wilhelm Roentgen (the first recipient of the Nobel Prize in Physics in 1901) gave his famous lecture "Concerning a New Kind of Ray". The use of protons for radiation therapy was proposed much later in 1946 by Robert Wilson [4]. Proton interactions with matter exhibited far less damage to healthy tissue along the path of the projectile while administering a large dose to the tumor deep within the tissue. The use of protons in cancer therapy was implemented for the first time in 1954 at the Lawrence Berkeley National Laboratory to treat a pituitary gland tumor. Decades later, carbon and other heavy ions were shown to be more efficient than protons in the killing of malignancies. In 1975, carbon ions were first used as ionizing radiation in the treatment of cancer at the Lawrence Berkeley National Laboratory. The United States pioneered the use of heavy ions in radiation therapy, but later abandoned this field due to the high cost of carbon and other heavy ion production facilities. In the early 1990's, both Germany and Japan revived the use of carbon ion radiation therapy, building new treatment facilities and serving as the world's leaders in carbon ion therapy research [5, 6].

To complement clinical, in vivo, and in vitro studies, biomedical physicists perform fundamental atomic physics measurements and simulations of secondary electron emission. Secondary electron emission is known to be the dominant contributing factor in energy deposition caused by ionizing radiation. Interaction cross sections for the probability of secondary electron emission in ion-atom collisions can be measured using low-density gas targets. These cross section measurements can be used to model energy deposition in simulations. Modifications to theoretical models of ion interactions with matter give insight into the fundamental processes involved in radiation therapy and help model the dosimetry in treatment planning.

As theoretical models have advanced to incorporate more complex target environments like water and DNA, interaction cross sections for condensed matter targets are desired for model improvement. Interaction cross section data from solid targets is unobtainable due to high target density and complexity. Instead, electron yield measurements have been used for comparison to simulation outputs as a way to test theoretical models. Proton interactions with gas [7–12], metallic [1, 3, 13–30], and non-metallic targets [1–3, 8, 19, 23, 31–38], have been studied for comparisons to theoretical models. Carbon ion interactions with metallic and non-metallic targets have been studied and these measurements are important for modeling the dosimetry, but are less available [16, 25, 27, 33, 39].

During the course of this work, an ultra-high vacuum chamber and ajoining time-of-flight data analysis system, previously employed by Dr. Robert McLawhorn in the Kansas State University J. R. Macdonald Accelerator Laboratory, was rebuilt and updated in the East Carolina University Accelerator Laboratory. Doubly differential electron yields from condensed phase targets relevant to theraputic applications were measured to establish a catalog of experimental results to be used for direct comparison to simulation. A new beam pulser was designed and custom-built in-house, utilizing workshop and expert staff resources in the ECU department of physics. Electron emission measurements from 1, 2, and 4 MeV proton interactions with gold foil and amorphous solid water were measured to expand the energy range of previously measured 2 MeV proton on gold foil experiments performed by Dr. Robert McLawhorn. Doubly differential electron yields from 0.2 MeV/AMU and 0.5 MeV/AMU carbon ion interactions with gold foil and amorphous solid water were measured in order to improve dosimetry modeling for heavy ion therapy in the Bragg peak energy range. Due to the recent interest in gold nanoparticles used as radiosensitizers in radiation therapy, doubly differential electron yields from proton and carbon ion interactions with silicon-embedded gold nanoparticles and thin gold nanoparticle film.

1.1 Ionizing Radiation

The majority of energy deposition from ionizing radiation interacting with matter occurs in the form of ionization and excitation of target atom electrons by incident projectiles. Electrons liberated through ionization are referred to as secondary electrons and will continue to travel through the medium causing a cascade of further ionization and excitation until reaching a thermal energy. The vast majority of the secondary electrons generated by ion interactions are in the low energy range of 0 - 100 eV and are primarily responsible for the total dose delivered to a target volume.

One of the tools used for modeling energy deposition by ions is Monte Carlo track structure code. Step by step tracking of secondary electrons and subsequent ionizations and excitations due to coulombic interactions are simulated by random number generation and piecewise cross section functions. A visual output form a track structure simulation for various ions traveling through water is shown in Fig.1 [40]. As the ions in this simulation traveled through the water environment, ionizations, auto-ionizations, and excitations generated secondary electrons, most of which were low energy electrons with very short ranges. Some of these secondary electrons were given a large amount of energy from the simulated incident projectile to create long trails, or tracks, of successive ionization, auto-ionization, and excitation electron events shown as various colored spheres. The number of secondary electrons N_e generated by fast ions passing through matter is given by

$$N_e = N_p n L \sigma \tag{1}$$

where N_p is the number of incident projectiles, n is the target particle density, L is the projectile path length for a given volumetric region of interest, and σ is the cross section, or probability of secondary electron production. This cross section σ increases with atomic number Z and can be seen in Fig.1, as the heavy ion projectile (bottom left) generated far more secondary electrons than the proton projectile (bottom right).

1.1.1 Biological Effects

Secondary electron production from ion interactions with matter not only scales with atomic number Z, but is also highly energy dependent. Secondary electron emission rates from X-ray interactions with matter decays exponentially with distance traveled in the target material. Secondary electron emission rates from ion interactions with matter increase dramatically near the end of their track (0.2 MeV/AMU). This phenomenon was discovered by W.H. Bragg and formally became known as the Bragg peak. Bragg made early measurements of this characteristic spectrum using alpha particles produced by a radium salt source in an ionization chamber in 1904 [41]. This increased electron emission at the end of fast ion tracks is typically analyzed by calculating dose

$$D = \frac{E_A}{m}, \tag{2}$$

or the absorbed energy E_A per unit mass m in a target volume. Dose is typically measured in joules per kilogram, or gray (Gy). Dose distributions of the Bragg peaks produced by a variety of ions interacting with matter have been measured extensively since this discovery [42]. Dose-depth curves for X-rays, protons, and carbon ions traveling through tissue are shown in Fig.2. In order to deliver a lethal dose of radiation to a tumor using X-rays, a large amount of dose will be delivered to healthy cells along the entrance path. Dose to this same healthy tissue is also inevitable for proton and carbon ion irradiation, but is substantially less. Additional dose delivered to healthy tissue after the tumor cite by X-rays, referred to as the exit dose, is not shown in Fig.2. Proton and carbon ion radiation give very little exit dose, negligible in comparison to X-rays. This significant difference in damage to healthy tissue is the main reason ion therapy, although much more expensive to provide, has proven to be more effective in treatment. When comparing proton dose to carbon ion dose, it can be noted that carbon ions deposit less dose on the entrance path, in general, but deliver more exit dose past the tumor site.

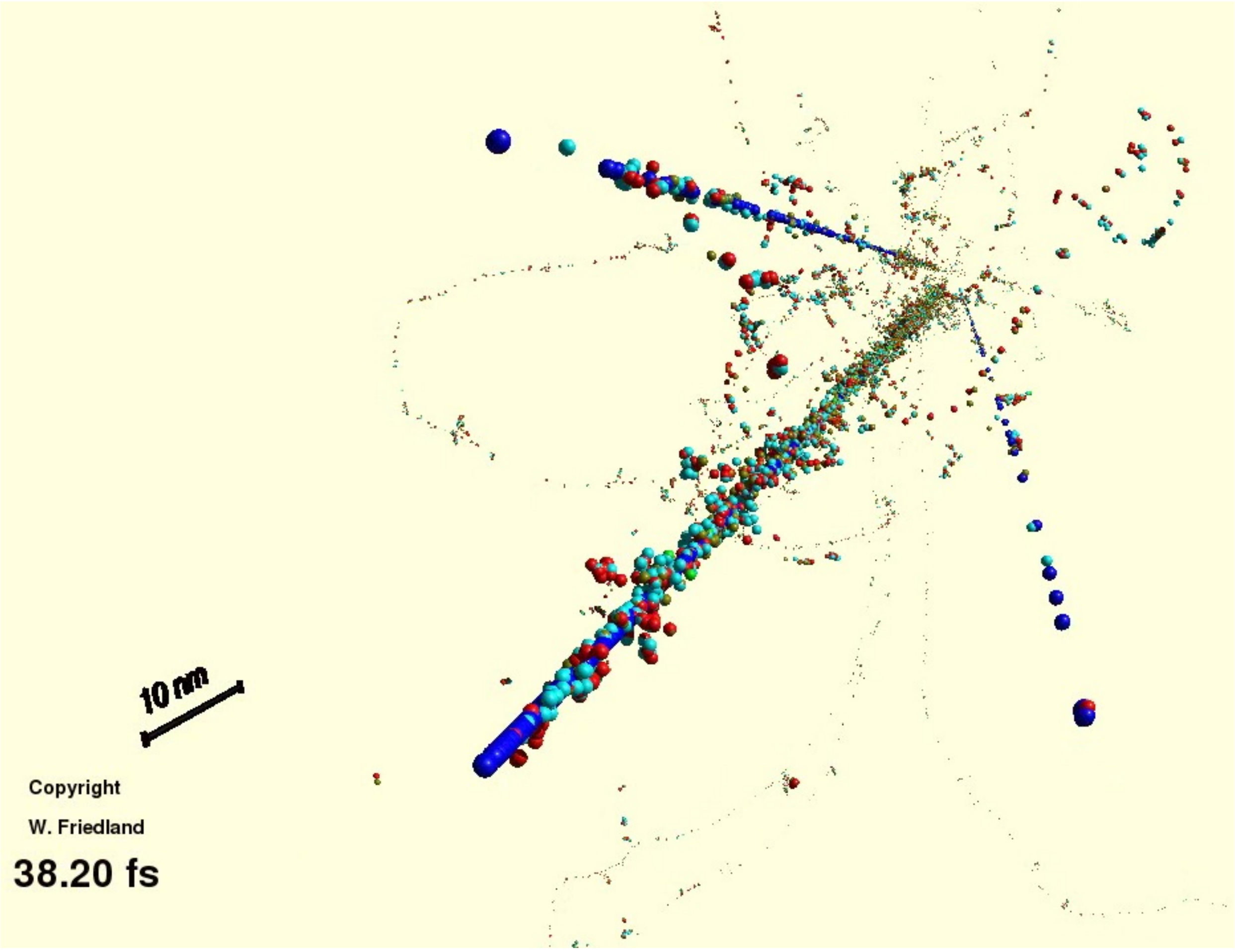

Figure 1: Electron track structure Monte Carlo simulation for a high energy hydrogen ion (bottom right), helium ion (top left) and sodium ion (bottom left) traveling through a water environment. This image shows the recorded events from 38 fs of travel time. Each ionization or excitation event caused by a secondary electron emission is marked by a colored sphere. Low energy electrons are the most common and have short tracks that end near the incident ion. Less common high energy electron emissions leave behind a long trail of excitation and ionization event markers. [40].

Relative biological effectiveness

$$RBE = \frac{D_I}{D_X} \tag{3}$$

is the ratio of X-ray dose D_X to ion therapy dose D_I that produces the same biological effects. These biological effects are generally measured through in vitro cell survival studies which account for cell death from physical processes like single and double strand DNA breaks from secondary electron collisions and chemical processes including free radical production from the ionization of water molecules. Interrupting the cell cycle though necrosis or inducing cell apoptosis through direct DNA damage are the main causes of cell death in ionizing radiation studies. For proton therapy, an accepted RBE value of 1.1 in the Bragg peak region has been used for decades, but new studies are challenging this approximation by considering dose dependency on RBE for proton therapy. When comparing effective cell killing for in vitro studies, an increasing RBE from 1.15 to 1.4 has been measured in the 2 - 0 Gy region, which occurs in the distal tail of an ion's track in the tumor region of interest [43–45].

1.1.2 Clinical Applications

Techniques for treating malignancies with ion therapy have been practiced since the 1950s and have proven more effective at delivering lethal dose to malignancies while preserving healthy tissue than X-ray therapy [46]. At the time of this publication, 96 proton therapy centers were active worldwide with over 225,000 total patients treated as of December 2019 [6]. These proton therapy centers were located in Austria (1), Belgium (1), China (2), Czech Republic (1), Denmark (1), England (5), France (3), Germany (5), India (1), Italy (3), Japan (18), Poland (1), Russia (5), South Korea (2), Spain (2), Sweden (1), Taiwan (2), The Netherlands (3), and the United States (41). There were 12 active carbon ion therapy centers at the time of this work with over 34,000 total patients treated worldwide as of December 2019 [6]. These carbon ion therapy centers were located in Austria (1), China

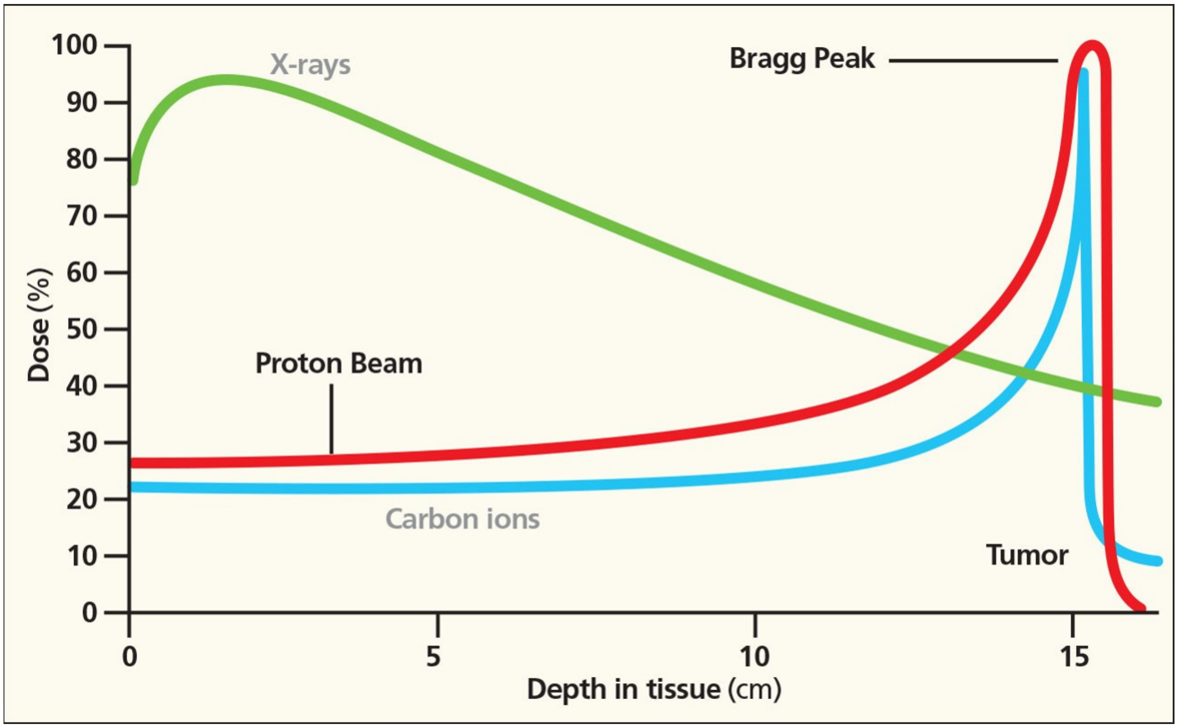

Figure 2: Comparison of the dose-depth relationship for photon, protons, and carbon ions in tissue. [47]

(2), Germany (2), Italy (1), and Japan (6).

Proton therapy has been used to treat a wide variety of cancer types, mainly in cases where tumor location relative to sensitive organs requires increased dose delivery precision. A illustration of a dose delivery treatment plan simulation for the treatment of prostate cancer with proton therapy is shown in Fig.3. In this treatment plan, proton beams are scanned over multiple entrance angles to deliver an integral lethal dose to the tumor site. When compared to the X-ray treatment plan, far less healthy tissue is exposed to ionizing radiation as the high dose at the end of the proton beam track allows for fewer entrance angles and the Bragg peak nature of proton therapy offers little to no exit dose. Carbon ion therapy is less common in practice than proton therapy due to cost, but is becoming cheaper and more readily available. Carbon ion therapy clinical trials and patient records have been accumulating and have shown increased malignant cell killing efficiency with less negative symptoms in patients.

Clinical trials have been done for carbon ion therapy showing high 5-year survival rates and low toxicity for the treatment of prostate, head, neck, lung, liver, bone, and soft tissue, rectal, and pancreatic cancers when compared to standard X-ray therapy [48–50]. Carbon ion therapy has been shown to be just as effective as proton therapy in the treatment of prostate cancer with half the total therapy sessions, or fractionations, at the same total tumor dose. A lethal dose to prostate cancer is typically delivered in 32 fractions over 8 weeks for proton therapy and 20 fractions over 5 weeks for carbon ion therapy. A recent clinical trial of over 700 patients who received carbon ion therapy for prostate cancer over a 5 year period showed significantly less genitourinary toxicity with equal 5-year survival rates from 57.6 Gy treatment plans of 16 fractions over 4 weeks compared to 63.0 Gy treatment plans of 20 fractions over 5 weeks [51]. A new clinical trial is currently being done to test the efficacy of 51.6 Gy treatment plans over only 12 fractionations with expectations of further lowering toxicity and improving patient quality of life while maintaining 5-year survival rates comparable to previous treatment plans.

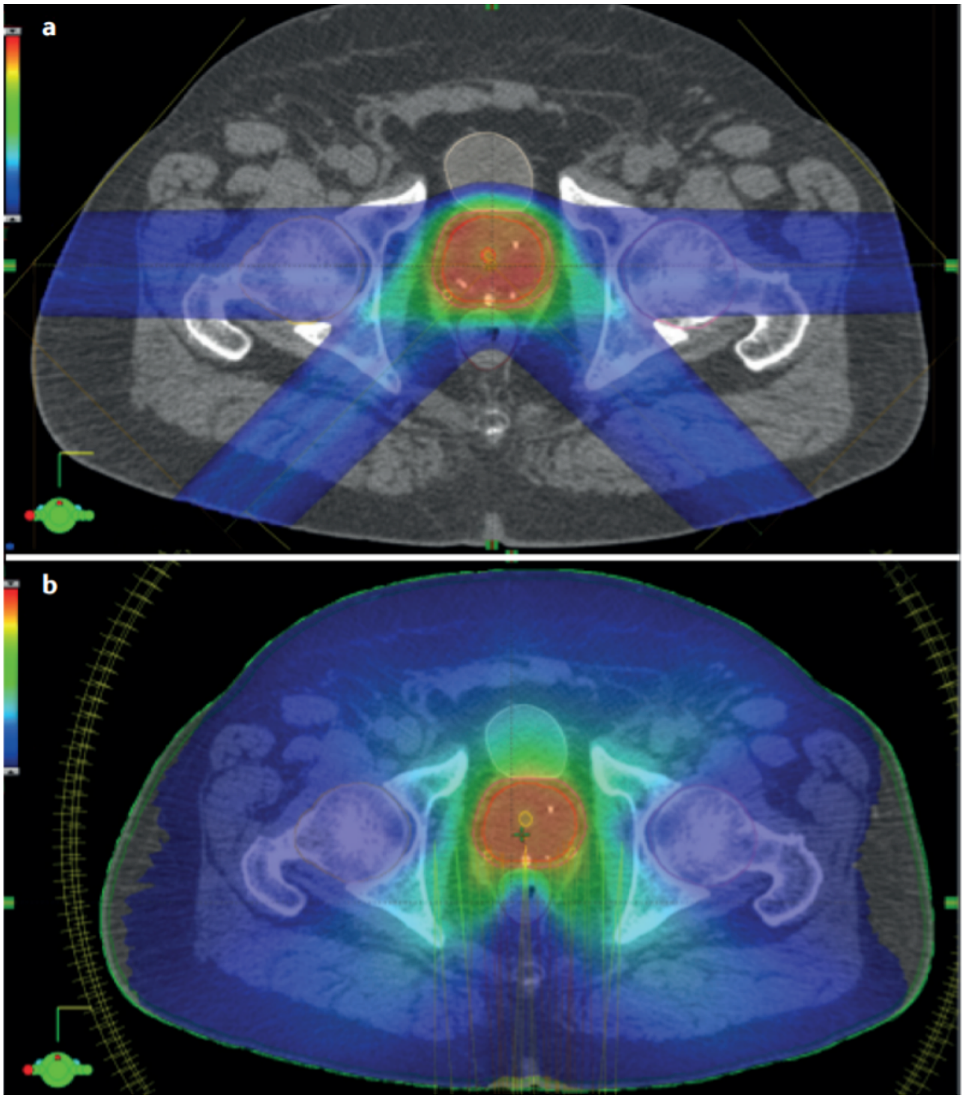

Figure 3: Dose distributions of 40 Gy to the prostate gland by proton (a) and X-ray (b) therapy. In both cases, multiple beams were used at various angles to administer an integrated dose. This figure illustrates the lessening of dose to healthy tissue due to the Bragg peak efficacy and lack of exit dose [52].

1.1.3 Gold Nanoparticles as Radiosensitizers

GNPs are ideal radiosensitizers as they can be manufactured with size distribution in the 1-150 nm range [53–55]. Nanoparticles of this size are excellent for passive uptake at specific tumor sites due to their low permeability to normal healthy tissue but high permeability to locally damaged capillaries surrounding tumors [56–58]. As a high-Z material, GNPs have high photoelectric and secondary electron emission probabilities. This physical dose enhancement is complemented by the large surface area to volume ratio available for coatings of targeting proteins used to enhance cellular uptake [59–61]. A diagram of this GNP coating cellular uptake process is shown in Fig.4 [62].

In vitro studies for X-ray irradiation of immortalized cell lines in the presence of glucose and citarte coated GNPs (16 - 50 nm) have shown significant cell survival fraction reduction for cancer cells [63–66]. In vivo studies on the radiosensitization of various coating GNPs (2 - 50 nm) during X-ray irradiation has shown delay in tumor growth and increased long-term specimen survival when compared to treatments of equal dose [64, 67, 68]. At the time of this writing, in vitro studies on the cell survival of immortalized human cells in the presence of coated GNPs under proton and carbon ion irradiation were in progress in the ECU Accelerator Laboratory. These studies aim to compare similar dose rates, total local dose, and GNP concentration effects to similar X-ray irradiation measurements.

1.2 Ion Induced Electron Emission from Solids

Experimentally measuring secondary electron emission in solids requires several considerations. Unlike gas targets, the target density is high, so the ability to know if an electron emitted from the surface of a target was produced by the incident projectile or a secondary electron from an ionization or excitation event of the incident projectile is impossible. For this reason, cross sections cannot be measured for ion interactions with solid targets. In modeling biological systems, theoretical cross sections must then be used in simulations. So instead of cross section measurements, electron yield measurements are made to compare to

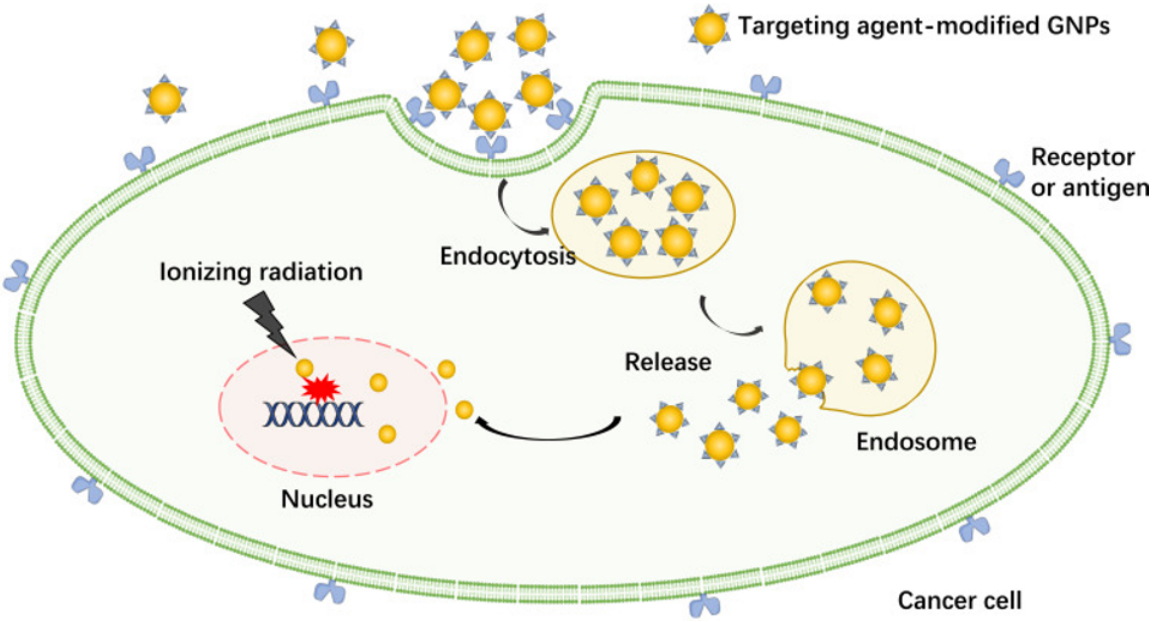

Figure 4: Coatings on GNPs both reduce toxicity and posess targeting proteins used to enhance cellular uptake through endocytosis, enhancing DNA damage from short range secondary electron emission [62].

the electron yield outputs of Monte Carlo models.

In order to understand electron yield measurements, a series of fundamental physical quantities must be defined. Stopping power

$$S = -\frac{dE}{dx} \tag{4}$$

is defined as the energy loss per unit length of a particle traveling through matter. The range

$$R = \int_0^{E_0} \frac{1}{S} dE \tag{5}$$

of such a particle is given by integrating the reciprocal stopping power over energy, where E_0 is the initial kinetic energy of the particle. This understanding of particle range in matter involves a "continuously slowing down approximation" where the stopping power is assumed to be a continuous function of energy. This is not always the case, as most ion-material interactions show high energy dependence in stopping power [69]. A large catalog of various stopping power measurements have been made over the last century and are available in a database with accompanying extrapolation code, named The Stopping and Range of Ions in Matter (SRIM), provided by Ziegler [70–72]. With these two concepts, a wide array of predictions were made including the need for thin target foils on the order of 1 μm to allow the passage of ions in the low energy ($<$ 6 MeV) range used in this investigation.

In order to escape the surface of a solid, electrons must overcome a surface barrier potential

$$U = E_F + \Phi \tag{6}$$

where E_F is the Fermi energy of the conduction band (1 - 15 eV) and Φ is the work function of the material (4 - 6 eV). Therefore, the energy of an electron emitted from the surface of a solid target must be

$$\varepsilon = \varepsilon_i - U \tag{7}$$

where ε_i is the initial energy of the electron before overcoming the surface barrier potential. The probability of electron escape from the surface of a solid can be expressed as

$$P(\varepsilon) = 1 - \frac{U}{\varepsilon_i}. \tag{8}$$

1.2.1 Total Electron Yields

Total electron yield

$$\gamma = \frac{N_e}{N_p} \tag{9}$$

from ion interactions with solid-state materials is the total number of electrons N_e emitted per incident ion projectile N_p. Total electron yield should be formally defined as the sum,

$$\gamma = \gamma_B + \gamma_F, \tag{10}$$

of backward yield γ_B and forward yield γ_F. The total electron yield from ion interactions with solids depend heavily on both the projectile and target material. These dependencies are given by

$$\gamma = \frac{PL}{2I} S \tag{11}$$

where P is the probability of escape, discussed previously, L is the mean free path of the electron, I is the ionization potential of target electrons, and S is the stopping power. Total electron yield is typically written as

$$\gamma = \Lambda S \tag{12}$$

where Λ was known as the "material parameter" in atomic physics until recently. Measurements of total yields for 10 keV - 24 MeV proton interactions with various thin metallic foils were made by Hasselkamp et al. in 1986 and are shown in Fig.5 [22]. Further measurements from higher Z ion projectiles have been made, showing an additional projectile dependence on Λ. This "gamma factor" has been shown to decrease with high Z projectiles [15, 73].

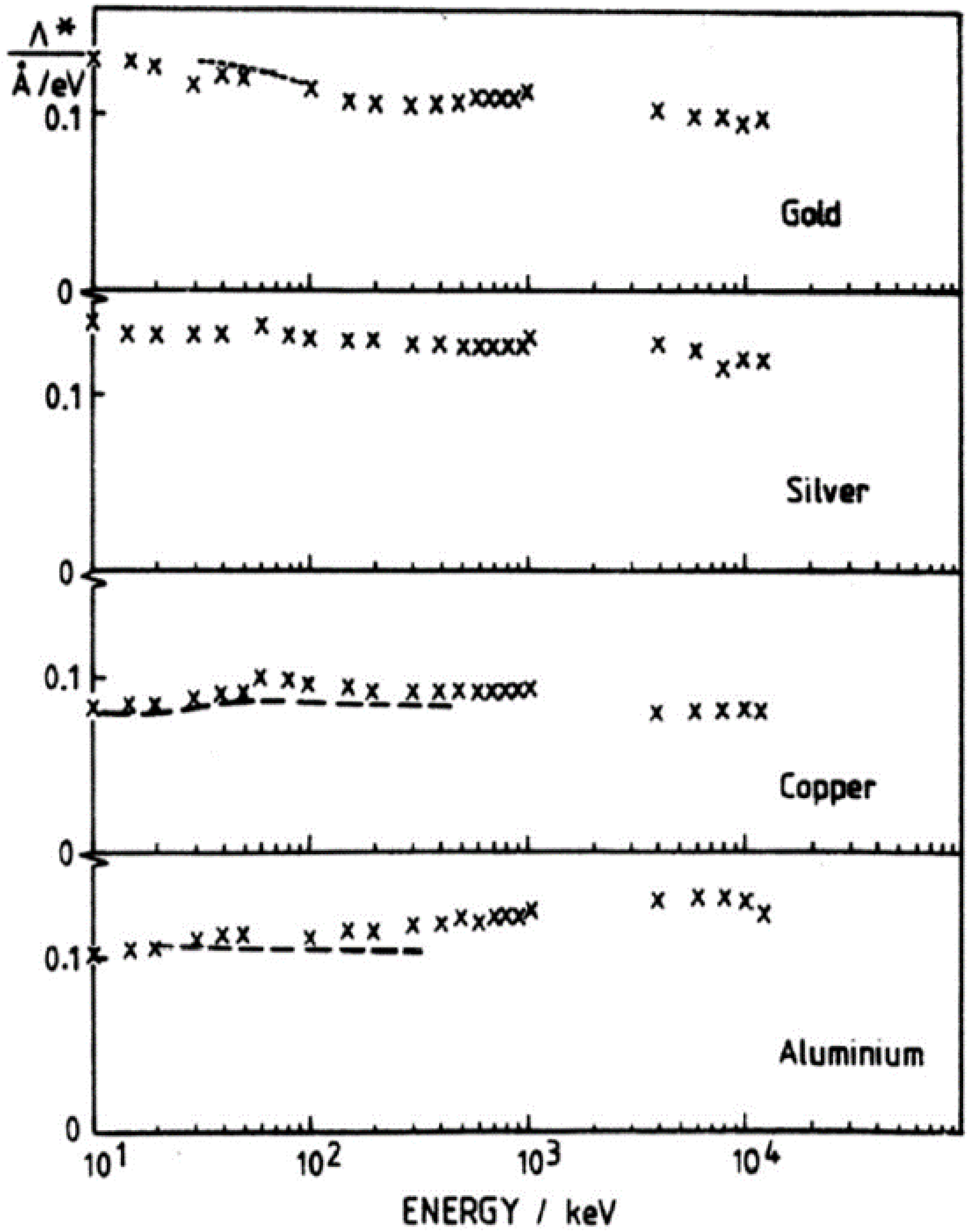

Figure 5: Total electron yields from 10 keV - 10 MeV proton interactions with Au, Ag, Cu, and Al foils. [22].

1.2.2 Singly Differential Electron Yields

Beyond total accumulated charge methods of measuring total electron yields form ion interactions with solids, measurements can be made showing the energy and angular distribution of electron emission. Measurements of these isolated parameters in the total electron emission spectrum is referred to as differential yields. The differential of total electron yields in energy $d\gamma/d\varepsilon$ or angle $d\gamma/d\theta$ can be written as $\gamma(\varepsilon)$ and $\gamma(\theta)$ respectively and are both referred to as singly differential electron yields. The angle θ here is with reference to the projectile direction of motion. Making singly differential electron yield measurements further probes the fundamental nature of spatial and energetic

structure of electron emission useful for understanding track structure and dose distributions.

Singly differential electron yields with respect to energy $\gamma(\varepsilon)$ are highly dependent on projectile type and energy, as well as target material. With careful consideration of surface contamination attenuation effects and energy loss from the surface barrier potential, this method of measurement provides critical insight into the abundance of low energy ($<$ 100 eV) electrons primarily responsible for DNA damage during ion therapy. Typical $\gamma(\varepsilon)$ measurements are found from backward scattered electron emission, as only sufficiently thin targets produce forwards scattered electrons. A plot of backward scattered singly differential electron yields $\gamma(\varepsilon)$, showing target material and projectile energy dependence, is shown in Fig.6.

1.2.3 Doubly Differential Electron Yields

Electron yields differential in both energy ε and angle θ are referred to as doubly differential electron yields $d\gamma/(d\varepsilon d\theta)$, typically written as $\gamma(\varepsilon, \theta)$. These spectra are the most informative in studying the electron emission from ion interactions. Structure can be seen in these spectra from various electromagnetic and quantum mechanical processes occurring in the coulombic interactions between projectiles and target electrons. An instructive

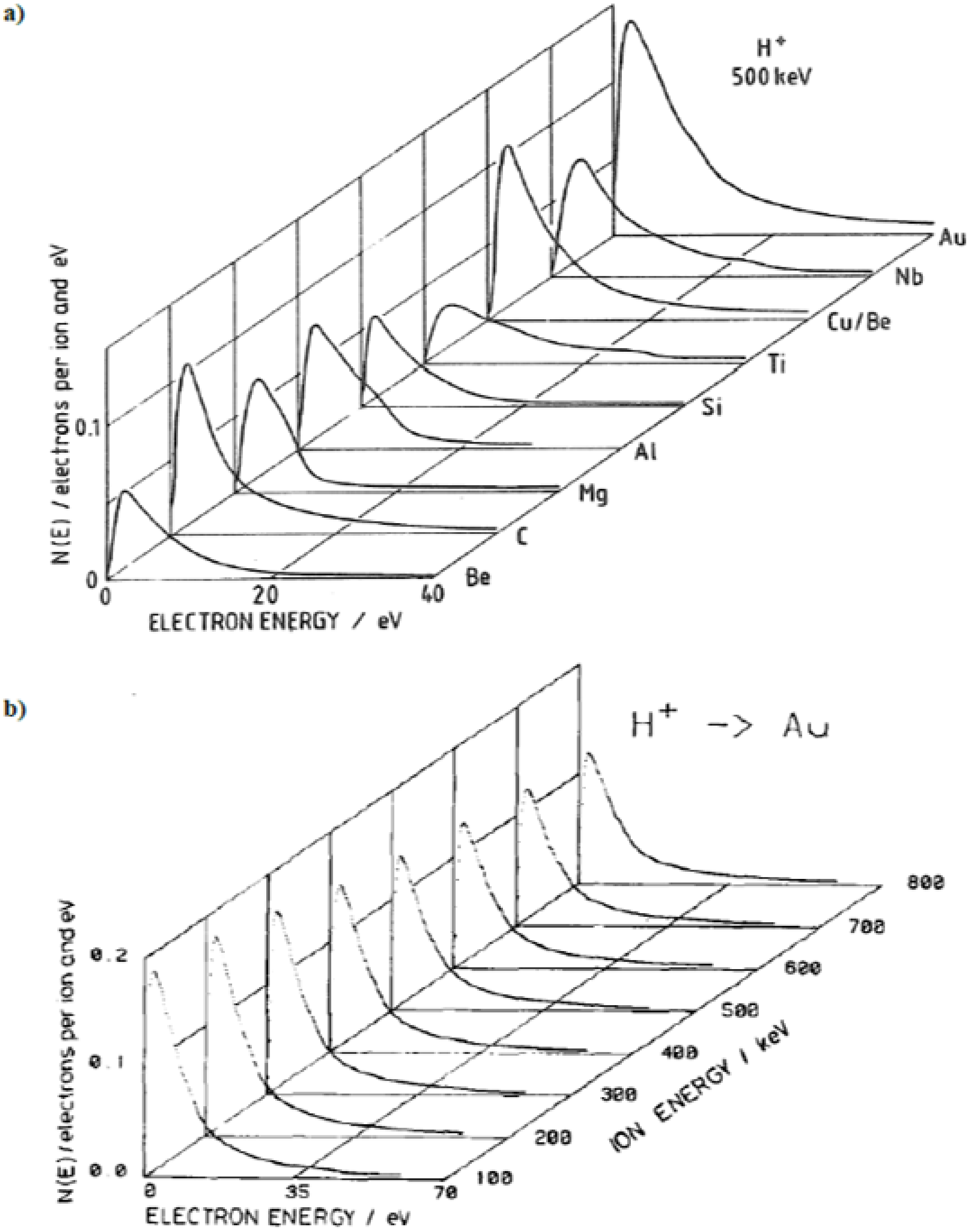

Figure 6: Singly differential electron yields $\gamma(\varepsilon)$ from (a) 500 keV proton interactions with clean metallic foils, as well as singly differential electron yields $\gamma(\varepsilon)$ from (b) 100 - 800 keV proton interactions with clean Au foil. [22].

plot of various spectral structure found in doubly differential electron yields, adapted from Frischkorn et al is shown in Fig.7 [74]. This figure, log-log scaled intensity vs. electron velocity, shows common structure found in forward scattered doubly differential electron yield spectra at 0 degrees and other forward angles. Characteristic peaks are shown from Auger electron production from both the projectile and target atom electron shell vacancy filling after ionization. These Auger electron peaks from the projectiles and target materials are predictable because energy gaps between electron shells in atoms are discrete and unique. An electron peak of "convoy" electrons will appear on doubly differential electron yield spectra where, through a charge exchange into a continuum state, ionized electrons pass through the target material with positively charged projectile ions at the projectile velocity. Electrons emitted as a result of elastic collisions with incident projectiles are forward-scattered with a velocity twice that of the incident projectile through momentum exchange. These binary encounter electrons will be discussed later in this publication and will dominate the forward scattered doubly differential electron yield spectra for this investigation.

Doubly differential electron yields from 1.2 MeV proton interactions with carbon foil at 0 degrees, made by Rothard et al, is shown in Fig.8 [73]. This plot, scaled by electron energy, shows a specific example of the generic plot previously discussed. Carbon target Auger electron, binary encounter electron, and convoy electron peaks are shown, as well as the location of the plasmon decay peak. A plasmon is a cascade, or wave, of nearly free electrons acting as an electron gas generated by an excitation process described by the dielectric response theory. This wave of electrons has a frequency

$$\omega_{plasmon} = \sqrt{\frac{n_e e^2}{m_e \epsilon_0}} \tag{13}$$

where n_e is electron density, e is electron charge, m_e is electron mass, and ϵ_0 is the permittivity of free space. The corresponding energy of this electron wave is given by

$$E_{plasmon} = \hbar\omega_{plasmon}. \tag{14}$$

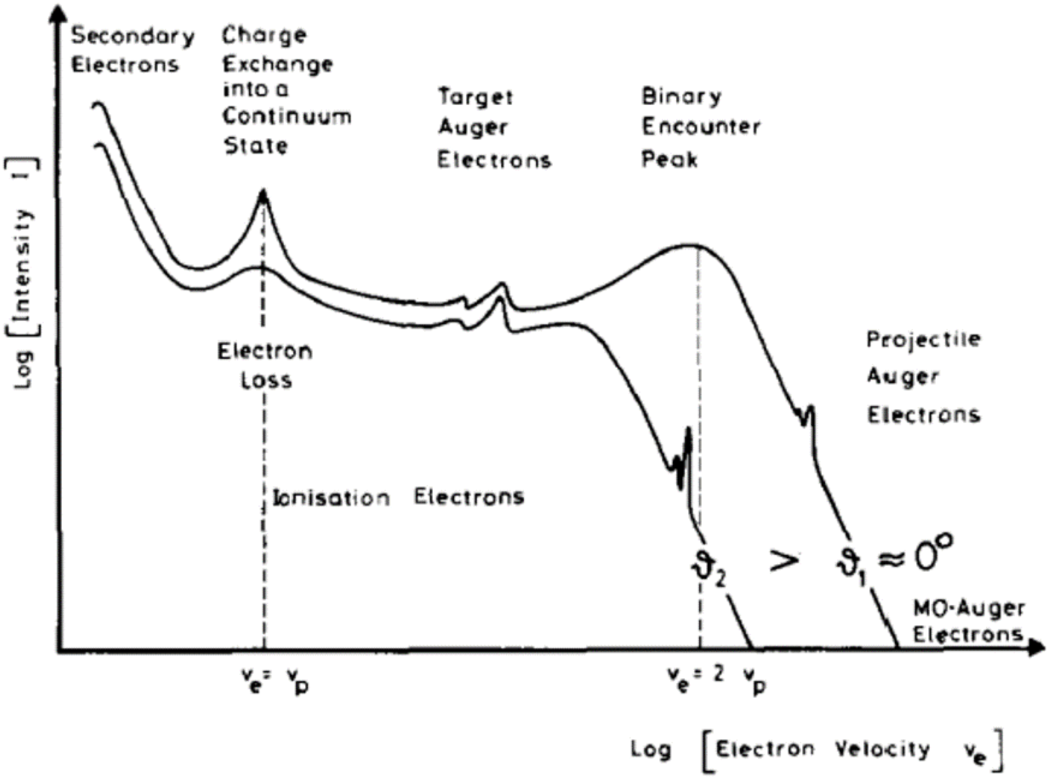

Figure 7: Generic instructive diagram of doubly differential electron yields $\gamma(\varepsilon, \theta)$ spectra features at 0 degrees and an arbitrary angle between 0 and 90 degrees from the incident projectile, adapted from Frischkorn et al [74].

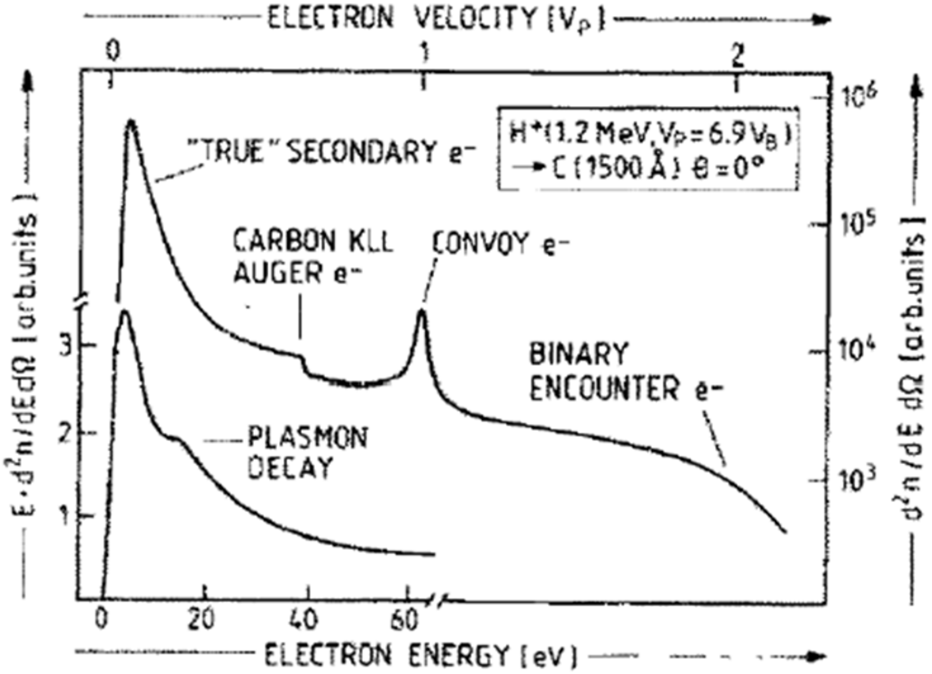

Figure 8: Doubly differential electron yields $\gamma(\varepsilon, \theta)$ from 1.2 MeV proton interactions with clean carbon foil adapted from Rothard et al [73].

2 Materials and Methods

The experimental results for this work were obtained in the East Carolina University Accelerator Laboratory (ECUAL) under the supervision of Dr. Jefferson Shinpaugh. The ECUAL utilizes a National Electrostatics Corporation (NEC) 2 MV Tandem Pelletron Accelerator to produce fast ions of various species and charge states [75]. Proton and carbon ion beam was created using a cesium ion sputter source designed by Middleton et al [76]. Electron yields were measured in an ultra-high vacuum (UHV) chamber equipped with electrostatic detectors designed for time-of-flight (TOF) analysis. Supporting vacuum technology, beam manipulation equipment, electronics systems, and data acquisition software were used in collaboration throughout the accelerator system to maintain adequate pressure and beam stability necessary for this work. In addition, the ECU department of physics hosts a staff of technical support including a machine shop, electronics shop, and engineering lab capable of fabricating custom hardware and software.

2.1 Ion Source

The ion source used to generate ion beam for this project was a cesium ion sputter source designed by Roy Middleton [76]. A diagram of this ion source is shown in Fig.9. A reservoir of cesium was heated to vapor form at roughly 100°C. The cesium gas was injected into the center of a tantalum ionizer coil, heated to approximately 1200°C, which phase-changed the cesium vapor into Cs^+ plasma. This positively charged plasma was attracted to the negatively biased cathode assembly. A diagram of the cathode target is shown in Fig.10. The cathode was packed with a target powder capable of generating a wide range of ions at various beam currents. Titanium hydride and graphite powders were selected for H^- and C^- ion production respectively. A plot of typical H^- production by a titanium hydride packed cathode over time is shown in Fig.11. The desired charge-to-mass ratio ion beam produced by this ion source was selected via an inflection magnet before injection into the accelerator.

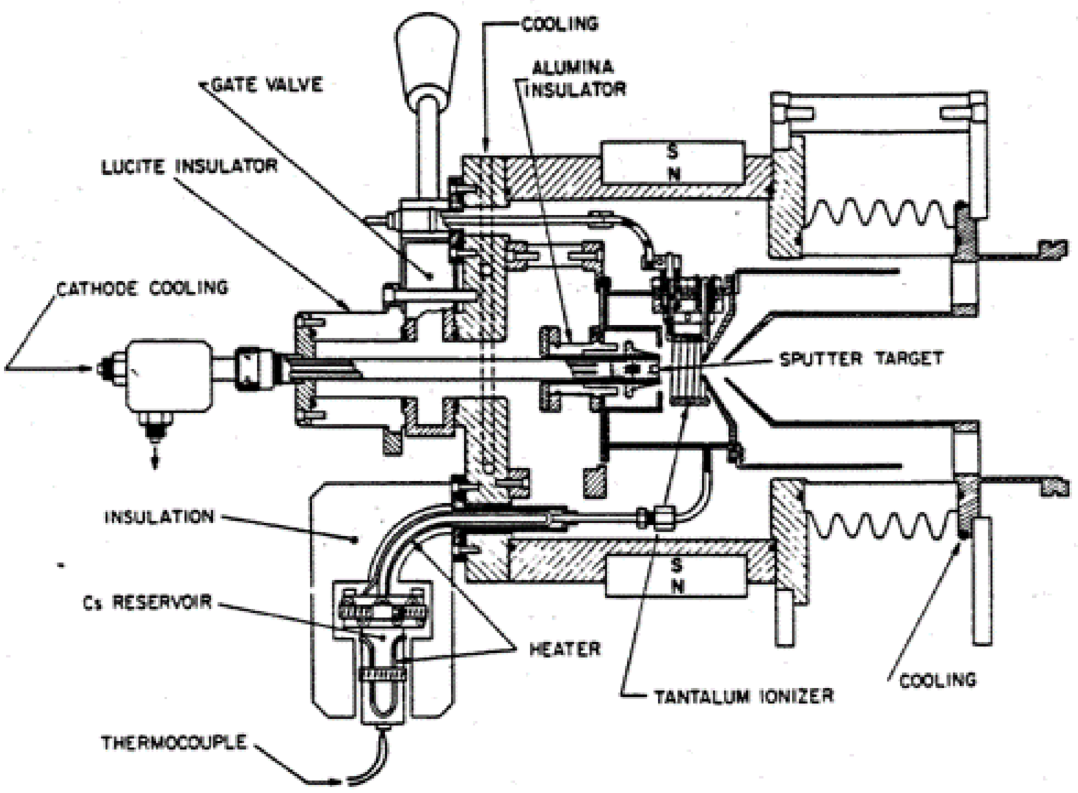

Figure 9: Diagrammatic display of the cesium ion sputter source used to produce ion beam. Cesium gas is generated in the cesium oven, transferred to the sputter target, and phase shifted into plasma via proximity to the 1000°C tantalum ionizer. The resulting ion beam is accelerated to the right [76].

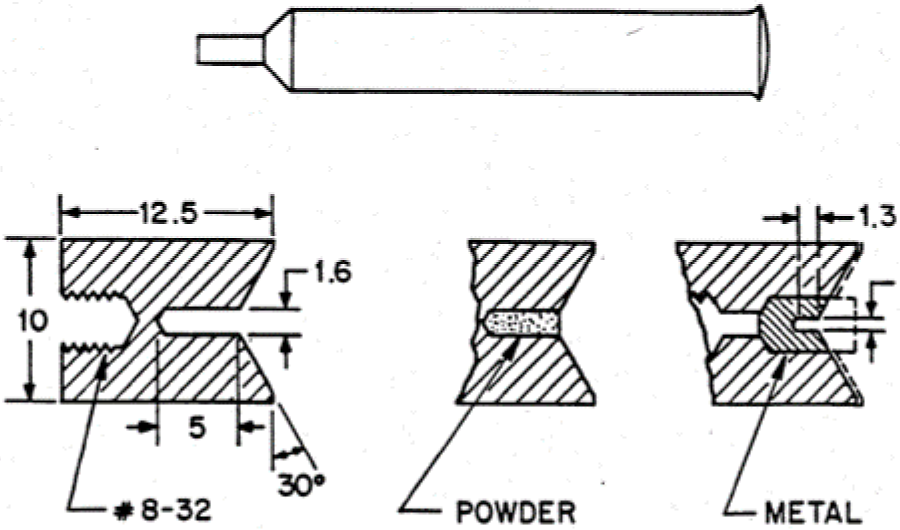

Figure 10: Cathode assembly used in ion sputter source, labeled as "sputter target" in Fig.9. The aluminum or copper cylinder has a powder-filled cavity that when sputtered generates a variety of ions [76].

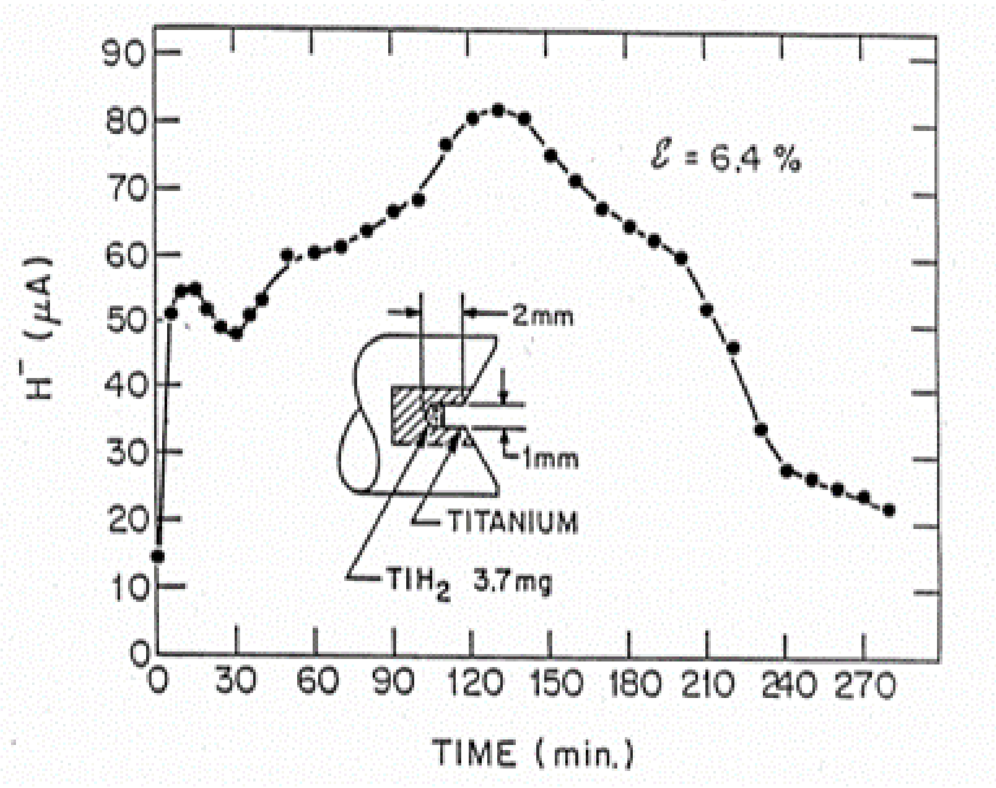

Figure 11: Expected beam output over time for titanium hydride cathode target [76].

The middleton design used for this sputter ion source utilizes a coiled cylindrical heating element coated in tantalum, referred to here simply as the ionizer. A cross-sectional diagram of the ionizer, designed by HeatWave Labs, is shown in Fig.12. The ionizer requires a high-vacuum environment to achieve operational current and temperature. In practice, the ionizer current must be ramped up and down slowly to avoid compromising material integrity. For this reason, the ionizer is the primary component considered when designing both start-up and shut down procedures. Typical operating conditions of the ionizer are 21 A, 200 W at 1200°C. This high temperature is necessary to phase shift the injected cesium gas into plasma. The positively charged cesium nuclei within the plasma are accelerated towards the cathode and sputter ions off the surface of the cathode powder reservoir.

Prior to ion source operation, several safety procedures are required by the ECUAL laboratory safety plan. For radiation safety, the ECUAL is equipped with a LUDLUM model 375 Area Monitor positioned above the central terminal with an alarm threshold of 0.5 mR/hr. Before starting the ion source, a Cs-137 standard source of activity 5 μCi is used to test the survey meter alarm. For electrical safety, a grounded shorting rod was attached to the ion source at all times when not in operation. Removing the shorting rod from the ion source allows for high voltages of up to 10 kV to be applied, but presents an electrical hazard. To protect the operators, a cage was installed around the source with two access panels, equipped with electrical interlocks. The access panel interlocks must be closed for the high voltage power supplies to operate. An additional power supply interlock was located outside of the ion source cage, requiring a key kept under the supervision of ECU Accelerator Engineering.

Visual inspections of ion source ancillary equipment were required prior to operation. The beamline gate valve between the low energy beamline and accelerator remained closed until the ion source reached operational parameters. A low energy beamline pressure of less than 1 μTorr was verified prior to operation for optimal beam conditions and ionizer integrity.

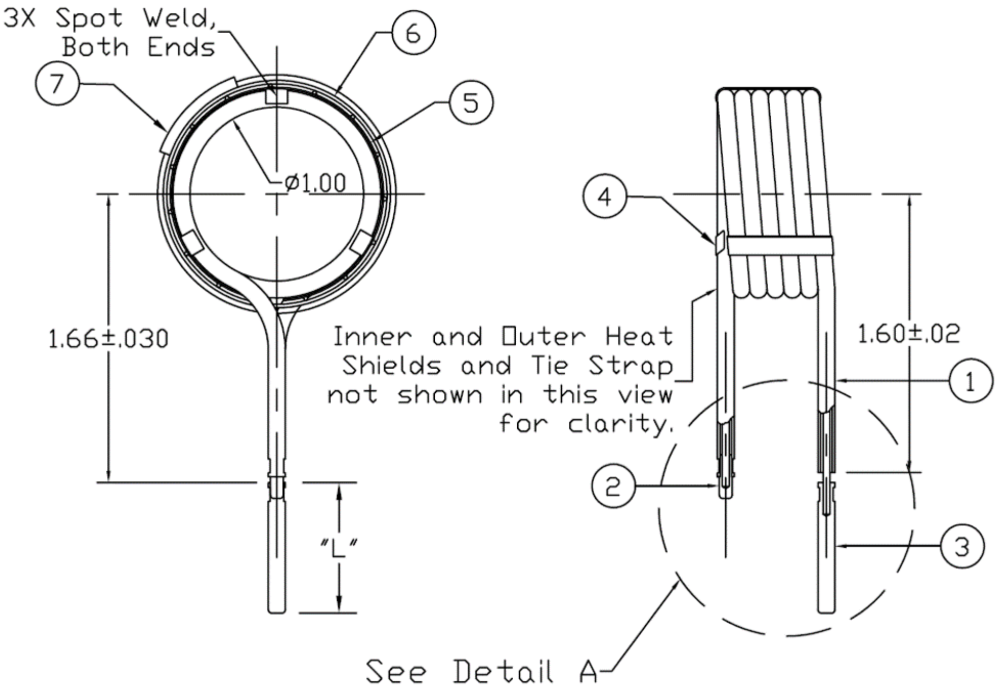

Figure 12: Diagram of the ionizer used to generate cesium plasma, provided by HeatWave Labs.

A Thermo Fisher NESLAB chiller circulated ethylene glycol and water through the cathode assembly to maintain thermal stability. The NESLAB chiller was equipped with a flow meter and thermometer to monitor circulation and operating temperature. An operating temperature of the coolant was verified to be less than or equal to 20°C. A Faraday cup located on the low energy beamline was inserted to measure beam current and act as a beam stop during low energy beam optimization.

The ion source power supplies were set to operational values in a time-sensitive chronological order. The various power supply connections for the ion source are shown in Fig.13 The extraction accelerating column positioned post ion source and pre-inflection magnet was first set to 30 kV to clear the ion source of sputtered beam and provide enhanced beam focusing for low energy optimization. The inflection magnet current was then set to a previously known value for selecting the ion of choice. A typical value for the inflection magnet current was roughly 2 A for H^- beam throughput. The remaining high voltage power supplies for the source voltage, cathode voltage, and einzel voltage were then set to previously found values for maximum beam current for the given ion of choice. The source voltage and cathode voltage typically sum to a value of roughly 6 kV. Once these voltages were set, the ionizer current was stepped up to 22 A by 2 A every five minutes. This high current resulted in an operational temperature of roughly 1200°C. The canal connecting the cesium reservoir and ion source was then heated by a 28 W coil heater. The cesium oven was then set to 5 W. The temperature of the cesium oven was monitored at these settings until a temperature of 24°C was reached. This temperature readout was taken by a thermocouple located on the oven, and has been previously determined to be primarily a result of the canal reaching a maximum operating temperature. The cesium canal was heated prior to the cesium oven to prevent buildup of flow-limiting cesium residue in the canal. After the canal was sufficiently heated, the cesium oven was set to 30 W. This oven heater setting resulted in an oven temperature of roughly 100°C in one hour. During this time, beam current on the low-energy Faraday cup was monitored by an RBD 9103 Autoranging Picoammeter with a resolution

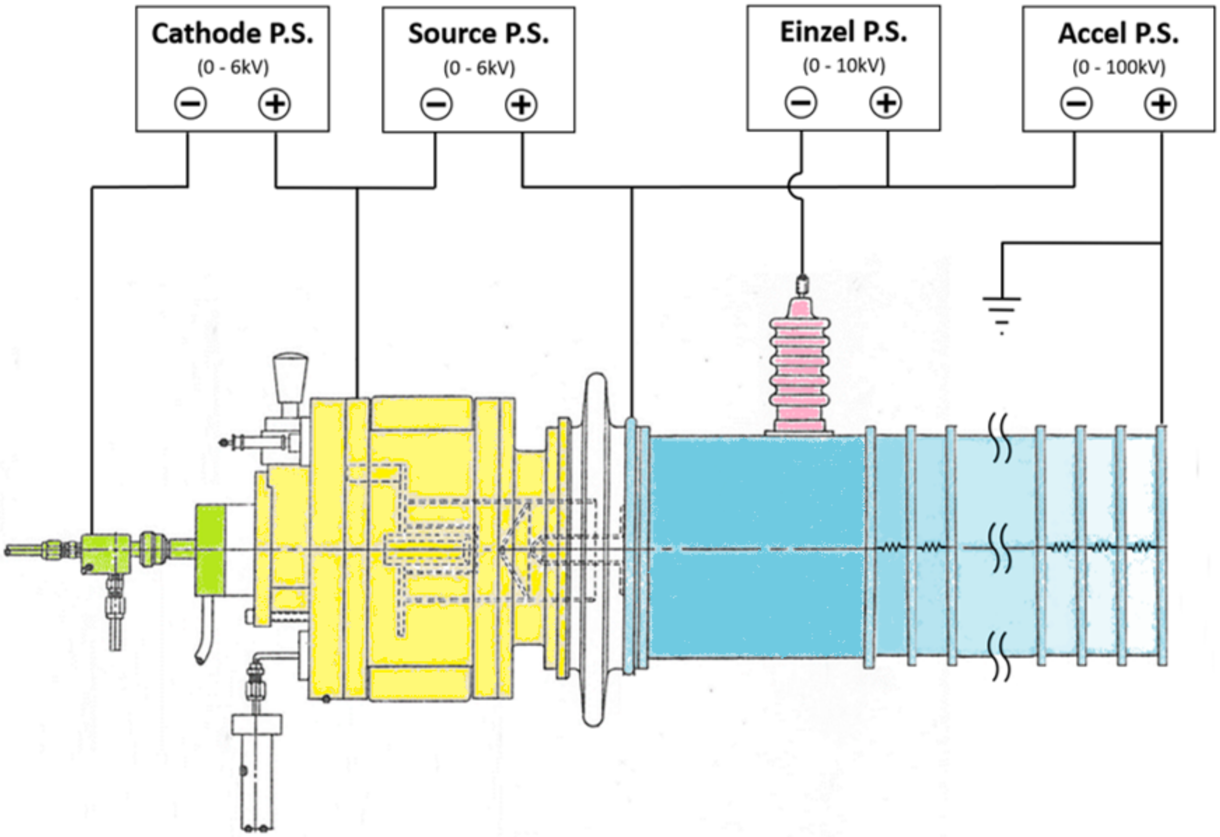

Figure 13: Electrictonics diagram for the cesium sputter ion source. Cesium plasma was accelerated to the left towards the negatively biased cathode assembly (green). Negative ion beam produced by cesium sputtering was repelled from the cathode bias (green) and accelerated through the source bias (yellow) and the accelerating column (blue) [76].

of 1 nA at 20 μA full scale. At an oven temperature of 100°C, parameters including inflection magnet current, vertical steering magnet current, source voltage, cathode voltage, and einzel voltage could be adjusted to maximize beam current on the low-energy Faraday cup. Typical low-energy beam currents of roughly 10 μA H^- were measured with this procedure. A freshly-packed cathode typically lasted roughly 20 hours under these conditions.

In the case of a loss in beam current during data collection due to insufficient cathode target output, the cathode could be changed without repeating the ion source start-up procedure. The high voltage power supplies associated with the ion source were set to 0V while the ionizer, canal, and oven currents remained constant. The interlock-equipped access panel was opened, and the shorting rod was attached to the source. This triple redundancy provided adequate electrical safety measures to handle the cathode assembly. The cathode assembly can then be retracted beyond the gate valve without a loss in vacuum. The gate valve was closed to isolate the cathode assembly from the source. After installing a new cathode, the cathode assembly was reinserted into the pre-valve chamber. This chamber was evacuated to rough vacuum before re-opening the gate valve and setting the cathode assembly in place.

The software used to control the ion source components was created by Accelerator Engineering staff at ECU with Nation Instruments' Laboratory Virtual Instrument Engineering Workbench (LabVIEW). The LabVIEW user interface is shown in Fig.14. This interface allowed the operator to adjust input settings, operate faraday cups, and monitor readouts. The source current and cathode current were closely monitored over time, as these readouts indicated an excess buildup of sputtering artifacts which compromised the operation of the high voltage power supplies. These artifacts of sputtering including carbon, aluminum, and copper would build up over time and bridge the gaps between components, current limiting the applied voltages. Various internal components of the ion source were disassembled and polished on a lathe as needed by the ECU machine shop staff to prevent this electrical shorting.

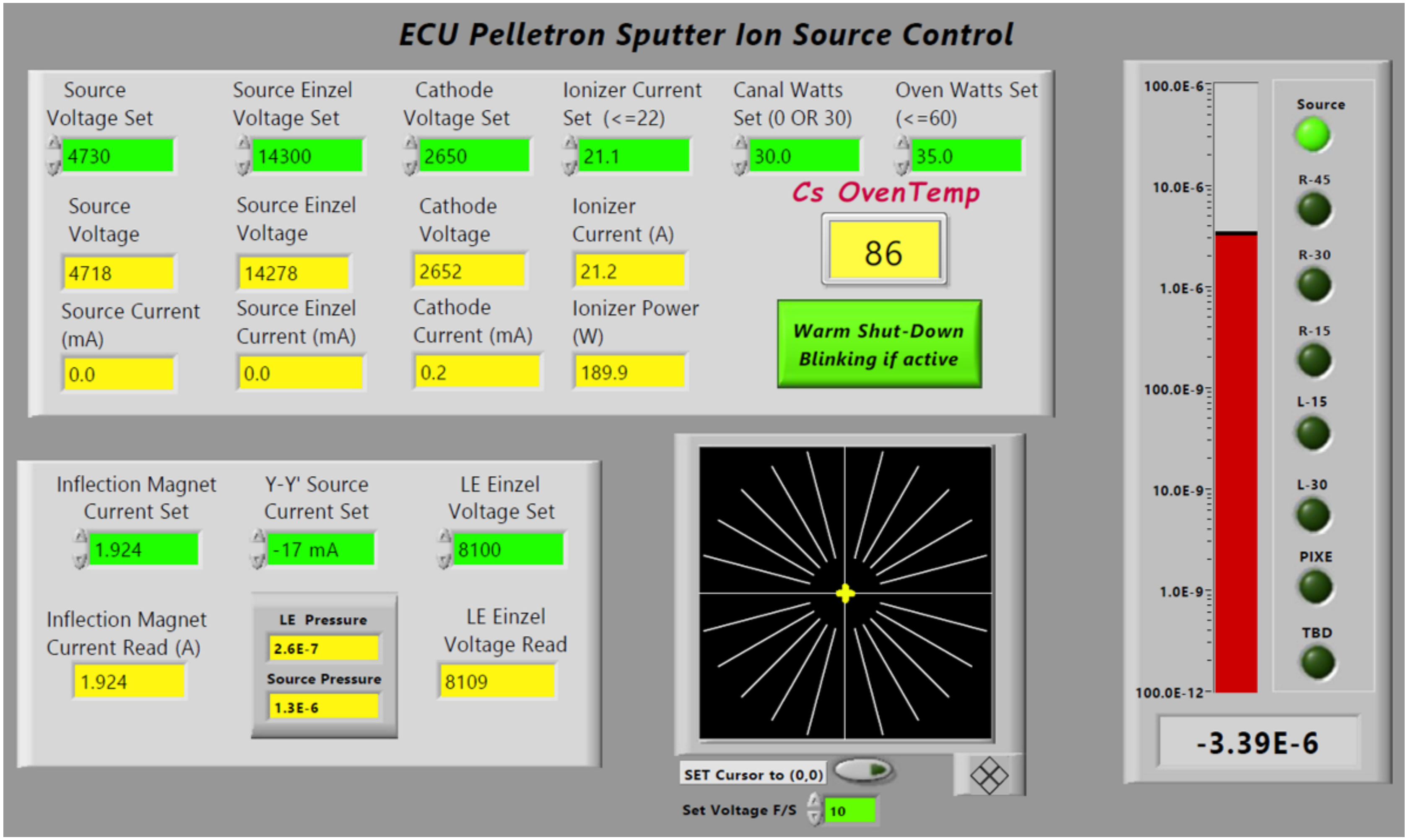

ECU Pelletron Sputter Ion Source Control

Source Voltage Set: 4730
Source Einzel Voltage Set: 14300
Cathode Voltage Set: 2650
Ionizer Current Set (<=22): 21.1
Canal Watts Set (0 OR 30): 30.0
Oven Watts Set (<=60): 35.0

Source Voltage: 4718
Source Einzel Voltage: 14278
Cathode Voltage: 2652
Ionizer Current (A): 21.2
Cs OvenTemp: 86

Source Current (mA): 0.0
Source Einzel Current (mA): 0.0
Cathode Current (mA): 0.2
Ionizer Power (W): 189.9

Warm Shut-Down Blinking if active

Inflection Magnet Current Set: 1.924
Y-Y' Source Current Set: -17 mA
LE Einzel Voltage Set: 8100

Inflection Magnet Current Read (A): 1.924
LE Pressure: 2.6E-7
Source Pressure: 1.3E-6
LE Einzel Voltage Read: 8109

SET Cursor to (0,0)
Set Voltage F/S: 10

-3.39E-6

Figure 14: Software interface for the Ion source and low-energy beamline component controls. Controls, or inputs, are shown in green while readouts, or outputs, are shown in yellow. Various lab Faraday cup controls are shown on the right and electrostatic steerer controls are displayed as a polar array in the bottom-middle.

2.2 Accelerator

The ECU Accelerator Laboratory is equipped with a National Electrostatics Corporation 2 MV Pelletron tandem accelerator. Insulated chain links transport charge from a charging station to the central terminal similar to a Van de Graff generator, biasing the central terminal up to +2 MV. A series of insulated rings with connecting resistor chain steps this 2 MV bias down evenly to create a uniform electrostatic field along the axial center [75, 77, 78]. Negatively charged ions injected into the accelerator were accelerated toward the positively charged central terminal based on the initial charge state. Singly charged hydrogen and carbon ions were injected into the accelerator for this work. The energy gained by ions moving through this uniform electric field,

$$E = qV, \tag{15}$$

depended on the charge q and electric potential of the central terminal, V. Upon reaching the central terminal, a N_2 gas jet acted as an electron stripper, generating a variety of positively charged ions. These now positively charged ions are accelerated away from the positively charged central terminal, resulting in a dual acceleration. The injection of singly charged H^- ions resulted in the ejection of H^+ ions with an increase in energy of 4 MeV at 2 MV central terminal bias. Optimal yield of negatively charged ions through the accelerator occurred in the range of 1-2 MV central terminal voltage with a partial pressure of 1 μTorr N_2 stripper gas. For more complex ions, multiple charge states are generated at the central terminal during electron stripping. An injection of negative carbon ions, C^-, resulted in a wide variety of molecular and charge states and will be discussed in the following chapter. An analyzing magnet was used to select the charge-to-mass ratio of these positive ions injected into an experimental beamline at a specific angle from normal incident beam (Fig.15). Faraday cups were used to measure beam current in the low-energy beamline, the high-energy beamline, and experimental beamline for beam optics optimization.

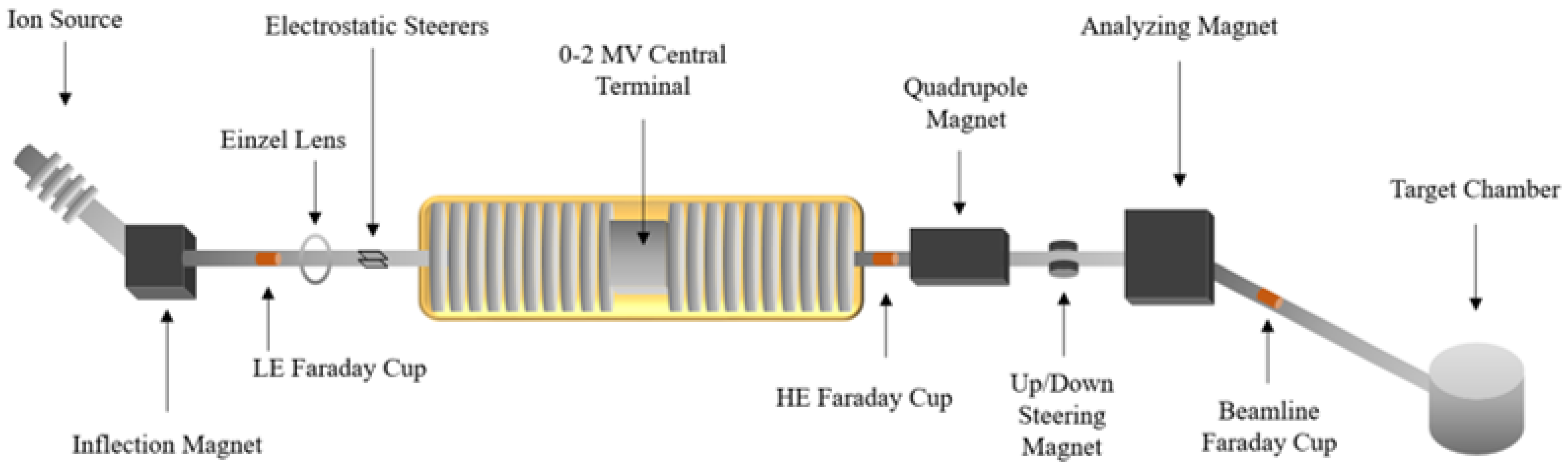

Figure 15: Diagrammatic display of the ECU Accelerator facility. The ion source (left) produces negative ions that are injected into the Pelletron tandem accelerator, stripped of electrons at the central terminal, and ejected as positively charged ions. The analyzing magnet steers the positively charged ions into the R15 beamline (right) for data acquisition.

Beam current was maximized on the low-energy beamline Faraday cup using the methods described in the previous chapter. This negative ion beam produced by the ion source was considered “dirty” beam due to the various artifacts sputtered off of the ion source cathode. The inflection magnet between the ion source and low-energy beamline served as an ion selector by allowing passage of only the specific charge-to-mass ratio desired, discarding artifacts of copper, aluminum, titanium, etc.

After low-energy beam current maximization via ion source optimization, as discussed in the previous chapter, a set of electrostatic steerers and an einzel lens were used to maximize current on the high-energy beamline. The electrostatic steerers directed the beam vertically and horizontally using a uniform electric field between parallel charged plates. The low-energy einzel lens served as a beam focus by setting the focal length of the beam to match the position of the high-energy Faraday cup via a set of concentric charged rings, normal to the beam path. During the electron exchange process with N_2 stripper gas in the central terminal, a variety of molecular and charge states of ions were produced. These positive ions, in the case of hydrogen and carbon beam, also varied in energy due to the varying charge states.

In order to maximize current on the beamline Faraday cup, a second steering magnet, labeled as the analyzing magnet in Fig.15, served as both a horizontal steering component as well as a beam charge state selector. Steering the beam 15 degrees from normal, into the electron emission beamline, allowed the specific mono-energetic charge-to-mass ratio beam required for data analysis. An accompanying up/down steering magnet on the high-energy beamline served as a vertical steering component for maximizing beam current on the beamline Faraday cup. A quadrupole magnet was used for focusing the beam on the beamline Faraday cup, similarly to an einzel lens, with the added effect of beam shaping in the transverse plane. Quartz crystals, positioned at the low energy Faraday cup and the beamline Faraday cup, illuminate blue light during ion beam interaction and were used to image the beam during alignment, focusing, and shaping.

2.3 Ion Beam Production

For this experiment, both proton and carbon beam were used as incident beam to measure ion-induced electron yields. In order to generate H$^-$ at the ion source, aluminum cathodes packed with titanium hydride powder were sputtered with cesium plasma as described in a previous chapter. This same procedure was used to generate C$^-$ ions using an aluminum cathode packed with graphite powder. A typical beam current measured for H$^-$ ions on the low-energy Faraday cup was 10 μA, and typical H$^+$ yields on the high-energy Faraday cup were roughly 50%. This is due to the cross section interaction probability of ionization between 1-2 MeV H$^-$ and N_2 at 1 μTorr partial pressure. Another loss of 50% occurs between the high-energy and beamline currents as the analyzing magnet selects only the mono-energetic H$^-$ ions from the accelerator output. The stripper gas is designed to be localized about the central terminal, but some N_2 straggling can occur and lead to late ionization, resulting in undesired energies. Other molecular artifacts can be generated in the central terminal during electron transfer that were eliminated using the analyzing magnet.

Identifying carbon ion species produced by the accelerator was done by measuring the radius of curvature of the analyzing magnet with protons, modeling the various run parameters for various carbon ion species, then experimentally verifying current peaks predicted by the model. Any massive object following a curved path must experience a centripetal force,

$$F_C = \frac{mv^2}{r}, \tag{16}$$

where m is mass, v is velocity, and r is radius of curvature. In the case of an ion moving perpendicular through a uniform magnetic field, this force is the Lorentz force

$$F_L = qvB, \tag{17}$$

where q is electric charge, v is velocity, and B is the magnetic field strength. Equating centripetal and Lorentz force,

$$\frac{mv^2}{r} = qvB, \tag{18}$$

an expression for desired magnetic field strength to pass a specific charge-to-mass ratio at a certain velocity can be obtained:

$$B = \frac{mv}{qr}. \tag{19}$$

In order to predict and identify the species of carbon ion beam passing through the analyzing magnet, a radius of curvature for the magnet had to be measured. This was done by measuring various energy proton beam peaks passing through the analyzing magnet and assuming a linear relationship between the magnet current and magnetic field. This radius of curvature with arbitrary units,

$$R^* = \frac{m_p v}{q_p I} \tag{20}$$

was calculated using the analyzing magnet current, I, proton mass, m_p, and proton charge, q_p as shown in Table 1. Only the analyzing magnet current settings used to identify main peaks in mono-energetic proton beam with confirmed 50% or greater throughput yield were measured.

Table 1: The radius of curvature calculations (with arbitrary units) for proton beam passage of various energies. Analyzing magnet current, charge, mass, and velocity were used to calculate the above radii.

Pass Energy (MeV)	Magnet Current (A)	Charge (e)	Mass (amu)	Velocity (m/s)	Radius *
1	6.8	1	1	1.39E+07	2.04E+06
2	9.6	1	1	1.96E+07	2.05E+06
4	13.3	1	1	2.78E+07	2.09E+06

An average R^* of 2.06×10^6 was used to predict the analyzing magnet current necessary to identify various carbon ion charge states. Re-arranging the above equation for carbon ion beam passing through the analyzing magnet,

$$I = \frac{m_c v}{q_c R^*}, \tag{21}$$

predictions were made for analyzing magnet current settings necessary to identify various charge and molecular states of carbon beam. In the above equation, m_c is the mass of carbon in atomic mass units and q_c is the charge state of various carbon ions in elementary charge units. Various charge states of carbon beam were used in this investigation, while all molecular carbon beam was excluded. A sample calculation for various carbon ion beam charge states accelerated through a 1 MV central terminal and passing through the analyzing magnet is shown in Table 2.

Table 2: Analyzing magnet current settings calculations and measurements for carbon ion beam accelerated through a 1 MV central terminal tandem accelerator. The discrepancies of less than 1% allow confidence in identification of carbon ion charge states.

Molecule	C(5+)	C(4+)	C(3+)	C(2+)	C(+)
Charge in	1	1	1	1	1
Charge out	5	4	3	2	1
Mass	12	12	12	12	12
Energy (MeV)	5.93	4.95	3.96	2.98	2.00
Energy (J)	9.50E-13	7.92E-13	6.35E-13	4.78E-13	3.20E-13
Velocity (m/s)	9.76E+06	8.92E+06	7.98E+06	6.92E+06	5.67E+06
Velocity (c)	0.033	0.030	0.027	0.023	0.019
Calculated Magnet (A)	**11.22**	**12.81**	**15.29**	**19.89**	**32.57**
Measured Magnet (A)	-	12.82	15.35	20.07	32.92

The highest yield carbon ion charge states found during this investigation were C^{2+} and C^{3+}. C^{1+} and C^{4+} beams were low yield alternatives that required extremely long run times for comparable resolution in spectra. No yield of C^{5+} or C^{6+} were detected using this process.

2.4 Beam Pulser

In order to measure electron yields, a high-precision timed pulsed beam was necessary. A beam pulser was designed to sweep the beam across a 1 mm collimator prior to the entrance of the UHV chamber. A pair of synchronized parallel plates created a set of uniform electric fields used to divert the ion beam at regular intervals. A diagram of the beam pulser is shown in Fig.16. The first of the two parallel plates set were designed to create a vertical electric field by charging two electrically isolated stainless steel plates 2.54 cm in width and 12.7 cm in length. The bottom plate was held at a static 1200 V DC to hold the beam over the entrance collimator before the fast downward sweep. The upper plate charged up from 0 V to 2000 V in a few nanoseconds to push the beam downwards to a new static position below the entrance collimator. The second, downstream, set of parallel plates were positioned vertically in order to translate the ion beam horizontally by creating a horizontal uniform electric field. The right plate was grounded while the left plate was charged up from 0 V to 400 V, translating the beam to the right. After the beam reached this static position, both primary and secondary parallel plates were discharged back to 0 V, returning the beam to the original position above the entrance collimator over several hundred nanoseconds. This cycle was repeated at 10 kHz with the initial downward flash occurring during the first 5% of the duty cycle. The printed circuit board designed for the synchronized charging of parallel plates utilized metal-oxide-semiconductor field-effect transistors (MOSFETs). A diagram of the beam pulser circuit, designed by ECU staff member William Holland, is shown in Fig.17.

The power supply settings and operational frequency of the beam pulser were specifically selected in order to operate within the heat limits of the circuitry, as well as sufficiently divert both H^+ and C^{2+} beam. All projectiles in this study were traveling less than $0.1c$, allowing for non-relativistic calculations of their motion. The kinetic energy, K, of ion projectiles that passed through the beam pulser was

$$K = \frac{1}{2} m {v_z}^2, \tag{22}$$

where m is the projectile mass and v_z is the projectile velocity. Re-arranging for v_z, we get

$$v_z = \sqrt{\frac{2K}{m}}. \tag{23}$$

The time for a projectile to pass through the initial parallel plate assembly, t_p was

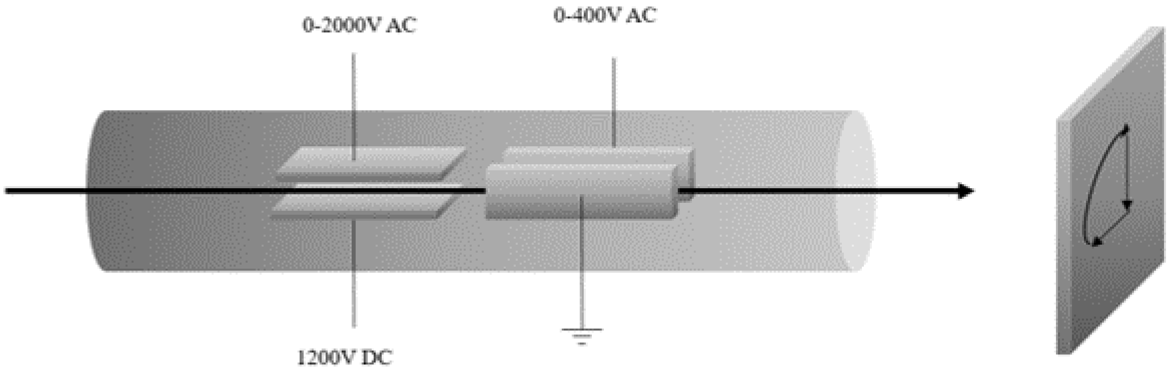

Figure 16: Diagram of the beam pulser designed to flash fast pulses of ion beam through the UHV chamber entrance collimator at 10 kHz. The "D-shaped" pattern of the beam path is shown on the right side of the figure, with the beam initially positioned at the top of the diagram prior to being swept across the UHV entrance collimator.

$$t_p = \frac{L_p}{v_z}, \tag{24}$$

where L_p is the length of the parallel plate assembly, or 12.7 cm. Equating the magnitude of coulomb force, F, to Newton's second law of motion,

$$F = qE = ma, \tag{25}$$

an expression can be found for acceleration,

$$a = \frac{qE}{m}, \tag{26}$$

in terms of q, the projectile's electric charge, and E, the uniform electric field between the parallel plates. Since the electric field E is uniform in the local region of the projectile's path, we can substitute

$$E = \frac{V}{d}, \tag{27}$$

where V is the voltage between plates and d is the distance between plates (1.27 cm), into our acceleration equation to get

$$a = \frac{qV}{md}. \tag{28}$$

Given an initial vertical velocity, v_{y0} of zero, the vertical velocity, v_y of a projectile exiting the parallel plate assembly must be

$$v_y = at_p. \tag{29}$$

The time for a projectile to travel from the exit of the first parallel plate assembly to the entrance collimator of the UHV chamber,

$$t_{UHV} = \frac{L_{UHV}}{v_z} \tag{30}$$

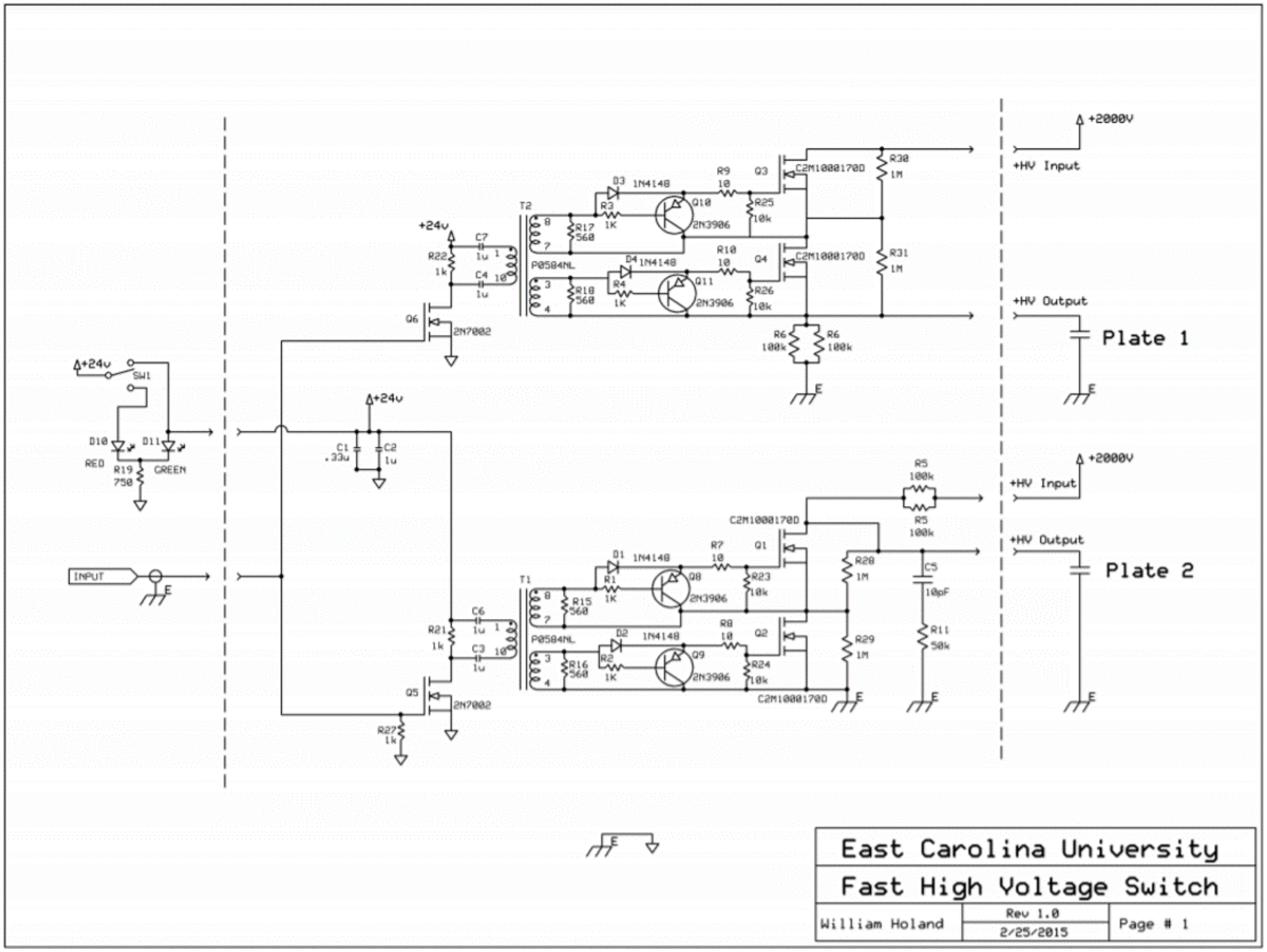

Figure 17: Electronics diagram of the metal-oxide-semiconductor field-effect transistor (MOSFET) circuit designed by ECU staff to control the beam pulser HV supplies attached to the parallel plate assemblies.
]

was found by measuring the distance from the parallel plate assembly to the UHV chamber, L_{UHV}. With the above equations, an expression was found to predict the vertical displacement of the beam,

$$y = v_y t_{UHV}. \tag{31}$$

By substitution of v_y and t_{UHV}, we have

$$y = (a t_p)\left(\frac{L_{UHV}}{v_z}\right). \tag{32}$$

By further substitution of a and t_p, we have

$$y = \left(\frac{qVL_p}{mdv_z}\right)\left(\frac{L_{UHV}}{v_z}\right). \tag{33}$$

which simplifies to

$$y = \frac{qVL_pL_{UHV}}{2dK} \tag{34}$$

with the initial expression for v_z. With the above expression, a vertical displacement of 27 mm - 6.8 mm was predicted for H^+ of energy 1 - 4 MeV with an applied AC voltage of 0 - 2000V on the primary plate. A vertical displacement of 23 mm - 9.1 mm was predicted for C^{2+} ions of energy 2.4 - 6 MeV. Both ranges of vertical displacement were found to be sufficient for a fast sweep across the 1 mm diameter UHV entrance collimator while operating within the heat restrictions of the MOSFET circuitry.

2.5 UHV Chamber

The vacuum chamber used for this experiment was an ultra-high vacuum (UHV) compatible (nTorr range) system shown in Fig.18 and Fig.19. Every apparatus installed onto the UHV chamber employed ConFlat flange technology, creating a vacuum seal by compressing copper gaskets with knife edges, allowing for ultra-high vacuum conditions. These metal gaskets provided a better alternative to standard Viton o-ring seals due to the ability to operate under high temperatures. A turbomolecular pump was used to achieve a base pressure of roughly 100 nTorr. The titanium sublimation pump was flashed daily to remove a large portion of the remaining hydrogen in the UHV chamber, lowering the total pressure by over an order of magnitude. Ion beam entered the chamber through a 1 mm diameter entrance collimator, through a centrally located target assembly, and into a Faraday cup positioned at the back of the chamber. Beam current could be measured in the Faraday cup positioned in the back of the chamber for alignment, optical optimization, and system tests. Although, during data collection the beam was pulsed, reducing current by up to a factor of 1000, which was not practically measurable.

A bake-out procedure, in conjunction with the high vacuum pumps, was performed to reduce the chamber pressure to roughly 1 nTorr. The bake-out procedure involves heating the chamber to a temperature of 100°C for 24 hours, and was necessary each time the chamber is opened for repair or target changes. Maintaining ultra-high vacuum was necessary to keep the target clean under low temperature conditions due to particulate build up from freezing. Additional ion sputter cleaning guns were installed onto the UHV chamber in order to ablate the front and back surfaces of the target assembly to ensure a clean surface. These ion sputter guns used high intensity neon gas jets, accelerated through a hot filament, to sputter clean the target. Neon projectiles were necessary in order to prevent freezing of the sputter ions onto the target under low temperature conditions. A gas leak valve was used to fill the UHV chamber with ultra-high purity deionized water at a rate that would raise the chamber pressure from 1 nTorr to 100 nTorr during target preparation. The procedure for various target preparations including amorphous solid water will be discussed in a later section.

The centrally-located UHV target assembly is shown in Fig.20. The target assembly is positioned on top of a flash heater, used to clean the target surface during bake-out. This flash heater apparatus is equipped with a thermocouple used to monitor the target temperature during both high and low temperature conditions. A sapphire isolation tube

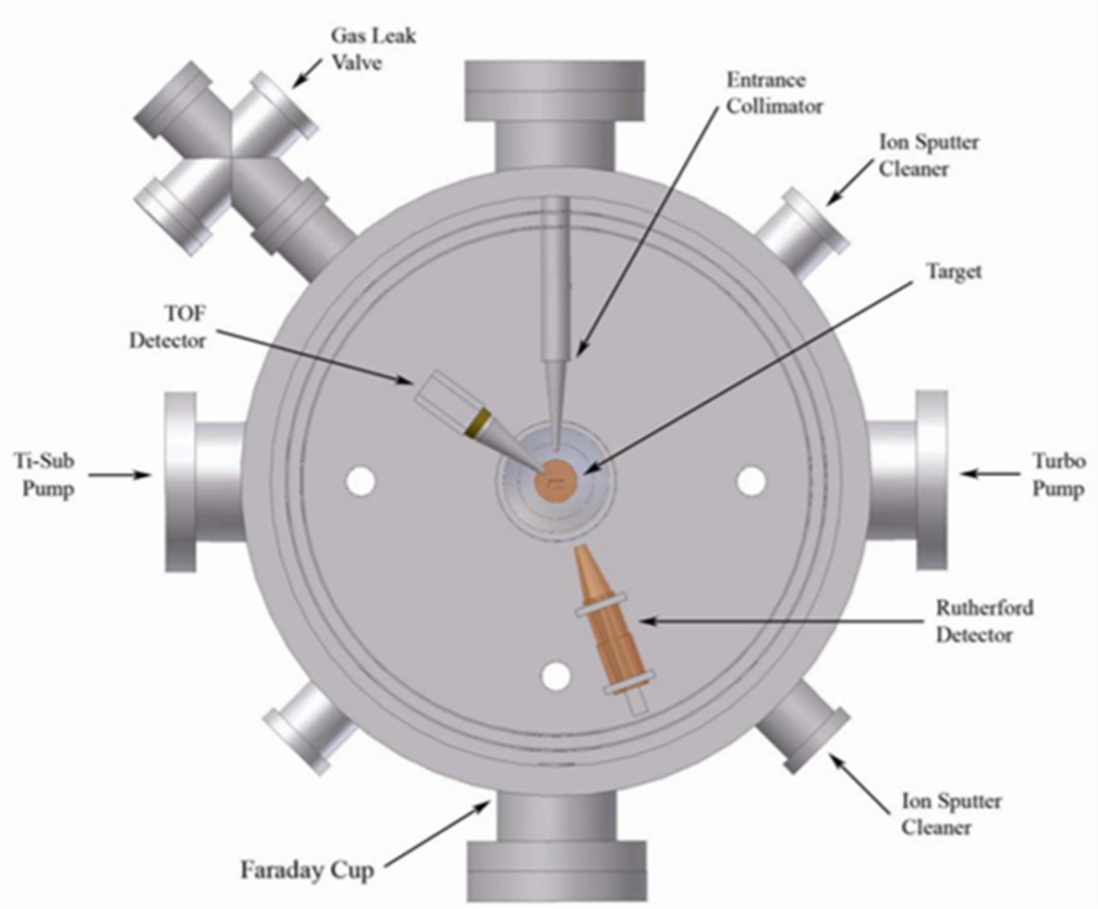

Figure 18: Overhead view of the ultra-high vacuum chamber. Shown above are the stationary Rutherford scattering detector used to measure scattered protons and the rotatable time-of-flight detector used to measure scattered electrons. Beam enters the chamber from the top of the figure, travels through the target assembly, and is collected in the Faraday cup at the bottom of the figure [3].

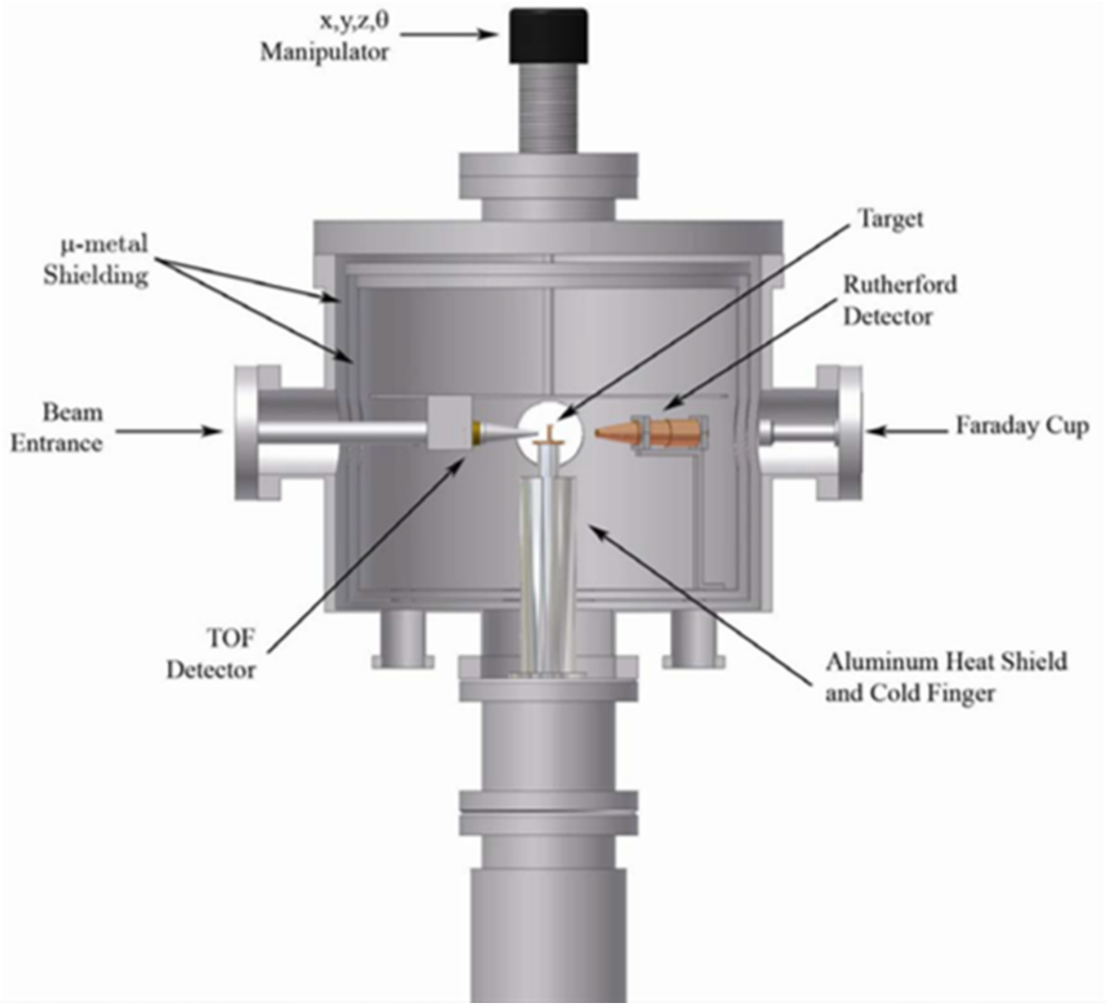

Figure 19: Side view of the ultra-high vacuum chamber. Shown above is the profile of the target holder assembly equipped with helium cold finger [3].

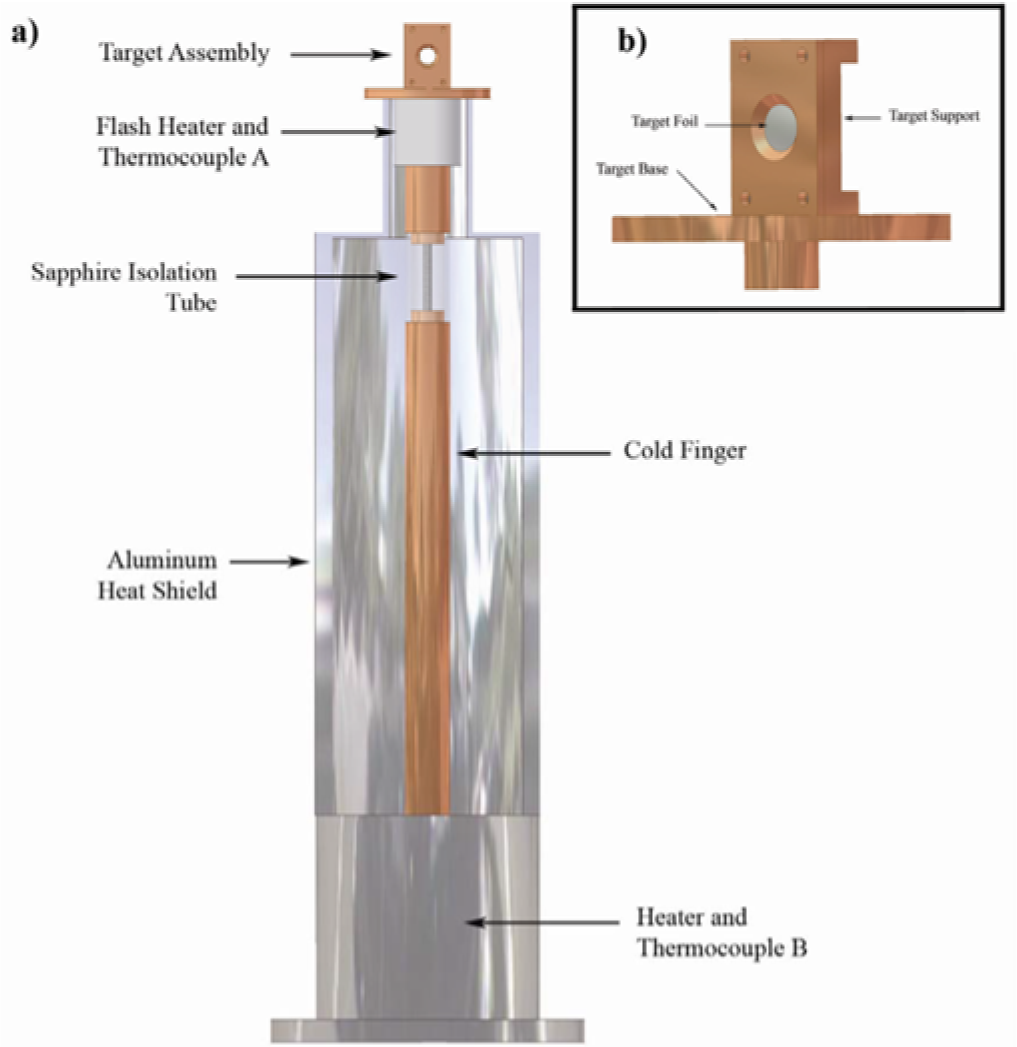

Figure 20: Cut out view (a) of the aluminum heat shield used to house the compressed-helium cold finger supporting the target assembly. A flash heater was used for target cleaning during the chamber bake out procedure. A side view (b) of the target assembly shows the beveled entrance window of the support that offers a greater range of angles in which secondary electron emission can be measured [3].

was used to electrically isolate the target assembly from the chamber while allowing good thermal conductivity. A compressed helium driven cold finger was connected to the target assembly in order to flash freeze water vapor onto the surface of target foils at roughly 20 K. An additional heater and thermocouple was installed onto the bottom of the surrounding heat shield, allowing for bake-out of the target assembly holder and thermal isolation of the cold finger from the rest of the chamber during low temperature conditions. The target foils used in this investigation were held between two copper plates, as shown in Fig.20(b). This target holder was designed with beveled edges at the entrance and exit apertures to allow for a wider range of angles for electron emission measurements. Typical targets positioned in this target assembly holder were 1 μm thick metallic foils. Ion beam entered the chamber through the 1mm diameter entrance collimator, traveled through this thin film target, and was collected in the rear Faraday cup. Typical ion beam currents collected through the thin films were on the order of tens of nanoamps, before being pulsed, with tens of microamps being generated upstream by the ion source.

The UHV chamber is equipped with a stationary Rutherford detector used to count scattered projectiles after passing through the target assembly. The Rutherford detector contained a Channel Electron Multiplier (CEM, often reffered to as a channeltron) assembly that was wired to accept only positively charged particles and was mounted at 20° from the incident beam. An electronics diagram of the CEM wiring and a cut-out view of the Rutherford detector assembly is shown in Fig.21. The CEM in the Rutherford detector was designed by Dr. Sjuts Optotechnik and utilizes a continuous dynode cascade for signal amplification. A gain of 1×10^8 electrons can be obtained from one incident photon, electron, or ion entering the conical entrance aperture. The output signal from this cascade is a sharp negative pulse of full-width half-maximum 8 ns. This design of detector was ideal for scattered ion detection due to the robust nature of the silicon channel walls, as well as the ability to count tens of thousands per second without saturating the output signals.

A free-pivoting time-of-flight (TOF) detector was mounted to the lid of the UHV

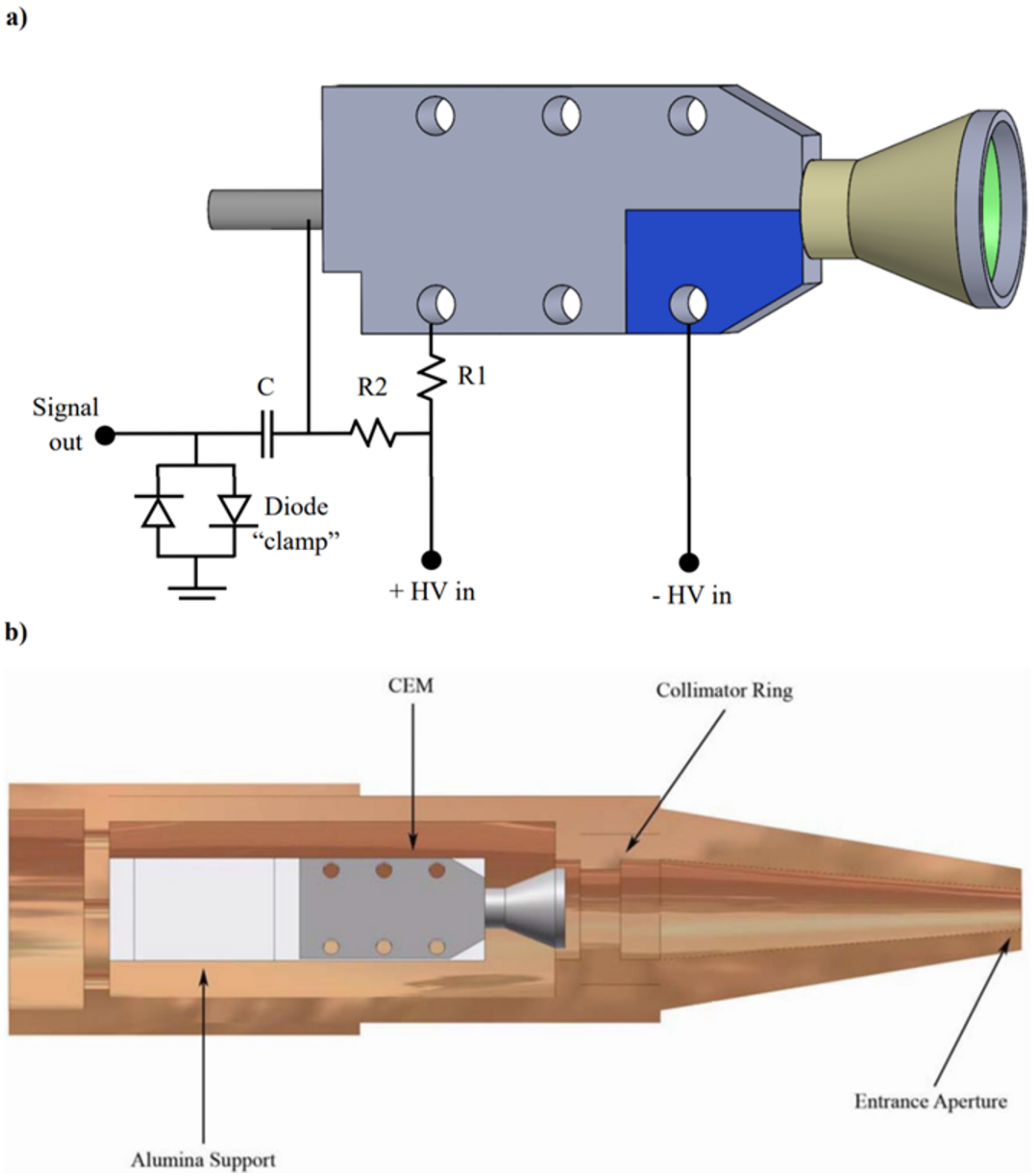

Figure 21: Electronics diagram (a) of the Rutherford detector used to count scattered projectiles during electron yield measurements. A cross-sectional diagram of the Rutherford detector assembly is shown below (b).

chamber capable of measuring low energy (0.1 - 100 eV) electron emission from the fast ion interactions with the target assembly. The external controls for the TOF detector allowed for alignment in three dimensions, as well as rotation about half of the UHV chamber (from 0° to 160° from incident beam). A diagram of the construction and wiring of the TOF detector is shown in Fig.22. The TOF detector utilized a multichannel plate (MCP) assembly as described by Ladislas Wiza [79]. An MCP assembly works similarly to a photomultiplier tube or electron multiplier with the added advantage of higher yield due to the enhanced spatial resolution of the channel array design. MCP channels are designed to be tilted away from the normal angle of incidence by roughly 15° in order to ensure surface contact from incoming projectiles. These straight, angled channels were made of semiconducting glass and held under high voltage to produce an electron cascade. The combination of two parallel multichannel plates with alternating channel angles and separation distance of roughly 100 microns is referred to as a chevron assembly. An illustration of the electron cascade in an MCP assembly, as well as a diagram of a chevron assembly of MCPs is shown in Fig.23. The advantage of the chevron assembly is the ability to achieve higher gains (2-3 orders of magnitude) in output signal with lower high voltage power supplies. This provided signal analysis of low amplitude, fast signals with inexpensive nuclear instrumentation module (NIM) electronics, as well as maximizing gains with the use of UHV compatible wiring in conjunction with high voltage power supplies.

2.6 Electron Yields

A data acquisition system was designed to perform time-of-flight (TOF) energy analysis (electronics diagram shown in Fig.24) of the secondary electron emissions from solid state targets. A LabView program was designed to trigger 10 kHz beam pulser signals from a National Instruments USB board. The same 10 kHz signal was routed to a delay which was used as the start signal for a time-to-amplitude converter (TAC). This delay was necessary to account for the signal travel time and fast beam pulse delay before passing the beam

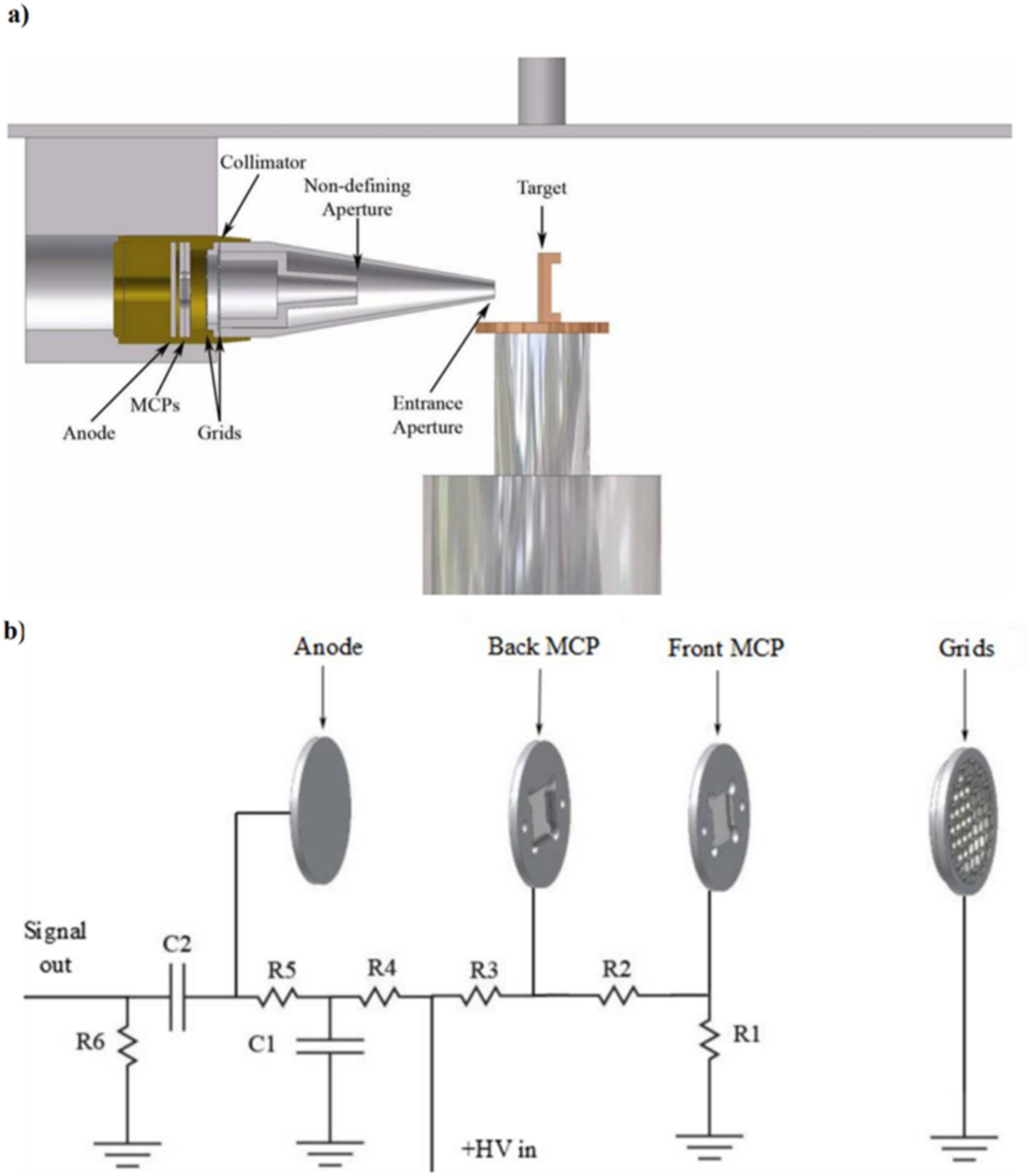

Figure 22: Cut-out view of the Time-of-Flight detector (a) showing scaled distance to the target assembly. The bottom image (b) is an electronics diagram of the multi-channel plate assembly inside of the Time-of-Flight detector.

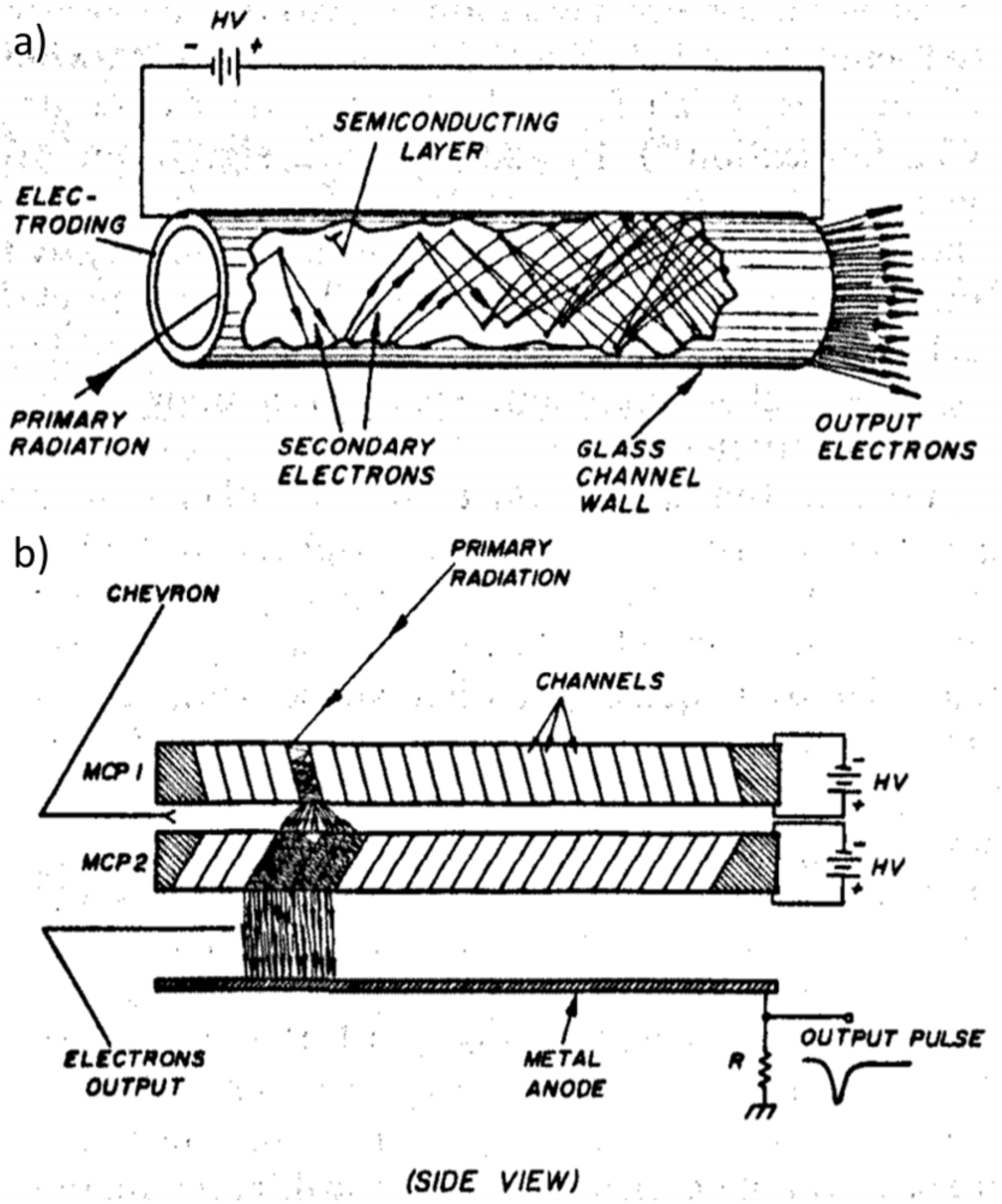

Figure 23: Electron cascade illustration (a) for a single channel in a multichannel plate (MCP) detector. A Chevron assembly of two MCPs with separation distance of roughly 100 microns [79].

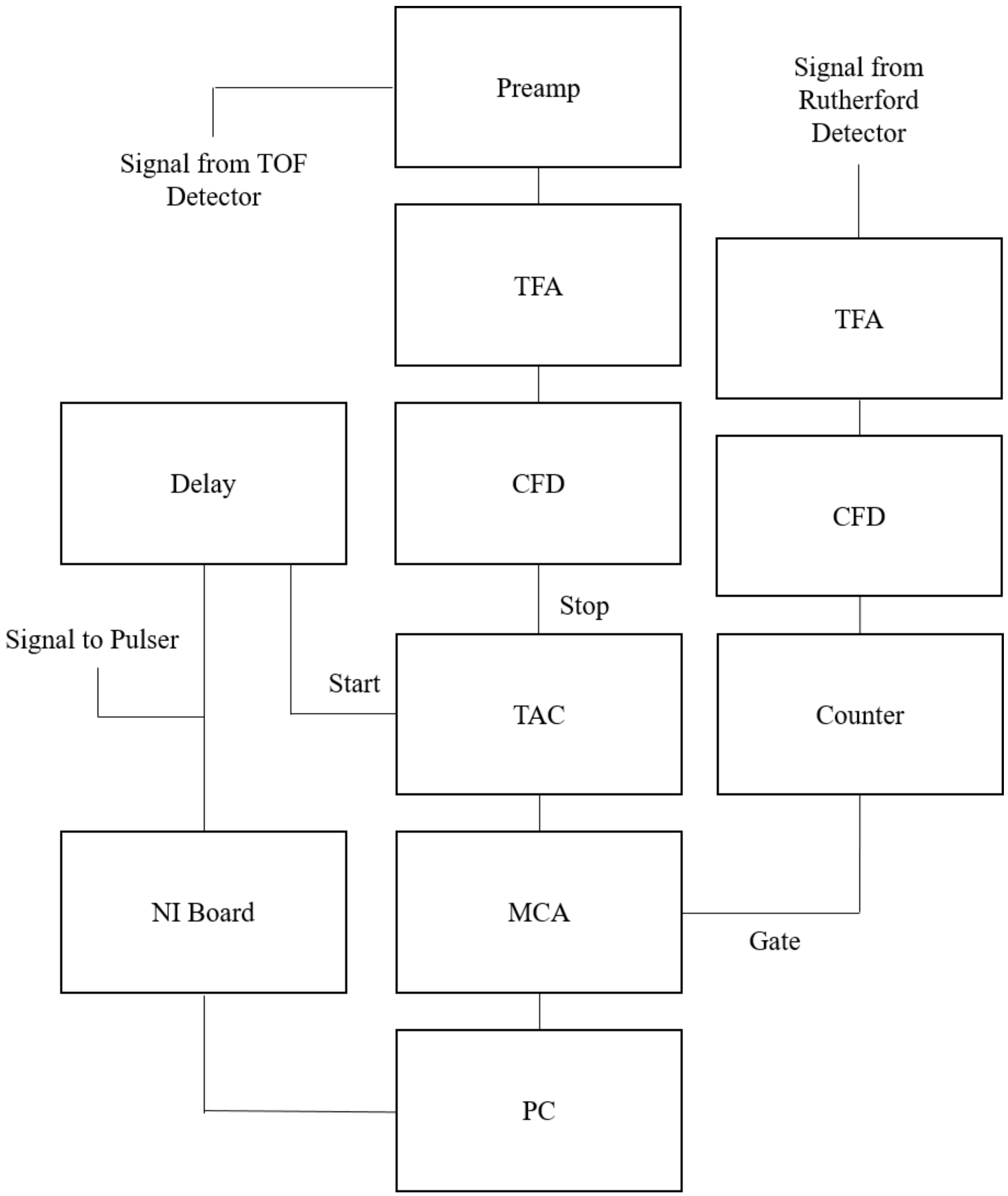

Figure 24: Diagrammatic display of the Time of flight data acquisition system used to measure secondary electron energies. A time of flight electron detector and Rutherford scattered ion detector work in conjunction with signals from a 10 kHz beam pulser to generate time stamped electron events to sort and bin signals in a multi-channel analyzer by way of a time to amplitude converter.

through a 1 mm collimator at the entrance of the UHV chamber. The TOF electron detector signals, collected by the multi-channel plates, were first amplified through a pre-amplifier, then again through a timing filter amplifier (TFA). A constant fraction discriminator was used to filter the noise from this signal and was sent to the TAC to be used as a stop signal. The TAC converted the time difference between start and stop signals to a square wave of amplitude 0 - 10 V scaling with time in a range of 500 ns. A multi-channel analyzer (MCA) was used to bin the TAC output signals into 2048 channels corresponding to evenly distributed signal amplitudes from 0 - 10 V. Binned counts form the MCA were used to build TOF spectra in Canberra Genie software and will be referred to as "raw count" spectra for the remainder of this paper. The Genie software was designed to receive MCA signals for a predetermined amount of time based on user preference. During Genie's data collection time window, a signal counter was used to integrate the scattered ion events measured by the stationary Rutherford detector. Signals from the Rutherford detector were amplified through a TFA and filtered through a CFD before being counted on a quad timer counter. A gate on the MCA triggered the start and stop collection of the Rutherford's counter on the beginning and end of the timing window of the Genie software.

In order to calculate the conversion of channel number in Genie to corresponding time of flight, a signal pulser of known frequency was built for calibration. A 50 MHz pulser was built and installed in place of the TOF electron detector in the data acquisition system. The resulting 20 ns periodic peaks are shown in Fig.25 over a 500 ns timing window, binned into 2048 channels. A peak separation of 80 channels resulted in a calculated ratio, Δ_t, of 4.032 channels/ns.

By obtaining 0° peak spectra of incident ion beam, a single channel, Ch_p was identified as the peak channel in the distribution. These 0° peak spectra, for both protons and carbon ions had characteristic timing resolutions based on the full-width half-maximum, and are shown in Fig.26. From the projectile peak channel, Ch_p, a "zero" channel,

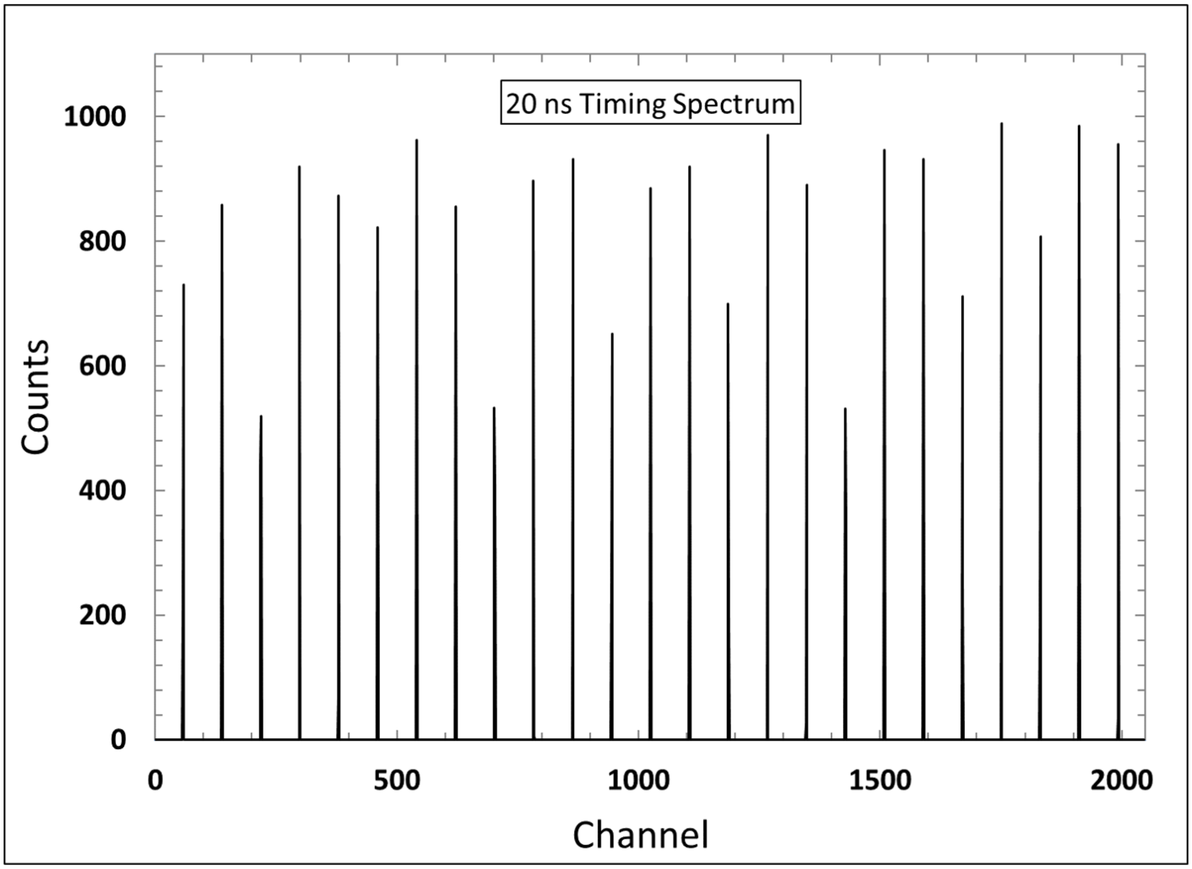

Figure 25: Timing calibration spectrum used to define the number of nanoseconds per channel. The above spectra was taken using a 50 MHz pulser over a 500 ns timing window.

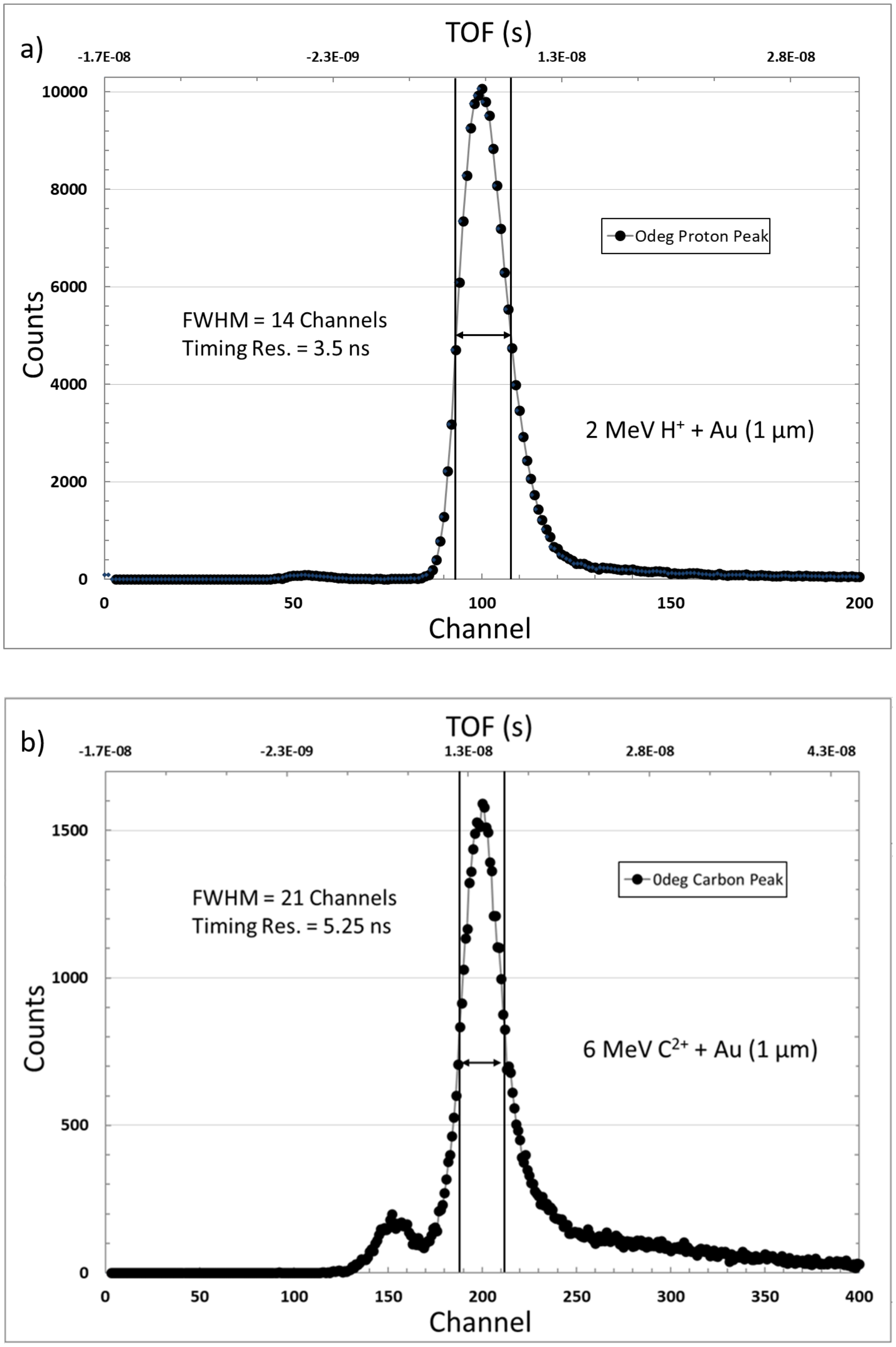

Figure 26: Typical proton (a) and carbon (b) spectra recorded at 0° incidence. From this spectra, electron travel time and detector timing resolution was resolved.

$$Ch_0 = Ch_p - t_p \Delta_t \tag{35}$$

could be defined that corresponded to the time in which the ion beam was incident on the target, where t_p is the time traveled from the exit of the target foil to the MCP assembly. In order to calculate this projectile time of travel,

$$t_p = \frac{d_p}{v_{exit}}, \tag{36}$$

the exit energy of the projectile, v_{exit}, leaving the back side of the target, as well as the distance from the target to the MCP assembly d_p had to be known. The distance from the foil to the MCP assembly was measured to be 94 mm, and the exit velocity v_{exit} of ions used in this study were calculated from the kinetic energy expression

$$K_{exit} = \frac{1}{2} m_p {v_{exit}}^2, \tag{37}$$

where m_p is projectile mass and K_{exit} is the kinetic energy of the projectile after passing through the target. The kinetic energy of each projectile after passing through the target foil was calculated using the stopping power and range of ions in matter (SRIM) code provided by Ziegler [71]. Zero degree peaks were found at the beginning of every data set for each projectile type and energy to ensure consistent timing calibration between spectra. With the channel Ch_0 identified, time-of-flight for electrons could be calculated for all TOF detector positions. The time-of-flight for an electron in nanoseconds,

$$t_e = \left| \frac{Ch_e - Ch_0}{\Delta_t} \right|, \tag{38}$$

was found by taking the difference of the electron event channel Ch_e found in an electron spectrum and the "zero" channel Ch_0 found from the incident projectile spectrum, then dividing by the time factor Δ_t. The resulting non-relativistic energy of electrons emitted from the target surface were

$$\varepsilon = \frac{1}{2} m_e {v_e}^2 = \frac{1}{2} m_e \left(\frac{d}{t_e} \right)^2 , \tag{39}$$

where d is the previously mentioned 94 mm from the target to the MCP assembly in the TOF detector. From the above expression, error propagation from timing resolution to energy resolution can be made. The uncertainty propagation formula

$$\frac{\delta \varepsilon}{|\varepsilon|} = |n| \frac{\delta t}{|t|} \tag{40}$$

applies here with the power $n = -2$. An illustration of the uncertainty in energy from 2 MeV proton impact on a 1 μm gold foil, as shown in Fig.26 (a) is shown in Table 3. This illustrates why the TOF method works very well to predict low energy (0.1 - 100 eV) electrons, but is not very useful for comparison to simulated high energy (> 100 eV) electrons. An example of a preliminary binned spectrum, referred to as "raw counts", is shown in Fig.27. These "raw" electron counts were used to find an energy distribution of electron yields from fast ion interactions. Initially a TOF distribution $\gamma(t, \theta)$, expressing the ratio of electrons produced per incident projectile, was necessary. The following expression

Table 3: Typical error propagation for electron energy with a timing resolution of 3.5 ns.

ε (eV)	t (ns)	δt (ns)	δt/t	$\delta\varepsilon/\varepsilon$
1	158.5	3.5	3.2%	6.3%
10	50.1	3.5	10.0%	19.9%
50	22.4	3.5	22.3%	44.6%
100	15.9	3.5	31.5%	63.1%
500	7.1	3.5	70.5%	141.1%

$$\gamma(t, \theta) = \frac{N_e}{N_p \xi T \Omega \Delta_t} \tag{41}$$

can be formed by finding the ratio of the number of electrons in each bin, N_e, to the number

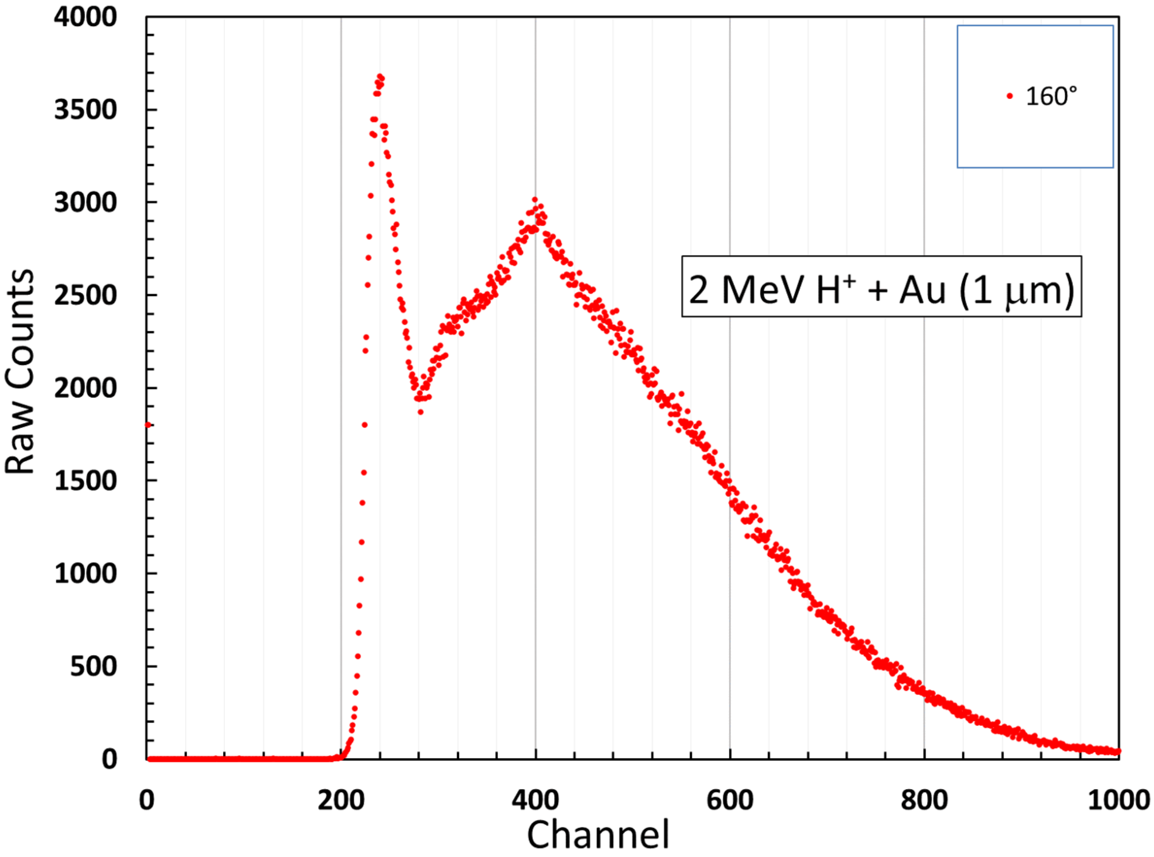

Figure 27: Example time-of-flight spectra of electron emission from 2 MeV proton interactions with 1 *mu*m Au foil at 160°. Each channel here corresponds to roughly 0.25 nanoseconds. Lower energy electrons, moving slower, appear farther to the right.

of projectiles, N_p, incident on the target. Here TOF detector efficiency ξ, solid angle subtended by the TOF detector collimator entrance Ω, and transmission coefficient of the TOF detector grids T, must be known. Time conversion of the 2048 channels in the raw count spectra is done by the above factor $\Delta_t = 4.032$ channels/ns. The energy distribution of electron yields $\gamma(\varepsilon, \theta)$, also known as the doubly differential electron emission yield, can be found by transforming the TOF distribution $\gamma(t, \theta)$ by

$$\gamma(\varepsilon, \theta) = \left| \frac{\gamma(t, \theta)}{\left(\frac{d\varepsilon}{dt}\right)} \right|. \tag{42}$$

Differentiating the above energy expression with respect to time, the doubly differential electron emission yield can be re-written as

$$\gamma(\varepsilon, \theta) = \frac{N_e t_e^3}{N_p \xi T \Omega \Delta_t m_e d^2}. \tag{43}$$

Due to the inability to measure the number of incident projectiles during the pulsed-beam data collection process, the number of scatter projectiles N_{sp} were used instead. This process required the normalization of these “relative” yields to published total backwards yields to be comparable. Due to the practicality of this process, the detector efficiency ξ, grid transmission coefficient T, and solid angle Ω were unnecessary constants for which normalization would compensate. Therefore the relative doubly differential electron yields can be written as

$$\gamma(\varepsilon, \theta)_{rel} = \frac{N_e t_e^3}{N_{sp} \Delta_t m_e d^2}. \tag{44}$$

An example of a relative doubly differential electron yield spectra, using the raw counts from Fig.27 is shown in red in Fig.28. Normalizing relative doubly differential electron yield spectra was done by measuring relative yields at many backward angles, then integrating over all energies and angles to compare total relative yields to previously measured total yields provided by Benka [16]. After measuring relative yields of several angles between 115

- 160°, integration yields over all energies for each angle

$$\gamma(\theta)_{rel} = \int_0^\infty \gamma(\varepsilon, \theta)_{rel} d\varepsilon \tag{45}$$

were calculated. Total relative yields were then found by integrating over all angles by extrapolating from 90 - 180° the function

$$\gamma_{rel} = \iint_0^{2\pi} \gamma(\theta)_{rel} sin\theta d\theta d\phi = 2\pi \int_0^\pi \gamma(\theta)_{rel} sin\theta d\theta. \tag{46}$$

This total relative yield number reported our estimated electron production per projectile in the backward scattering direction. When compared to the previously measured total backward electron yields, a normalization factor could be determined that could be used to scale our relative doubly differential electron yield spectra. An example of this scaling comparison is shown in Fig.28. For the remainder of this publication, an asterisk * will be used to denote relative yield spectra that have not been normalized to total yield data.

2.7 Target Preparation

Electron yields from proton and carbon ion interactions have been measured with gold foil, GNPs on silicon substrates, GNP thin film on TEM grids, and amorphous solid water targets. Considering the capabilities of current electron yield modeling techniques, high purity metallic targets offer the best method of comparison as this type of environment is more easily designed in simulation. An investigation into more complex solid state environments required collaboration and creative target choices.

2.7.1 Gold Foil

Gold foil manufactured by Goodfellow Cambridge Limited served as the primary target for system tests, comparisons, and normalization in this investigation. Sheets of 1 cm^2 99.9% pure 1 μm thick gold foil were clamped into the target assembly between two

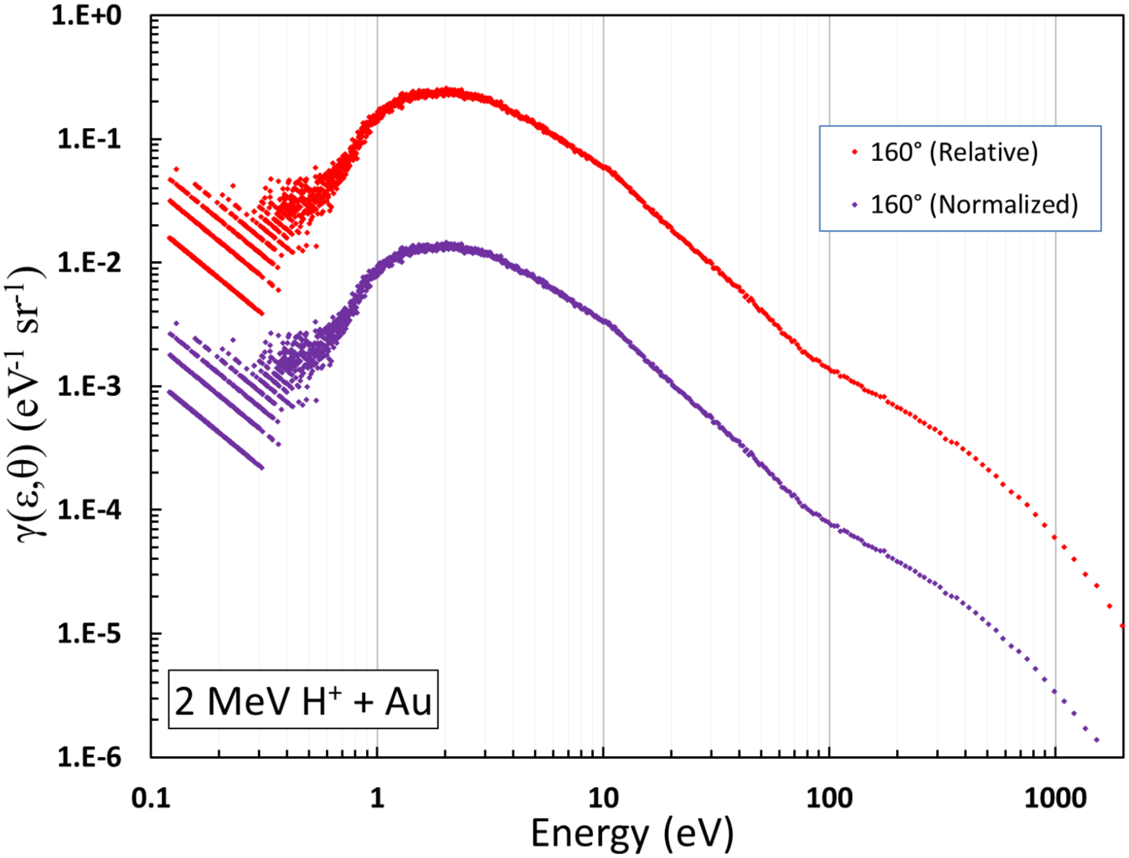

Figure 28: Example relative doubly differential electron yield (red) compared to normalized doubly differential electron yield (purple). the scaling factor for normalization was found by integrating relative spectra over energy and angle then comparing to total electron yield data.

beveled copper plates, as shown in Fig.20. This gold foil was resilient in UHV conditions, with heat (100°C), low temperatures (20 K), and ion gun sputter cleaning. During chamber bake-out, the gold foil target was also heated. Inevitably ambient particles did stick to the surface of the gold foil and affected the low energy region of the electron yield spectrum, so additional sputter cleaning was necessary to ensure a pure metallic surface. Energy loss through 1 μm of gold was calculated using the SRIM code previously mentioned. Exit velocities of the various ions used in electron yield measurements for this investigation are shown in Table 4.

Table 4: Energy-loss SRIM simulation results for projectiles used to measure electron emission yields.

Projectile	Incident Energy (MeV)	Exit Energy (MeV)	Exit Velocity (m/s)
H^+	1.00	0.87	1.29E+07
H^+	2.00	1.91	1.91E+07
H^+	4.00	3.94	2.75E+07
C^{2+}	2.40	0.39	2.51E+06
C^{2+}	6.00	2.73	6.62E+06

2.7.2 Gold Nanoparticles on Silicon Wafers

Silicon GNP targets were manufactured in-house by Dr. Katherine Tibbets at the Department of Chemistry, Virginia Commonwealth University [80]. Pulsed laser abblation in liquid (PLAL) of 5 - 13 nm diameter GNPs onto a silicon substrate was performed as described by Fojtík [81]. A 300 μm thick silicon wafer was submerged in a solution of $KAuCl_4$ (0.1 mM) and KOH (0.55 mM). A 30 fs pulsed 800 nm laser with an output fluence of 0.22 J/cm^2 was directed through a lens of focal length 50 mm. The silicon wafer surface was positioned 40 mm from the lens, creating an ablation spot size of 85 μm in diameter. A diagram of this experimental setup is shown in Fig.29. The resulting product was a sample of various sized GNPs both embedded and adhered to the surface of the silicon wafer. Transmission Electron Microscopy (TEM) images of centrifuged silicon-Au nano particles manufactured using this process are shown in Fig.30. The resulting size distribution of

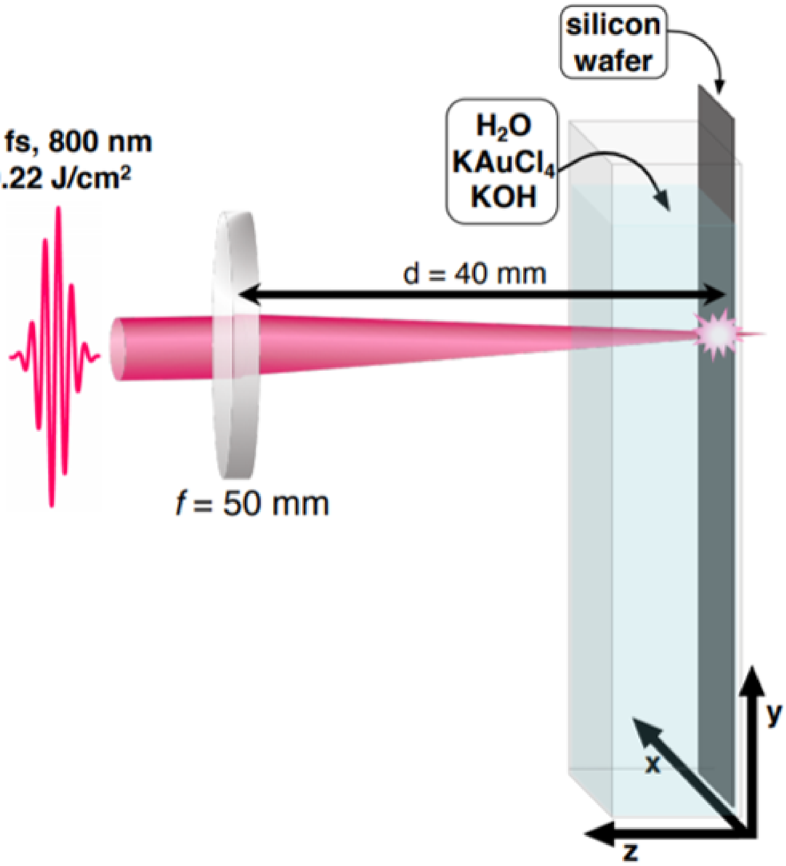

Figure 29: Diagram showing the high-intensity laser ablation process used to adhere GNPs onto the surface of silicon wafers. Fast laser pulses ablated the surface of a silicon surface submerged in an aqueous solution containing GNPs. Image adapted from Tibbets et.al. [80].

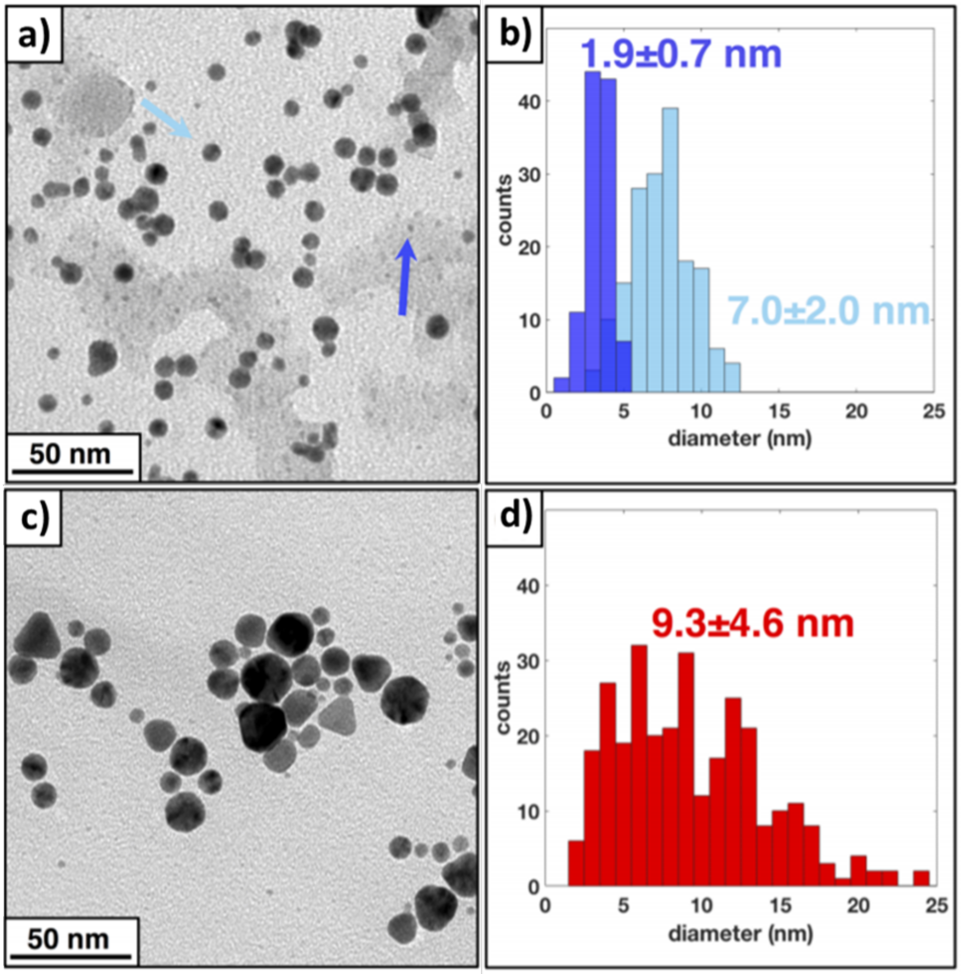

Figure 30: Transmission Electron Microscopy (TEM) images (a) of synthesized silicon GNPs embedded (dark blue arrow) into the silicon matrix and loose (light blue arrow) on the surface with size distribution (b). Scanning Electron Microscopy (SEM) images (c) of the control GNPs used in the diluted solution during the abblation process along with their size distribution (d). Images adapted from Tibbets et.al, [80].

GNPs for this target material ranged from 2 nm diameter for GNPs embedded in the amorphous silicon matrix to 7 nm diameter GNPs adhered to the surface. Optical microscope and TEM images of intact silicon GNP targets used for this investigation are shown in Fig.31. Patterns created by the moving-stage ablation process can be seen as deep grooves with clumps of SiGNPs forming a rough surface. Due to the 300 μm thickness of the silicon wafers, fast ion projectiles used in this investigation were completely attenuated. In order to measure electron yields from the surface of these samples, normalization of spectra through beam current comparisons were made, due to the lack of scattered projectiles in the Rutherford detector. Due to the inability to monitor the beam current in live time, an estimated average beam current was calculated from the instantaneous beam current measurements before and after each spectrum. The scattered projectiles N_{sp} number required for electron yield calculations was estimated from the number of scattered projectiles on gold foil under similar beam conditions.

2.7.3 Gold Nanoparticle Film on TEM Grid

Gold nanoparticle (GNP) monolayer film of thickness 4 - 6 nm, manufactured by Ted Pella Inc., was used as a target for this investigation. The manufacturing process is described by Allred et. al. in publication and U.S. Patent [82, 83]. GNPs were sputter-coated onto sucrose-enhanced 2% aqueous sodium dioctyl sulfosuccinate solution on glass slides. The GNPs were freed from this sacrificial substrate by methanol dissolution, then adhered to 300 mesh 3 mm wide gold transmission electron microscopy (TEM) grids. The grid windows were 58 μm with bar width of 25 μm, giving a 49% transmission rate for electron microscopy. An artist rendering of the described thin GNP film on gold 300 mesh grid and an electron microscope image of the GNP film is shown in Fig.32. Electron microscopy showed monolayer thick bunched GNPs with few-atom gaps of disorganized remaining substrate material acting as an adhesive. An image created by electron microscopy, along with size specifications for various films provided by the manufacturer, are shown in Fig.33. Extra considerations

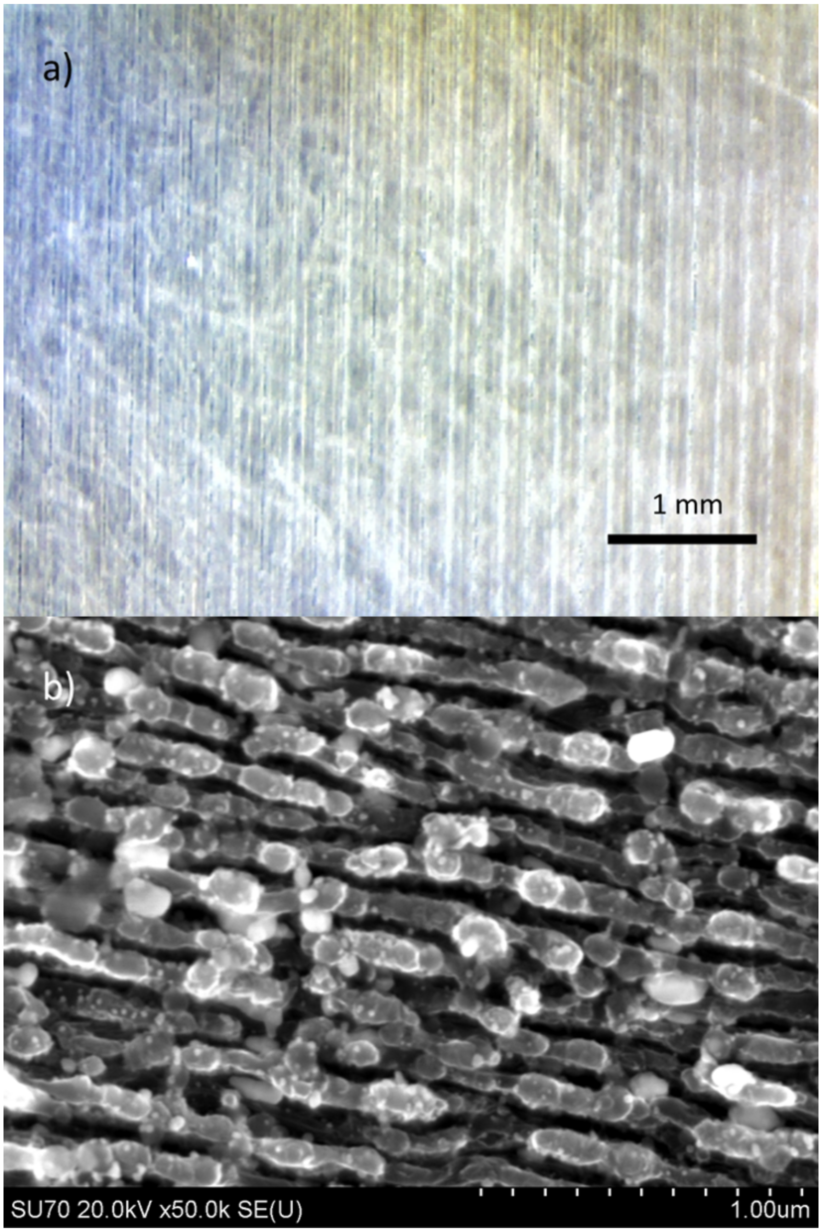

Figure 31: Surface images of the silicon GNP targets used for this investigation taken by an optical microscope at ECU (a) and TEM at VCU (b).

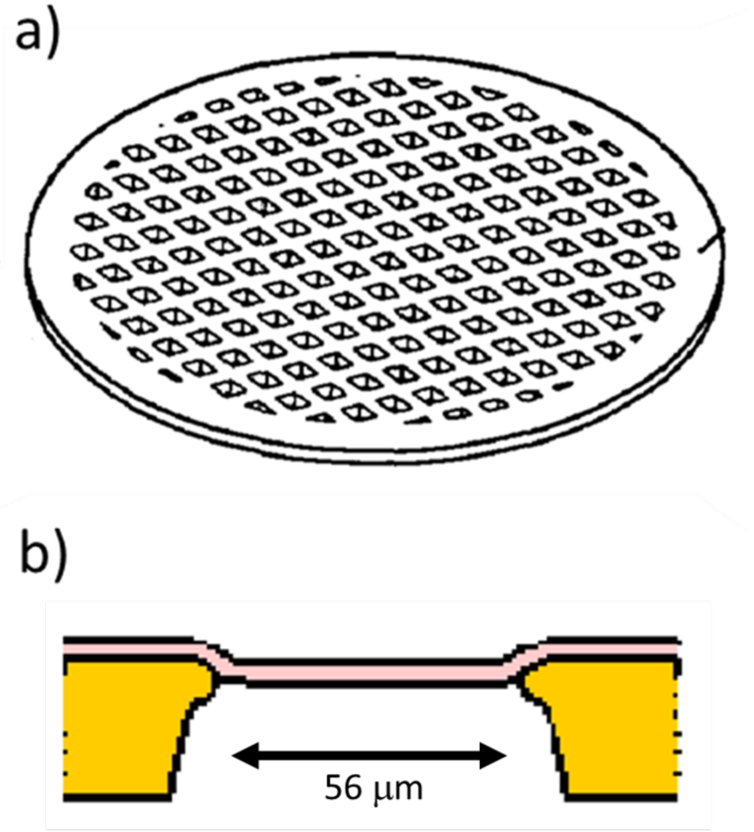

Figure 32: Artist rendering of an example 3 mm wide 300 mesh gold TEM grid (a) and side view illustrating the 4 - 6 nm thick GNP film (b) adhered to one side. [83].

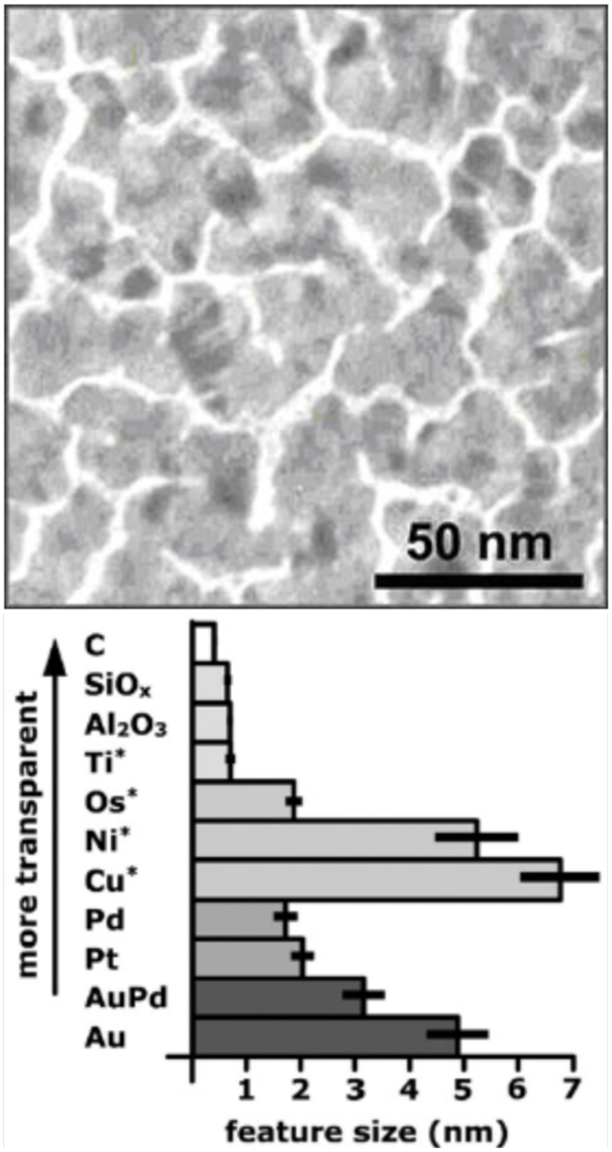

Figure 33: Electron Microscope image of the 4 - 6 nm GNP film used during this investigation. Below the image is a size estimation plot provided by the manufacturer for various films, including GNPs. Images adapted form Allred et.al. [82].

were made for this target including never allowing unpulsed beam exposure, never using the flash heater in the target assembly, and only using neon gas to sputter clean the surface. Sputter cleaning with argon gas was shown to completely disintegrate the GNP film from the grid. Only back scattered electron emission analysis was possible with the GNP film targets due to the design of the target only having film on one side. Furthermore, angular distribution of electron emission was not investigated for this target as it was unclear how the grid bars geometry would influence the spectrum. There was no known total yield measurements for this type of target, so normalization was not possible. Scaling of the electron yield measurements done with GNP film was performed using normalized gold foil spectra for comparison. The main advantage this target provided over the silicon GNPs was the projectile transmission, allowing scattered projectile measurements for comparison between this target's spectra without the need for beam current normalization mentioned in the previous section.

2.7.4 Amorphous Solid Water

Deionized (DI) water was stored in a 4 in. x 1 in. stainless-steel cylinder tank and connected to the gas leak valve on the UHV chamber. This tank was frozen in liquid nitrogen and evacuated multiple times. Frozen DI water was exposed to rough vacuum (1×10^3 Torr) to reduce nitrogen and other background gass from the water sample. The DI water would then be thawed and re-frozen in liquid nitrogen repeatedly to improve purity. Tests were performed using a Residual Gas Analyzer (RGA) to show that after three cycles of freeze-thawing, the nitrogen and other particulate content concentration in the DI water had converged. The final product of freeze-thawing DI water is referred to as ultra-high purity water. The base pressure obtained solely using the turbomolecular pump was less than 1×10^7 Torr. An example RGA spectrum of this high-vacuum environment is shown in Fig.34. After baking out the chamber and flashing the titanium sublimation pump, using the process previously discussed, the chamber pressure reached pressures of less than

1×10^9 Torr. An RGA spectrum of this ultra-high vacuum environment is shown in Fig.35. A spectrum of the ultra-high purity water leaked into the UHV chamber during ultra-high vacuum conditions is shown in Fig.36. Before freeze-thawing, the partial pressure peak of nitrogen in the DI water made up roughly half of the total pressure under these conditions. Water targets were created using this ultra-high purity water to simulate biological material. Under these ultra-high vacuum conditions, leaking water into the UHV chamber would result in adhesion of water to the target surface in a crystalline lattice. In order to more closely resemble liquid water, the target was chilled to low temperatures in order to achieve flash freezing of the water vapor in the form of amorphous solid water (ASW). The target assembly was chilled to roughly 20 K using a compressed helium cold finger, shown in Fig.20. At this low temperature, one mono layer (measured in units of Langmuir) of amorphous solid water is formed per second in a 1×10^6 Torr environment [84]. During ASW buildup, a pressure of 1×10^7 Torr ultra-high purity water was leaked into the UHV chamber, generating 1 L per 10 seconds.

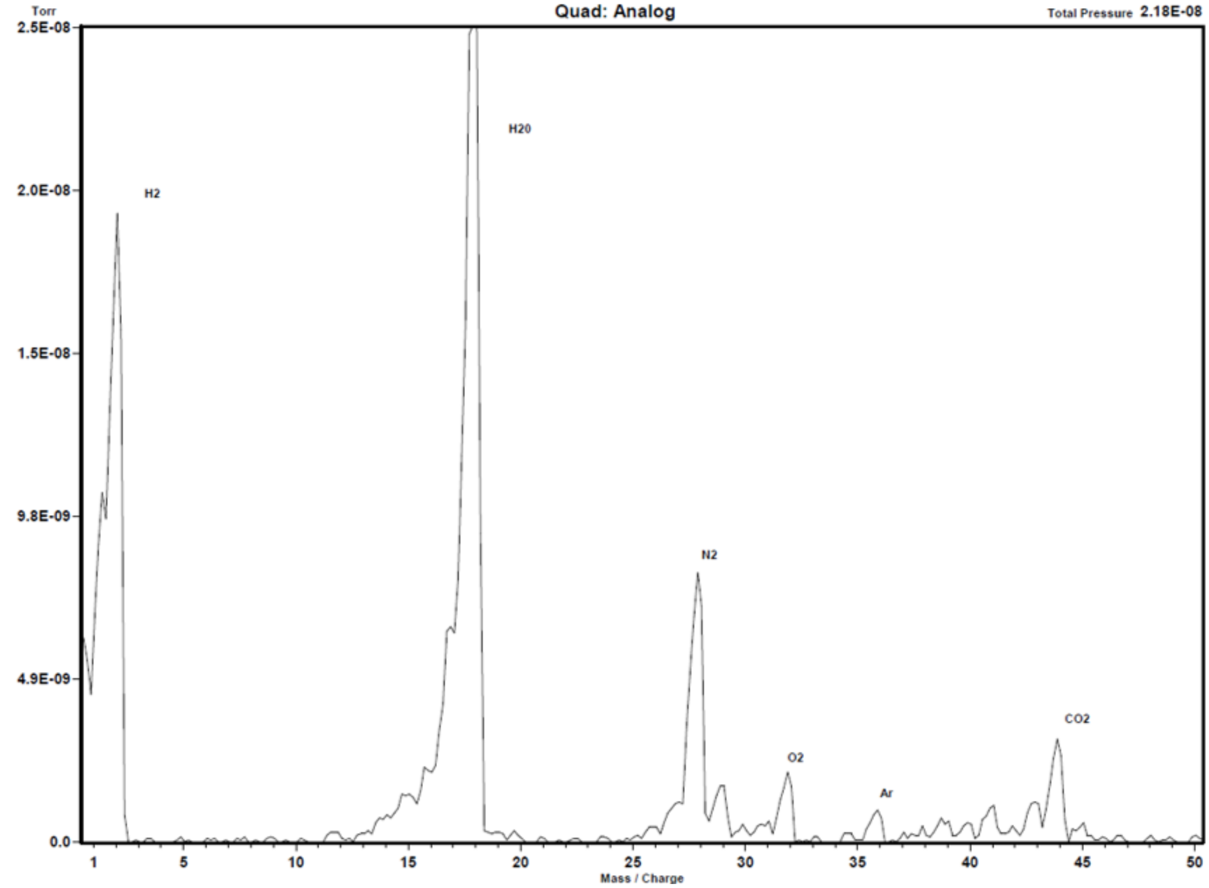

Figure 34: Residual Gas Analyzer spectrum of the base pressure in the UHV chamber, using only the turbomolecular pump.

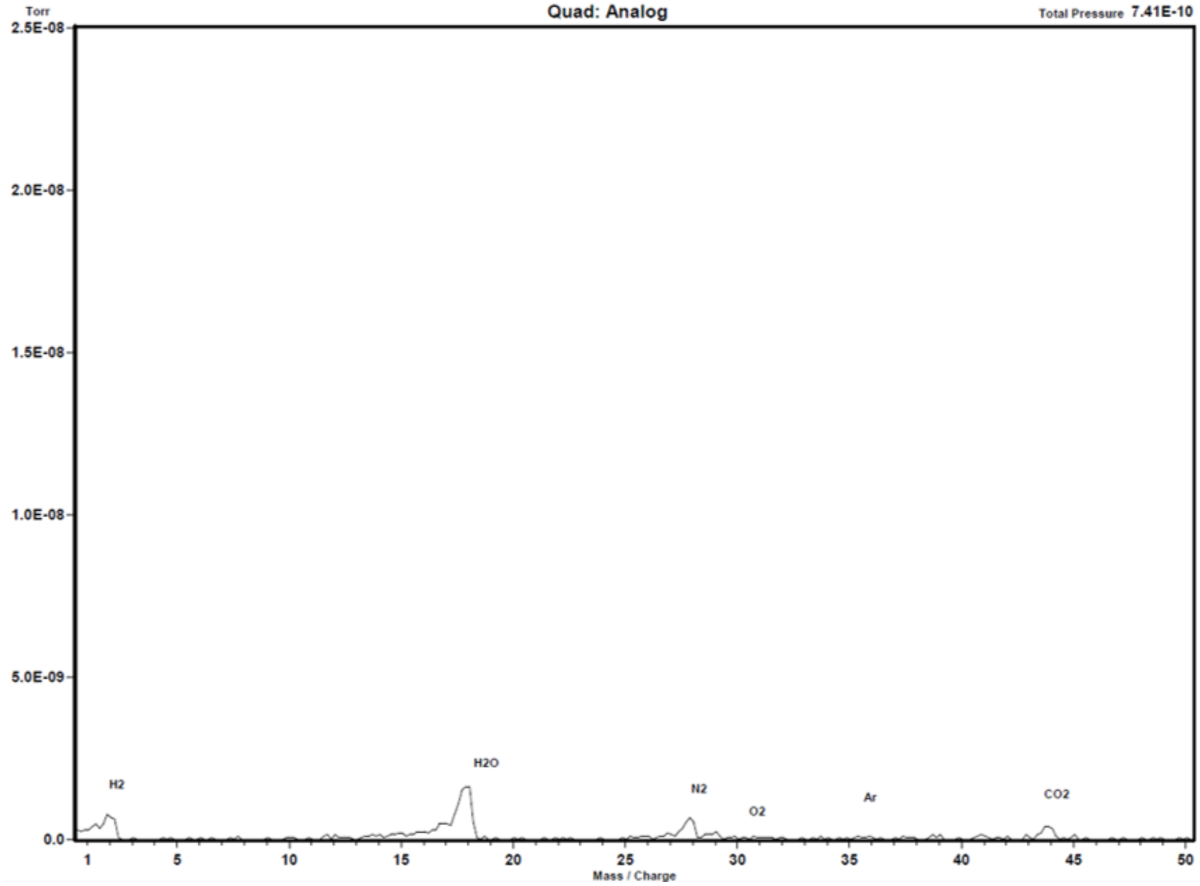

Figure 35: Residual Gas Analyzer spectrum of the post bake-out pressure in the UHV chamber. This procedure involved heating the chamber to 100°C for 48 hours.

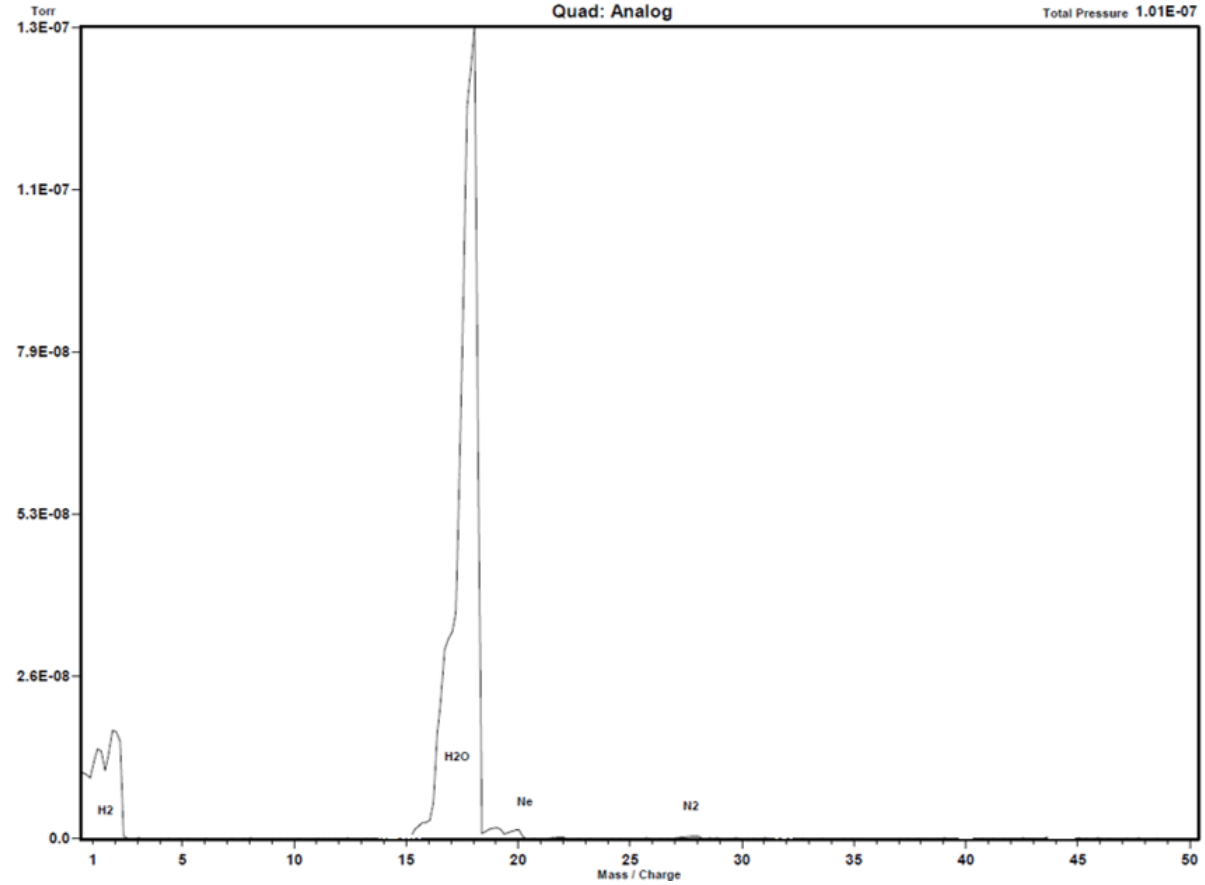

Figure 36: Residual Gas Analyzer spectrum of the ultra-high purity deionized water leaked into the UHV chamber used to build amorphous solid water targets.

3 Results and Discussion

Doubly differential electron emission yields, in angle and energy, from solid state targets were measured for fast proton and fast carbon ion interactions with gold foil and gold nano particle (GNP) targets coated in amorphous solid water. These measurements serve as vital comparison tools for Geant4 monte carlo simulations, as well as key insight into secondary electron emission in biological environments. This study aimed to directly measure both spatial and energy distributions of secondary electron emission near the Bragg peak for direct application to the study of malignant tissue killing in the treatment of cancer with ion beam therapy. Firstly, a complete study was performed on the spatial and energetic distribution of electron emission from proton and carbon-ion impact on 1 μm gold foil under-high vacuum and high target purity conditions in order to establish a method of normalization to total backwards yields previously measured by Banka et.al. [16]. Additionally, 1 μm gold foil was used as a substrate for amorphous solid water target production, as described in the previous chapter. Lastly, electron emission from more complex GNP targets were measured as a comparison study to gold foil to address theoretical questions concerning surface plasmon resonance effects, as well as investigate the practical application of GNPs acting as radiosensitizers during ion beam therapy. Targets used for this investigation included gold foil, GNPs embedded in amorphous silicon lattice and GNP film on TEM grid substrate.

3.1 System Tests

Various system tests were performed to ensure accurate electron emission measurements. During the construction of the UHV chamber, transit sighting, chamber 3-point stand height adjustments, and TOF detector translation manipulation were necessary for beam alignment. After development of the data analysis system described in the previous chapter, TOF detector alignment tests were performed at multiple angles to ensure optimal throughput of the entrance collimator to the MCP assembly. An example of the effects on carbon-ion induced electron yield spectra from misalignment are shown in Fig.37, where the TOF detector was intentionally moved off alignment in the "x" transverse direction, with respect to the ion beam while positioned at 160°. As this figure shows, misalignment on the order of just a few millimeters will result in a complete loss in electron emission detection. Pitch and yaw of the chamber, proper alignment of the experimental beamline, and TOF detector alignment were all necessary to obtain usable spectra.

Electronics tests were performed to ensure proper electrical connections in the UHV chamber, as well as in the data processing components used for signal analysis. During all electron emission measurements, the target assembly was grounded as to prevent charge buildup from the incident beam. Floating target and biased target tests were performed to ensure a proper connection to ground via UHV electrical feedthroughs. A shift in proton-induced electron yield and energy can be seem in Fig.38 due to a bias of 1.5 V. A negative bias increased yields and lowered the escape energy of secondary electrons while a positive bias decreased the electron yields and increased the required escape energy for electrons emitted from the surface of gold foil. Signal analysis tests were performed after optimizing signal amplification and discrimination for TAC and MCA use. One such test is shown in Fig.39, where the signal discrimination was increased from 2.0 to 5.0 (arbitrary scale) to investigate the relationship between electron energy and signal amplitude. The discrimination increase test shows an even distribution of electron yield reduction across all energies, confirming the stochastic nature of random output signal amplitude variance. This test was one example of eliminating equipment uncertainty in pre-normalization relative yield spectra, similar to the theoretical variable elimination in the relative doubly differential electron yield proof discussed in the previous chapter.

Target cleaning by sputter ion guns, as discussed in the previous chapter, was done to ensure high-purity target surfaces by removing impurities. To ensure a convergence to a clean surface, tests were performed by measuring electron yields from "dirty" to 40 minutes of cleaning every 5 minutes. This was done for both argon and neon gases used for sputter

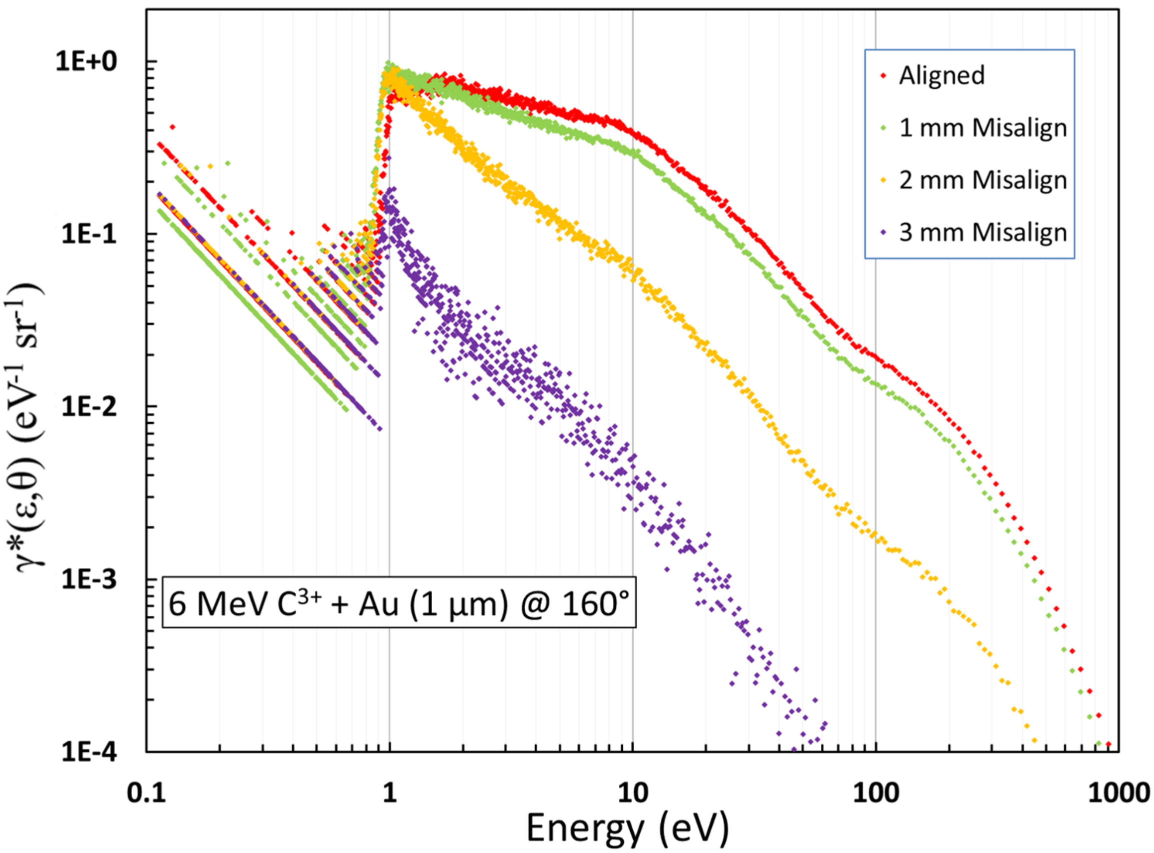

Figure 37: Target alignment tests, showing a decrease in yields by shifting the collimated TOF detector by 1, 2, and 3 mm in the "x", or transverse, direction using the moving stage mounted to the top of the UHV chamber.

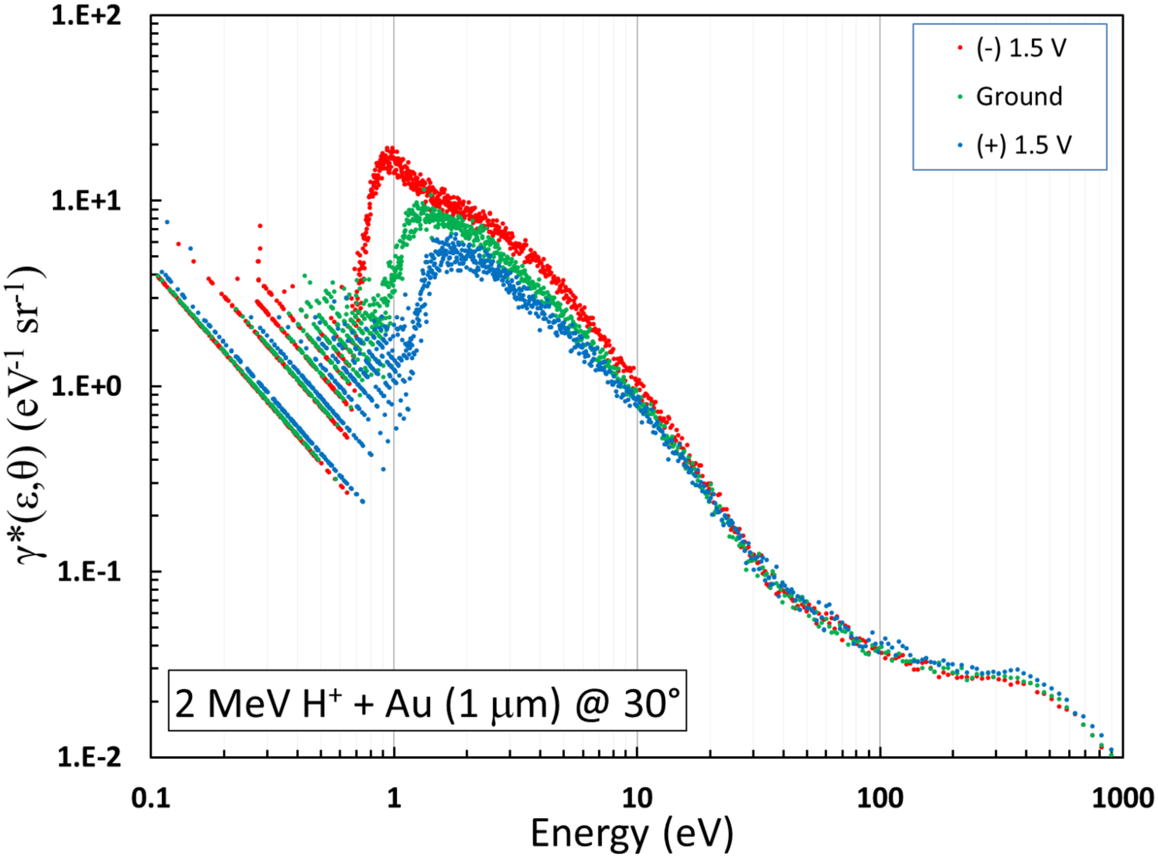

Figure 38: Target bias tests, showing a shift in low-energy electron production from fast proton interactions with gold foil.

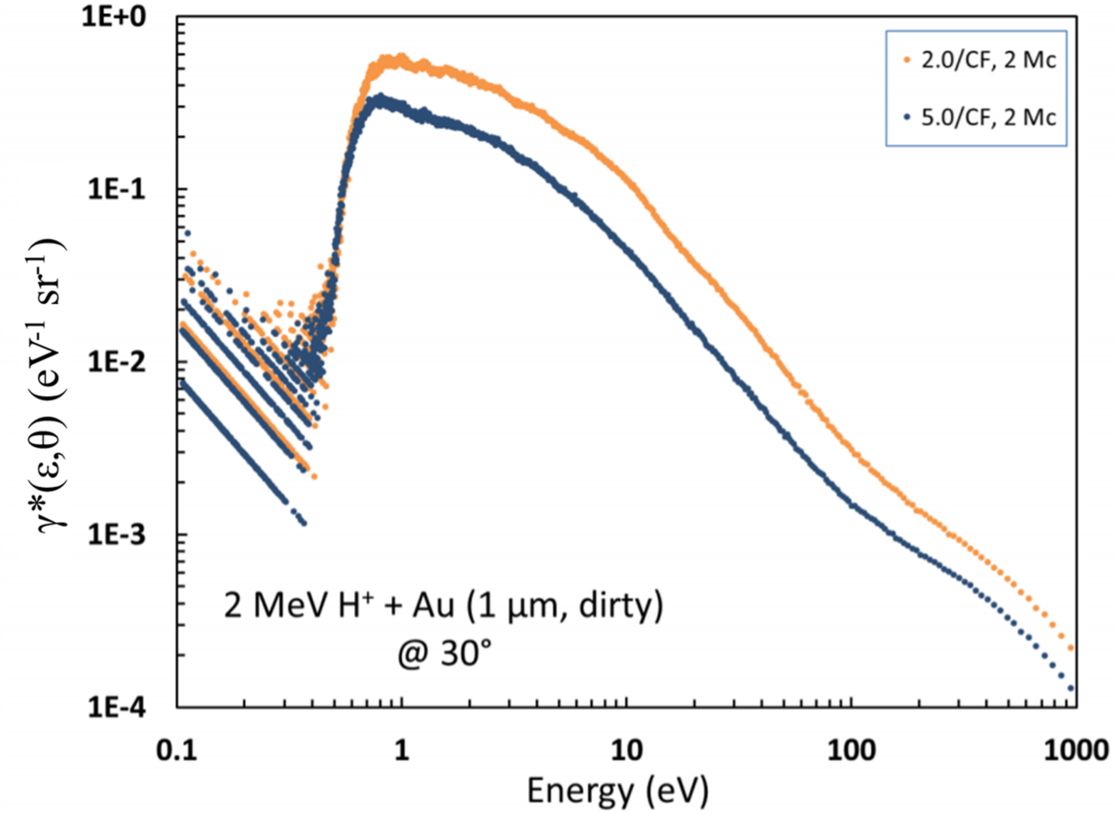

Figure 39: Signal discrimination tests, an even reduction in electron yields across all energies for an increase in signal discrimination.

cleaning in both normal and low temperature conditions. After only 5 minutes of cleaning, the electron yield spectrum converged to a point of "clean" for which no further sputter cleaning made a difference. During this cleaning process, a reduction in low-energy electron emission was observed and is plotted in Fig.40. The electron yields spectra shows a significant shift in the low energy electron "shelf" on the left side of the plot, indicating a loss in low energy electron production.

The process of making measurements under the experimental conditions of accelerator physics involves the cooperation of components from the ion source, accelerator, beamline, experimental chamber, detectors and data acquisition system. Ion source cathode changes, natural stripper gas bottle pressure decreases, minor deviations in alignment from target changes, and normal wear and tear on various circuitry were regularly compensated for through various adjustments in oven temperatures, beam optics settings, collimator position changes, detector alignment, and data analysis electronics optimization. The measurements for this investigation were made over the course of several years, during which time systems outside and inside of the experimental apparatus were changed and updated. Due to this large parameter space that was constantly evolving, tests were performed to measure the systematic error of electron yield measurements periodically as a comparative analysis for spectra spanning several months. One such example of a systematic error test is shown in Fig.41. This plot shows a compilation of "clean" proton induced electron emission spectra taken over the course of several weeks at ambient and low temperature (44 K) ranges. An average of these spectra was found and was plotted in black. A maximum variance in electron energy of roughly 15% was found at multiple average yield energies.

3.2 Doubly Differential Electron Yields from Gold Foil

Doubly differential, in angle θ and energy ε, electron yields $\gamma(\varepsilon, \theta)$ from fast proton and carbon ion interactions with gold foil were determined from relative doubly differential electron yields $\gamma(\varepsilon, \theta)_{rel}$ measurements that were normalized to total yield measurements

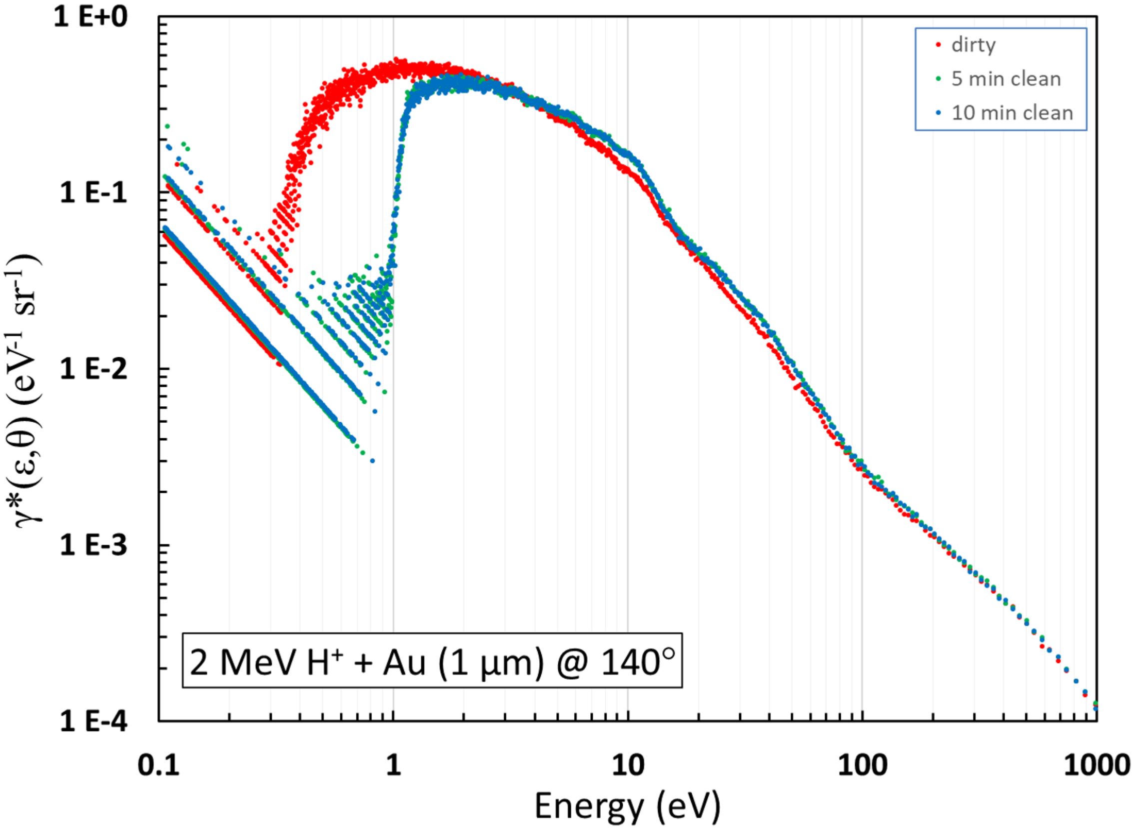

Figure 40: Electron yield spectra from gold foil before cleaning and after 2 subsequent cleanings. Shown above is the convergence to a "clean" state after only 5 minutes of argon sputter gun exposure.

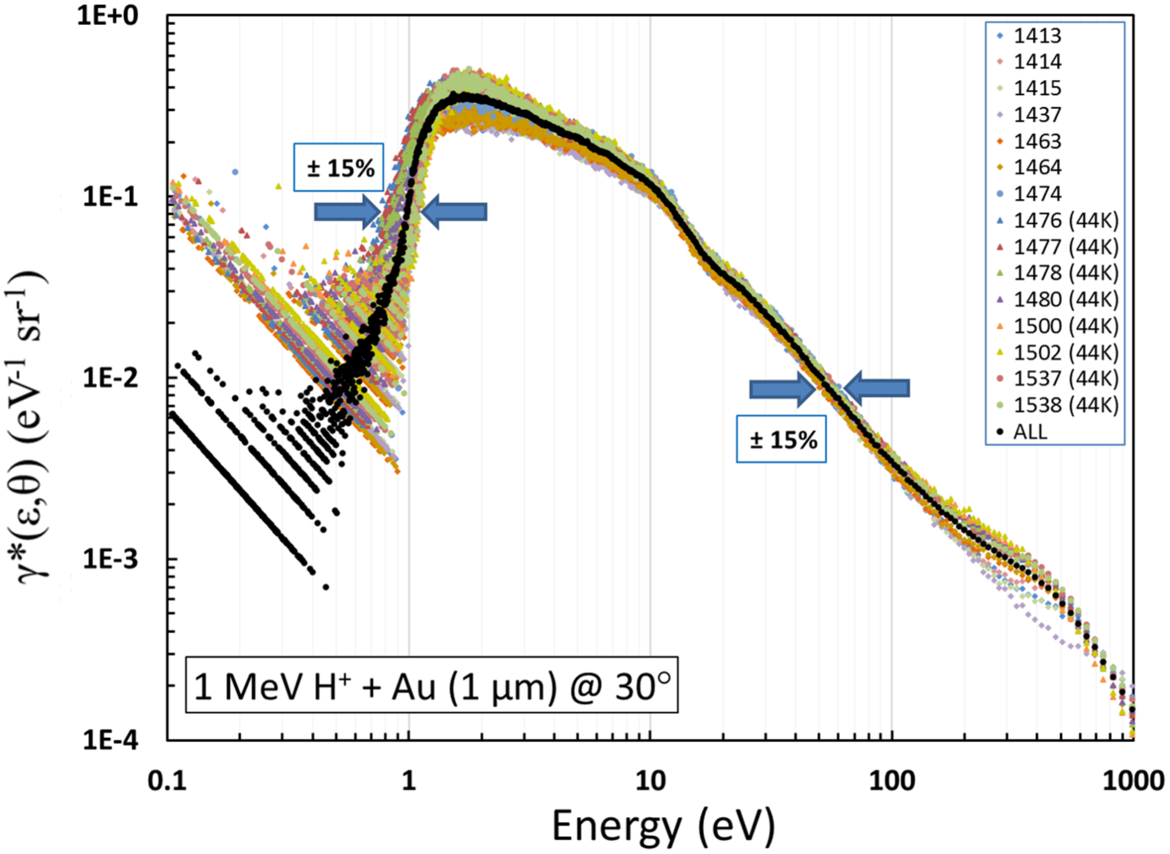

Figure 41: Systematic error tests showing many similar "clean" runs taken over a span of several weeks both room temperature, as well as low temperature (44 K). The numbers labeled in the legend are arbitrary run numbers used to identify spectra over the span of several years.

made by Benka and Koyama [16, 26]. In order to find the scaling coefficient for normalization, electron emission spectra were found for many back-scattered angles, then fit to a polar function and integrated over all angles and energies. All spectra presented in this section were measured in an irregular pattern, as opposed to sequentially in increasing or decreasing angle. This was done to compensate for any systematic error from other lab components including degradation of an ion source cathode over the course of a 12 hour run or pressure fluctuations in accelerator stripper gas. Relative electron yield transformation from raw counts data does account for changes in TOF detector count rate due to fluctuations in beam current due to the yields depending on scattered projectiles, which scale linearly with beam current. Each angular spectrum presented here is a compilation of five or more 5 minute runs, with sputter cleaning performed between each 5 minute run. Many of the compilations were done using individual runs spanning weeks or months of time.

3.2.1 Protons on Gold Foil

Doubly differential electron yields were previously measured by Dr. Robert McLawhorn for 2 MeV proton interactions with aluminum, copper, and gold foils [3]. To extend the energy range for proton interactions with gold foil, 1 MeV and 4 MeV protons on gold foil measurements were made. These near Bragg peak energies cover the full range of fast proton energies available at the ECU Accelerator Laboratory. The central terminal of the accelerator was set to 0.5 MV to produce 1 MeV protons. Any central terminal voltage below this threshold resulted in a steep decline in accelerator throughput yields from roughly 50% ionization of H^- into H^+ to less than 1%. Attempts were made to measure doubly differential electron yields from 500 keV and lower H^+, but this resulted in a count rate decline on the TOF detector from roughly 500 cps to less than 10 cps, which is within the noise range for the MCPs.

Doubly differential electron yields for 1 MeV proton interactions with 1 μm gold foil is shown in Fig.42. Due to the nature of the experimental design, the forward scattered

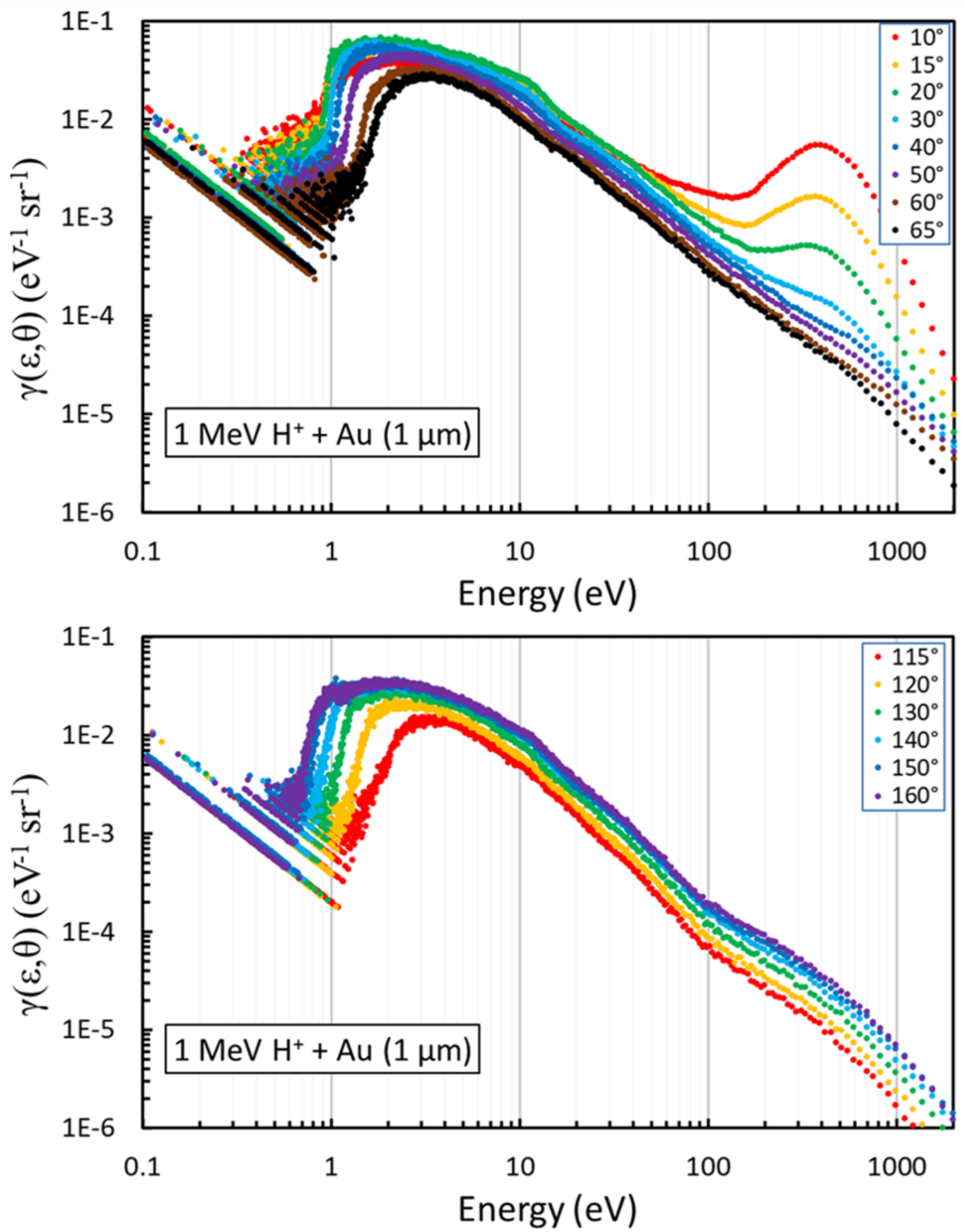

Figure 42: Doubly differential electron yields from 1 MeV proton interactions with gold foil. Forward (top) and backward (bottom) scattered angles are normalized to total electron yields.

yields contain scattered proton projectiles at small angles. The MCPs used in the TOF detector generate electron cascades, as described in the previous chapter, upon collection of photons, electrons, or any charged ion. These forward scattered proton projectiles appear in the spectrum on the right side in the 200 - 1000 eV range. As seen in Fig.42, the smaller the angle, the more incident projectiles are seen in the spectrum. In general, the forward scattered electron yields decrease as the TOF detector approaches 90°. The exception to this trend occurs in the small angles 10° and 15° where the low energy electron yield tends to show the opposite trend. This relatively lowered low energy electron yield for small angles is due to the nature of the TOF data analysis system. Due to the higher number of high energy events, due to the added scattered projectile events, some of the low energy electrons that would have been counted during a 500 ns collection window of the TAQ were missed. An early fast projectile caused the data acquisition system to trigger the stop, eliminating the opportunity for another longer time-of-flight event to be counted. As shown in Fig.42, electron yields decrease as the TOF detector approaches 90°. The scattered proton projectiles are not seen in the back scattered yields, and there is no local decrease in low energy electron yields when approaching 180°. This allows confidence in normalization as the backward angles were used to calculate scaling coefficients using backward total yield measurements.

Doubly differential electron yields for 2 MeV and 4 MeV proton interactions with gold foil are shown in Fig.43 and Fig.44 respectively. Evidence of the same forward scattered projectile events occurring for small angles can be seen for both higher energy proton projectiles. A relative decrease in scattered projectiles is apparent as the incident proton projectile energy increases. This trend clearly shows a decrease in solid angle scattering for increasing incident energy. Normalization of the 1, 2, and 4 MeV proton on gold spectra was calculated as shown in the previous chapter by integrating the backward scattered angle spectra over all energies, summarizing each spectrum to a single point on a singly differential electron yield $\gamma(\theta)$ plot. This singly differential yield plot is shown in Fig.45. A linear fit of the $\gamma(\theta)$ for five angles of forward and backward spectra for all three proton energies was

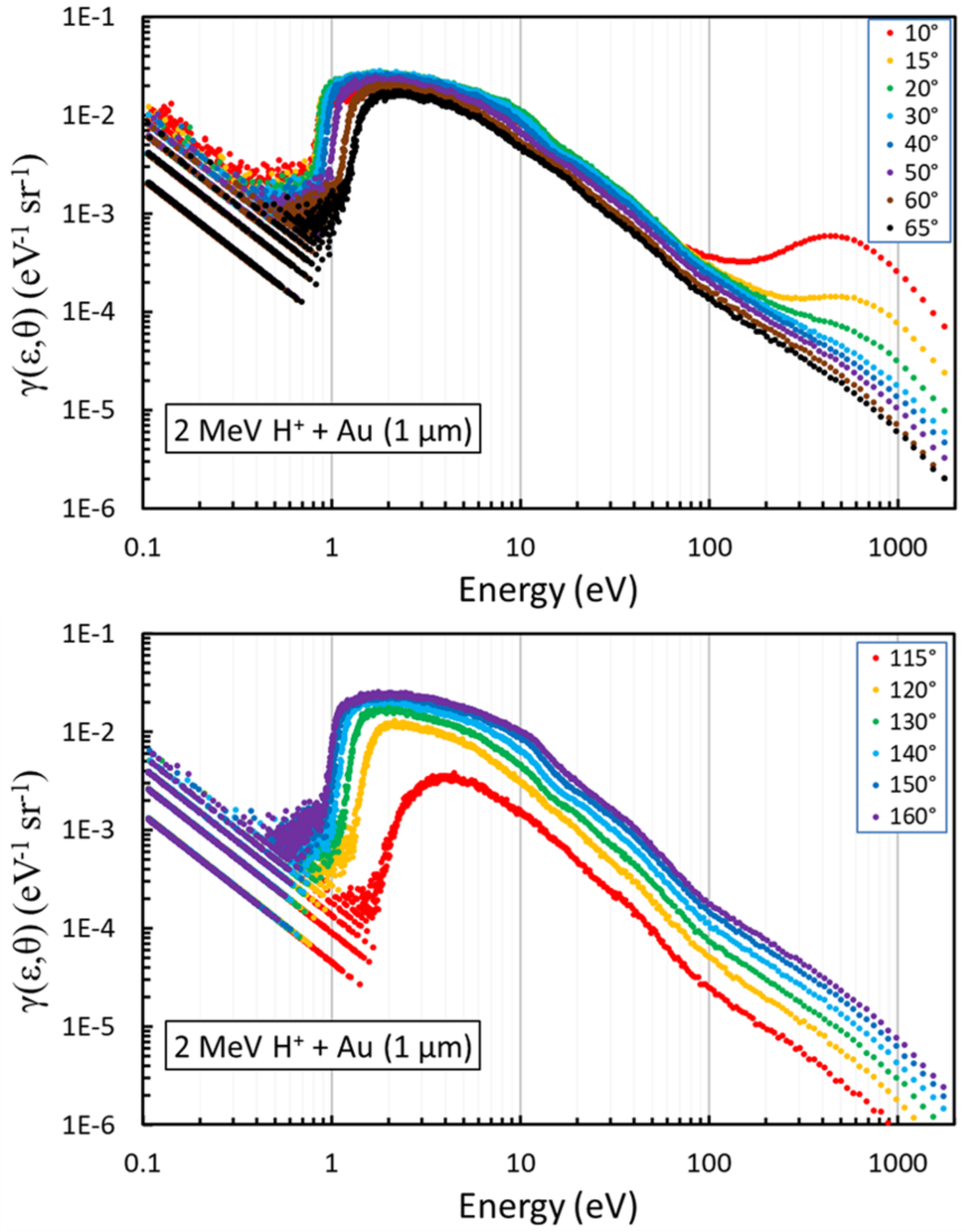

Figure 43: Doubly differential electron yields from 2 MeV proton interactions with gold foil. Forward (top) and backward (bottom) scattered angles are normalized to total electron yields.

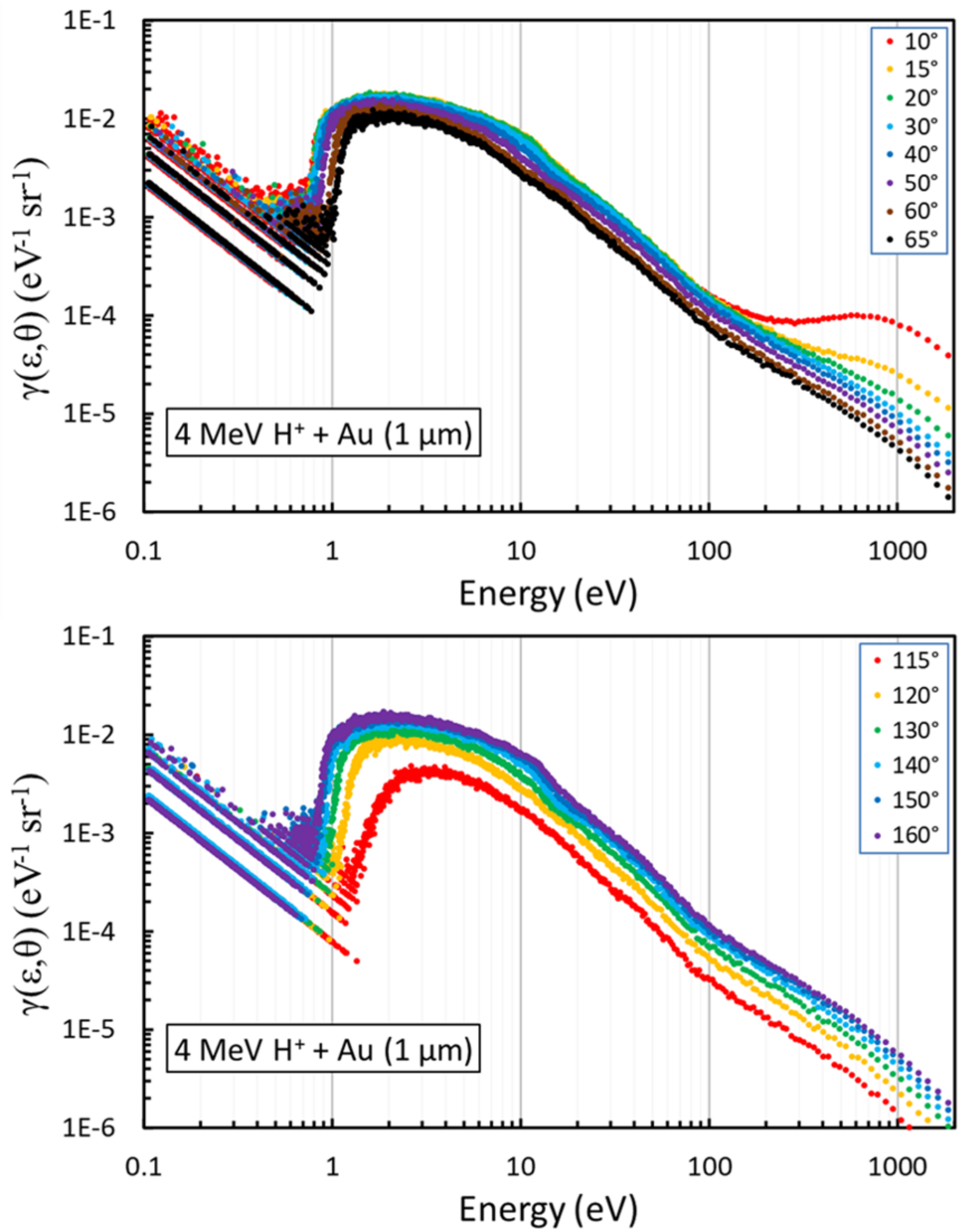

Figure 44: Doubly differential electron yields from 4 MeV proton interactions with gold foil. Forward (top) and backward (bottom) scattered angles are normalized to total electron yields.

found. Integrating the area under the back scattered linear fits gave a relative total yield of 6.8, 16.8, and 21.9 electrons per incident proton for 1, 2, and 4 MeV incident energy respectively. This far overestimates total yield measurements of 1.27, 0.91, and 0.65 electrons per incident proton from 1, 2, and 4 MeV respectively [16, 26]. Scaling factors of 0.19, 0.05, and 0.03 for 1, 2, and 4 MeV were applied to all relative doubly differential electron yields to produce the normalized plots shown in Fig.42, Fig.43, and Fig.44. One example of this scaling effect was demonstrated in the electron yields section of the previous chapter in Fig.28. A direct comparison plot of these three normalized doubly differential electron yield spectra for a single forward and a single back scattered angle are shown in Fig.46. A general decrease in electron yield is shown for increasing projectile energy, as would be expected. Electron yield should increase as projectile energy approaches the Bragg peak energy of 200 keV. In general, the TOF method used here to measure electron yields is considered reliable in the low energy (1 - 100eV) range. The discrepancies shown for the “cut off” energy shelf on the left side of the plots in Fig.46 are within less than 1 eV, and simply show a transition from detectable slow electrons to the right of the shelf to single counts in the raw count histogram to the left of the shelf. Although TOF spectra are unreliable over 100 eV, a convergence to similarly low yields on the high energy side of the spectra can be noted.

3.2.2 Carbon Ions on Gold Foil

Doubly differential electron yields were measured for fast carbon ion interactions with gold foil. The incident carbon projectiles used for this investigation were 2.4 MeV and 6 MeV C^{2+}. Doubly ionized carbon ions were chosen due to a relatively high yield when compared to other charge states produced by stripper gas ionization. This C^{2+} charge state of carbon allowed for investigation into the carbon ion Bragg peak of 200 keV/AMU. By setting the central terminal to 0.8 MV, a C^{-} ion entering the accelerator gained 0.8 MeV in energy, and with probabilistic ionization to C^{2+} gained another 1.6 MeV on the exit. Setting the central terminal of the accelerator below the 1 MV threshold, as discussed in the previous section,

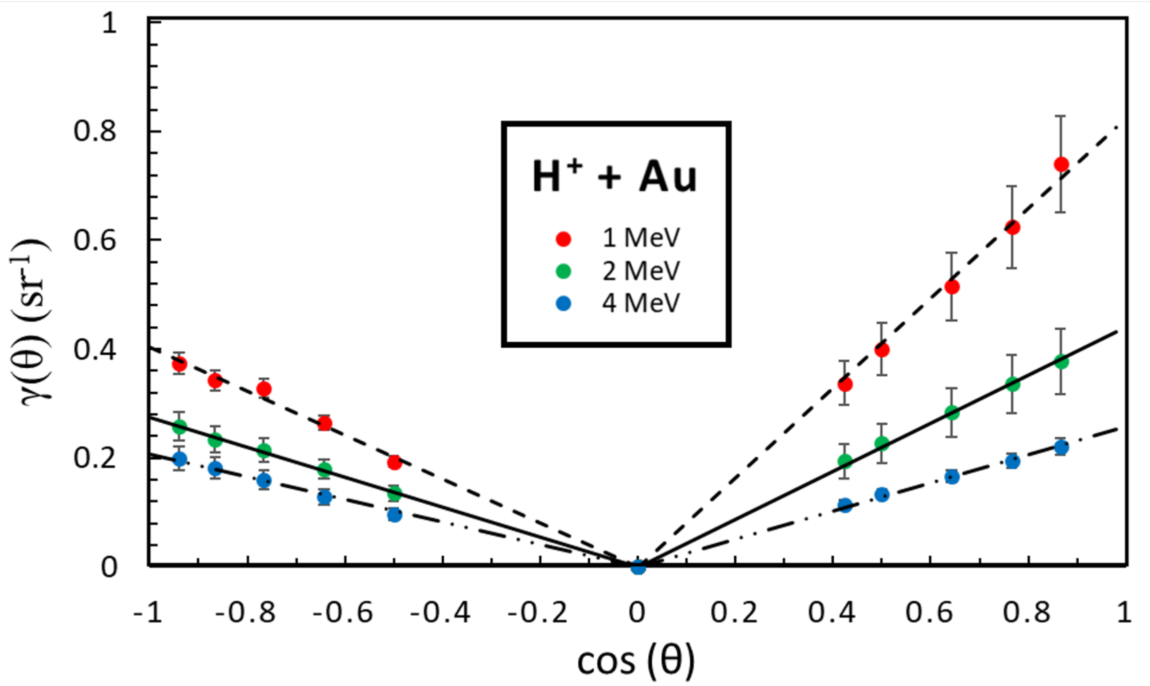

Figure 45: Plot of singly differential electron yields, in angle, for 1 - 4 MeV proton interactions with gold foil. The fit lines shown here were made by integrating five forward angle spectra (right of center) and five backward angle spectra (left of center) over all energies. Integrating over the backward angles here gives a relative total electron yield factor that can be used to find the normalization factor of measured total yields.

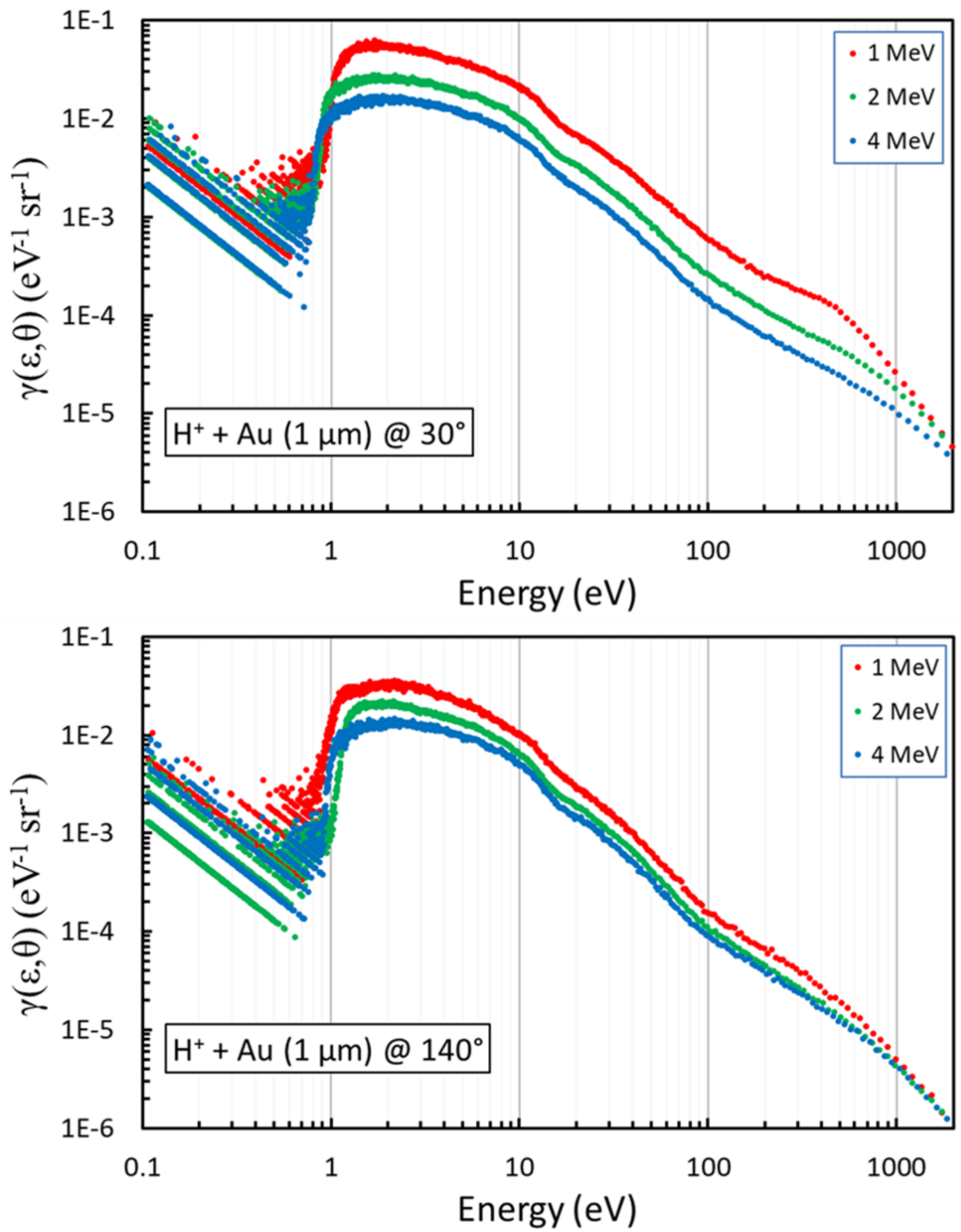

Figure 46: Doubly differential electron yield comparisons for 1 - 4 MeV proton interactions with gold foil at 30° (top) and 140° (bottom).

leads to a steep decrease in accelerator throughput yields and could account for a lessened resolution when compared to proton spectra. One major difference in the 2.4 MeV carbon ion spectra was the exit energy of the incident projectiles through the 1 μm foil. Using SRIM to calculate the expected projectile energy attenuation, an exit energy of 0.4 MeV was found for 2.4 MeV incident C^{2+} and an exit energy of 2.7 MeV was found for 6 MeV incident C^{2+}. Major adjustments to the data acquisition system were made to compensate for this timing difference. It should be considered that the forward scattered electron yields, unless produced early in the projectiles path through the foil target, were produced by a far lower energy ion than the reported incident projectile energy.

Doubly differential electron yield spectra for 2.4 MeV incident carbon ions, presented in Fig.47, were normalized to Itoh et.al. total yield measurements of 16 electrons per proton for 0.2 MeV/AMU C^{+} projectiles [25]. A relative electron yield of 7.5, found by integrating the linear fit made by a singly differential electron yield $\gamma(\theta)$ plot of back scattered spectra using the method described previously. All relative yields from 2.4 MeV carbon ion interactions with gold foil were scaled by a factor of 2.1, producing the normalized doubly differential electron yields shown here. Electron yields in the region of interest (0.1 - 100 eV) are roughly an order of magnitude greater than the lowest energy proton yield spectra (1 MeV) taken for the same target. This is to be expected as 2.4 MeV carbon is in the Bragg peak energy range of 0.2 MeV/AMU. It should be noted that the electron yields for energies over 50 eV for both forward and backward scattered electrons steeply decline when compared to proton interaction spectra.

Doubly differential electron yields for 6 MeV carbon ions are presented in Fig.48. A general increase in electron yields by an order of magnitude when compared to proton spectra is seen for most angles in 6 MeV carbon interactions, similar to 2.4 MeV carbon spectra. This energy of carbon projectile is equivalent to 0.5 MeV/AMU, and has more similarities to the 1 MeV proton spectra than the 2.4 MeV carbon ion yields. A relatively lower electron yield in the low energy range is seen for small forward angles, similar to 1 MeV proton

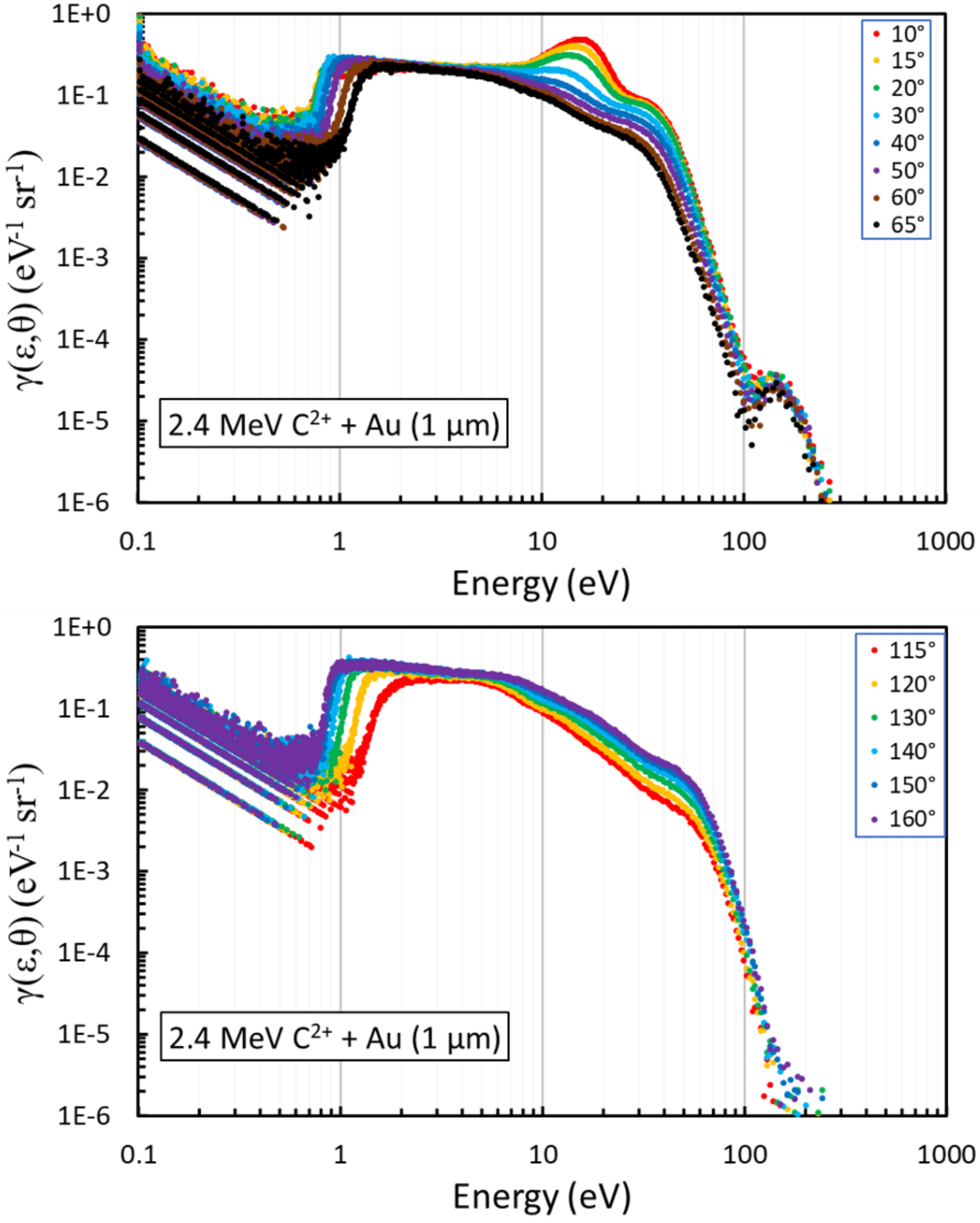

Figure 47: Doubly differential electron yields from 2.4 MeV carbon ion interactions with gold foil. Forward (top) and backward (bottom) scattered angles are normalized to total electron yields.

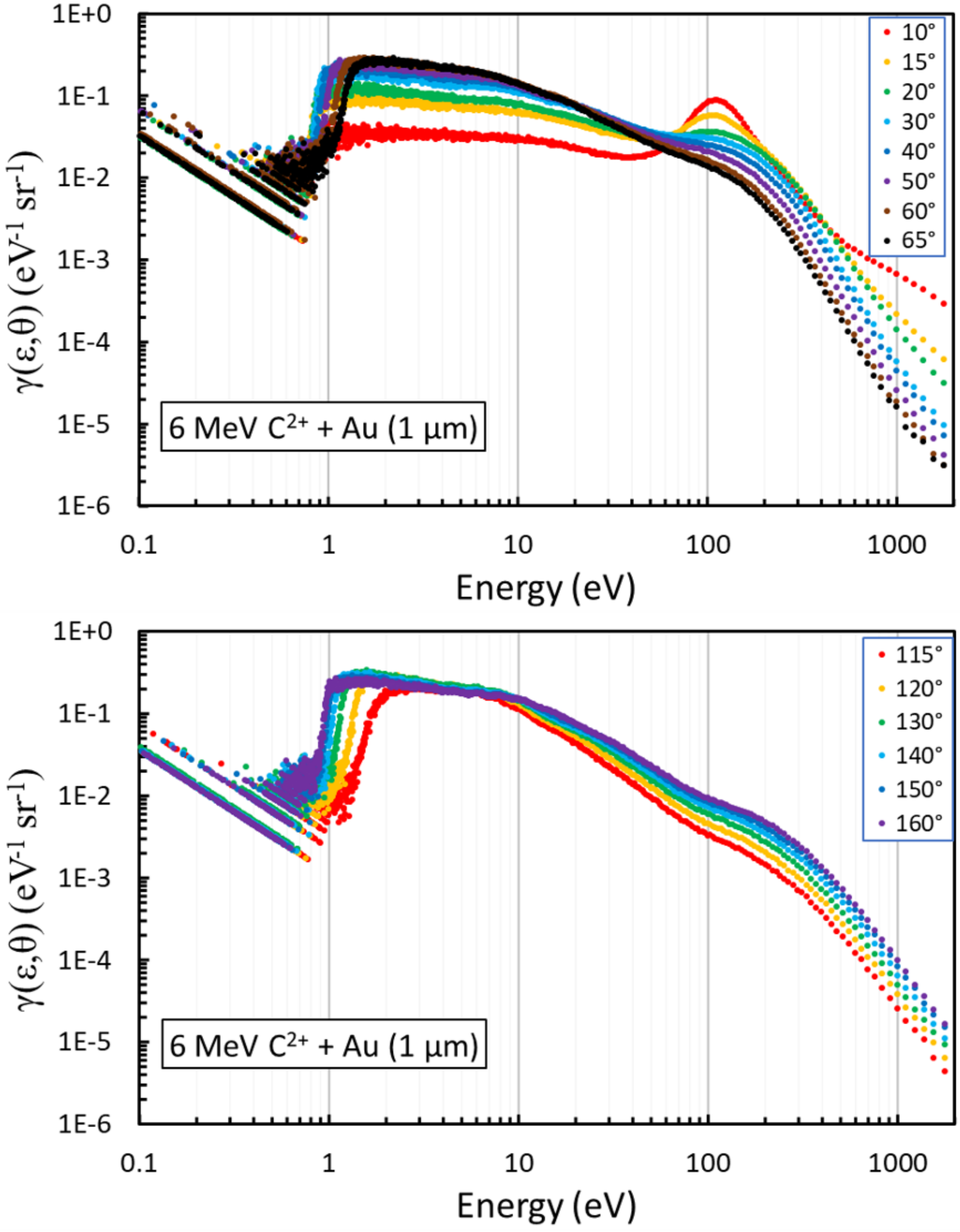

Figure 48: Doubly differential electron yields from 6 MeV carbon ion interactions with gold foil. Forward (top) and backward (bottom) scattered angles are normalized to total electron yields.

spectra. This could be due to the same detector flooding by scattered carbon projectiles seen in the greater than 1000 eV range. The 6 MeV carbon ion on gold foil spectra were normalized to Benka's total yield measurement of 22.7 electrons per proton for 6.4 MeV C^{6+} ions on gold [16]. The relative doubly differential electron yield integration method mentioned previously gave a relative total yield of 30.3, overestimating the total yields and generating a scaling factor of 0.75, which was applied to all relative yield spectra for 6 MeV carbon ion interaction spectra on gold foil in Fig.48.

An electron yield comparison of 2.4 MeV and 6 MeV carbon ion interactions on gold foil is shown in Fig.49. Although a lower total electron yield has been shown from previous measurements, a direct comparison after normalization shows a higher yield of low energy electrons for 2.4 MeV carbon ions when compared to 6 MeV carbon ions. This higher yield for low energy electrons could explain the dose distribution of carbon ions in the Bragg peak as it is believed low energy electrons are the primary source of damage to tissue, as discussed previously. It is unclear if this sharp drop off of high energy electron yield from 2.4 MeV is a physical phenomenon that explains the lower total yields measured by Benka and Itoh or an artifact of the experimental design of this investigation.

During normalization, as previously mentioned, total yield values were obtained from two different charge states of carbon, C^{+} and C^{6+}, neither of which are C^{2+}. Itoh describes the difference in charge state for total yields to be insignificant when comparing neutral to singly ionized carbon ion interactions with gold [25]. This provides confidence in using various charge state total yield measurements for normalization. To test this assumption, a charge state comparison was performed at ECU by reproducing a subset of the doubly differential electron yield measurements done by C^{2+} with the less favorable charge state C^{3+}. Both beams were tuned to an incident energy of 6 MeV. For a C^{2+} beam, a central terminal voltage of 2 MV was held, giving an entrance energy increase for C^{-} of 2 MeV, followed by an exit energy increase of 4 MeV. For a C^{3+} beam, a central terminal voltage of 1.5 MV was held, giving an entrance energy increase for C^{-} of 1.5 MeV, followed by an exit

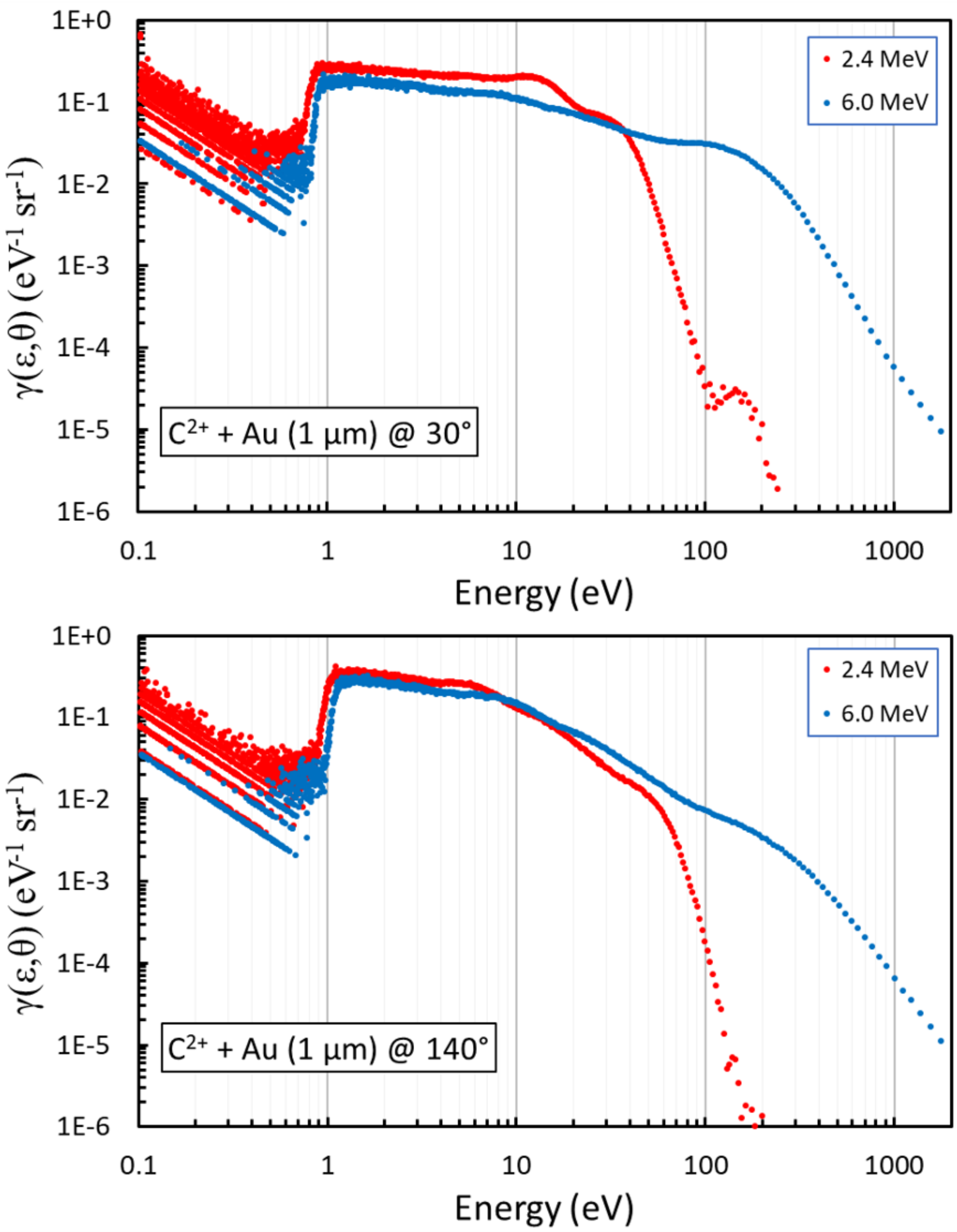

Figure 49: Doubly differential electron yield comparisons for 2.4 - 6 MeV carbon ion interactions with gold foil at 30° (top) and 140° (bottom).

energy increase of 4.5 MeV. A plot of the charge state comparison is shown in Fig.50. Both carbon ion charge states shown here were normalized to the C^{6+} total yields mentioned previously. This test showed an increase in electron yields for triply charged carbon ions for most energy ranges, contrary to Itoh's total yield findings.

3.3 Doubly Differential Electron Yields from Silicon GNPs

Doubly differential electron yields were measured for proton and carbon ion interactions with GNPs embedded in amorphous silicon lattice. Silicon wafers were ablated by a 30 fs pulsed laser as discussed in the previous chapter, resulting in 3 unique targets, provided by Tibbets et.al. [80]. A control target was prepared by laser ablating a silicon wafer in DI water. Another sample was prepared by ablating a similar silicon wafer in a 1.0 mM $KAuCl_4$ and 10.0 mM KOH, resulting in a target surface of 1.5% GNP as measured by an energy-dispersive x-ray spectrograph (EDX). A third target was manufactured by ablating a silicon wafer in 1.0 mM $KAuCl_4$ and 2.5 mM KOH, resulting in a target surface of 9.5% GNP as measured by EDX. Due to the 300 μm thickness of the silicon wafers, no forward scattered projectiles could be measured by the Rutherford detector for relative doubly differential electron yield measurements. To compensate for this, scattered projectiles from gold foil were used after scaling based on beam current in the experimental beam line. This technique served to offer comparisons between silicon GNP runs and create a baseline spectrum for later yield-based comparisons to normalized doubly differential electron yields.

3.3.1 Protons on Silicon GNPs

Beam optimization was performed using gold foil, including obtaining 0° peaks, measuring yields at various backward scattered angles, and establishing a relationship between experimental beamline current and scattered projectile counts for timed runs before each silicon target spectra attempt. After beam stabilization and data analysis calibration was done, the UHV chamber was opened in order to switch gold foil and silicon wafer targets.

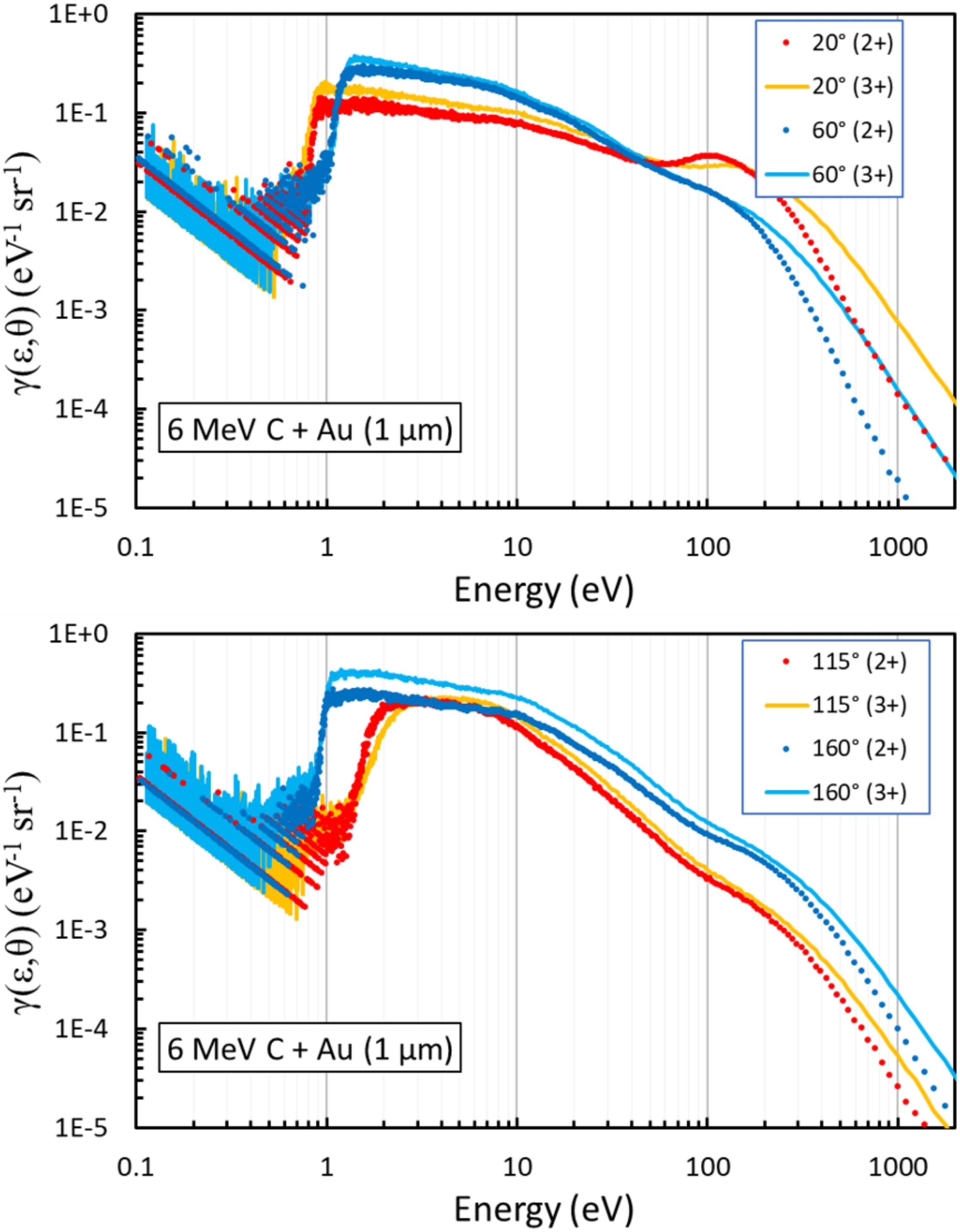

Figure 50: Shown is a comparison between doubly and triply ionized 6 MeV carbon ion interactions with gold foil. Forward (top) and backward (bottom) scattered angles both show a significant increase in high energy electron production for triply ionize carbon ion interactions.

Doubly differential electron yield measurements were taken for back scattered electron emission from proton interactions with the silicon control (Fig.51), 1.5% GNP (Fig.52), and 9.5% GNP (Fig.53) targets. A comparative plot (Fig.54) of electron yields at 140° was made to show a sharp increase in low energy electron emission in the presence of GNPs, with a small difference in electron yields from a 1.5% GNP surface to a 9.5% GNP surface. The scale of these plots is arbitrary as the method for calculating relative yields involved a process of entering scattered projectile numbers into the data analysis which were generated by comparing beam current during gold foil experiments.

Due to the lack of available total electron yield measurements available for proton interactions with silicon GNPs, normalization was not possible. Although, a yield-based comparison of the 9.5% silicon GNP spectra was made with normalized gold foil spectra. Doubly differential electron yields from 2 MeV proton interactions with gold foil and silicon GNPs are shown in Fig.55. The 9.5% GNP spectrum in this plot was scaled to have equivalent yield at 100 eV. The assumption being made here is that target type has little influence on the production of rare, high-energy electrons. Given the assumption of similar high energy electron production for similar incident projectile energy, a significantly higher level of low-energy electron yields can be seen in the 9.5% silicon GNP target when compared to the gold foil target.

3.3.2 Carbon Ions on Silicon GNPs

Relative doubly differential electron yields were measured for carbon ion interactions with silicon GNPs. The 9.5% GNP target was irradiated with carbon ions of various charge states and energies. A plot of relative doubly differential electron yields for 6 MeV C^{2+}, 8 MeV C^{3+}, and 10 MeV C^{4+} interactions with 9.5% GNP on silicon substrate at 160° is shown in Fig.56. A general increase in electron yields for lower energy incident projectiles was observed during this comparison study as expected. How the charge state of the carbon ions influence the electron yield spectra is unknown as there was a disagreement between

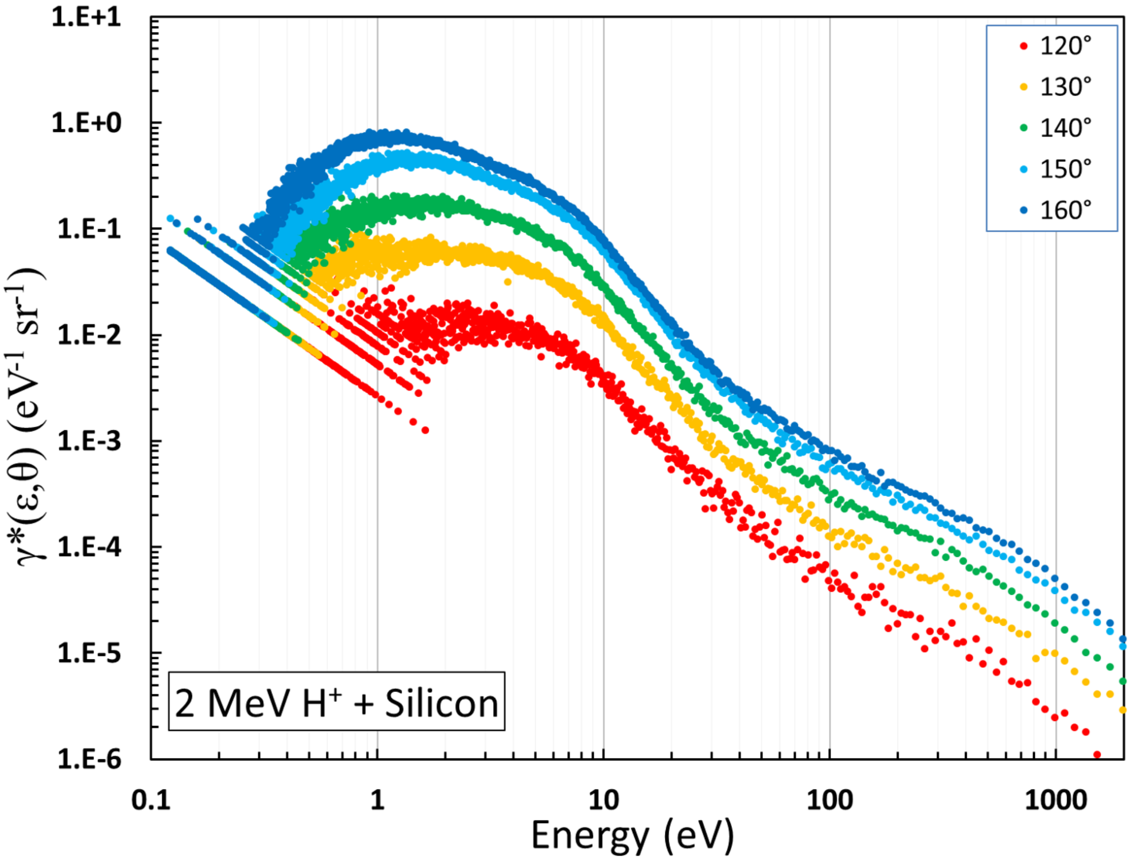

Figure 51: Back-scattered relative doubly differential electron yields from 2 MeV proton interactions with laser ablated silicon wafer target.

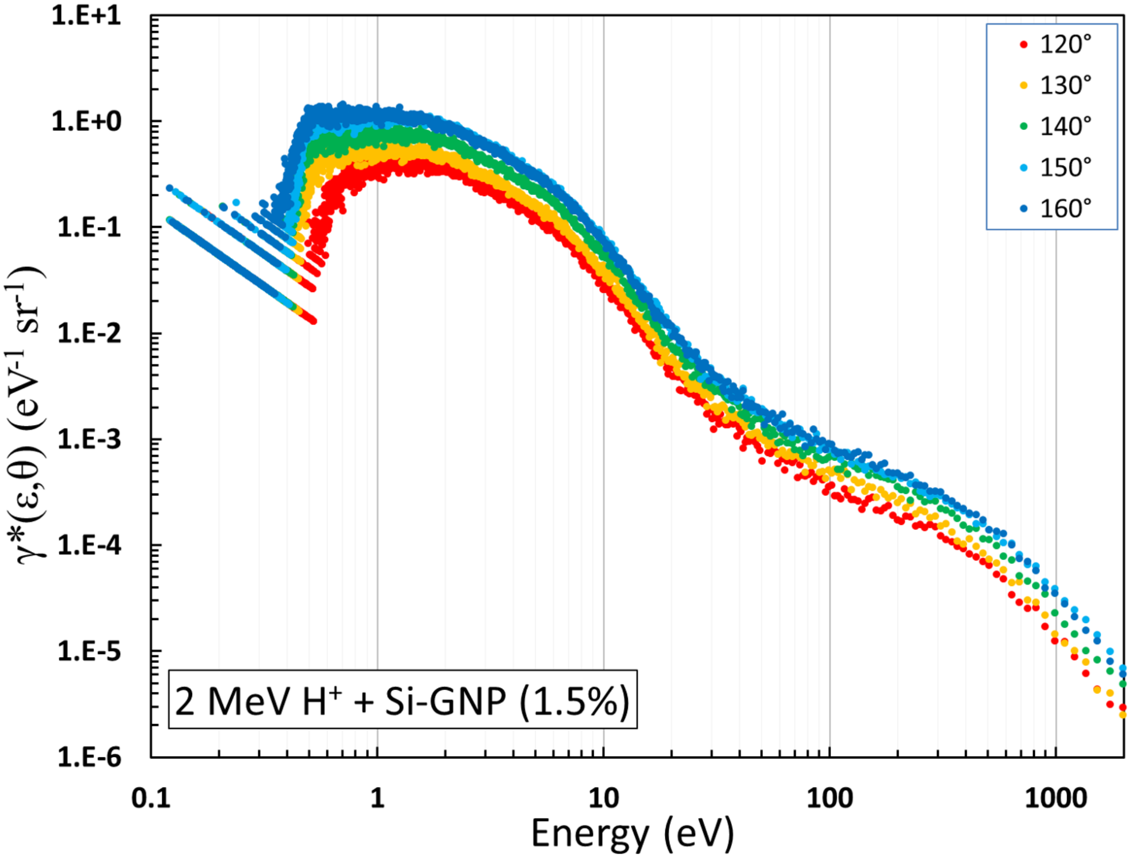

Figure 52: Back-scattered relative doubly differential electron yields from 2 MeV proton interactions with laser ablated silicon wafer target with 1.5% GNP surface.

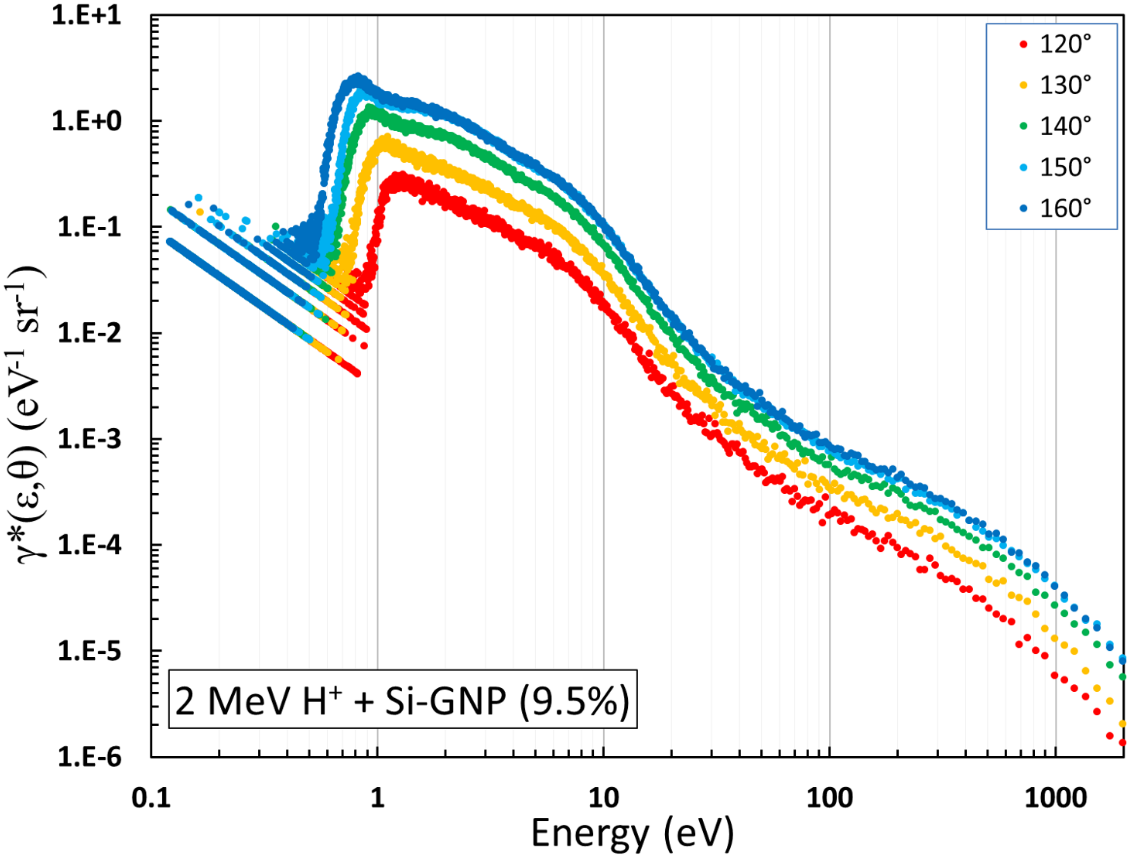

Figure 53: Back-scattered relative doubly differential electron yields from 2 MeV proton interactions with laser ablated silicon wafer target with 9.5% GNP surface.

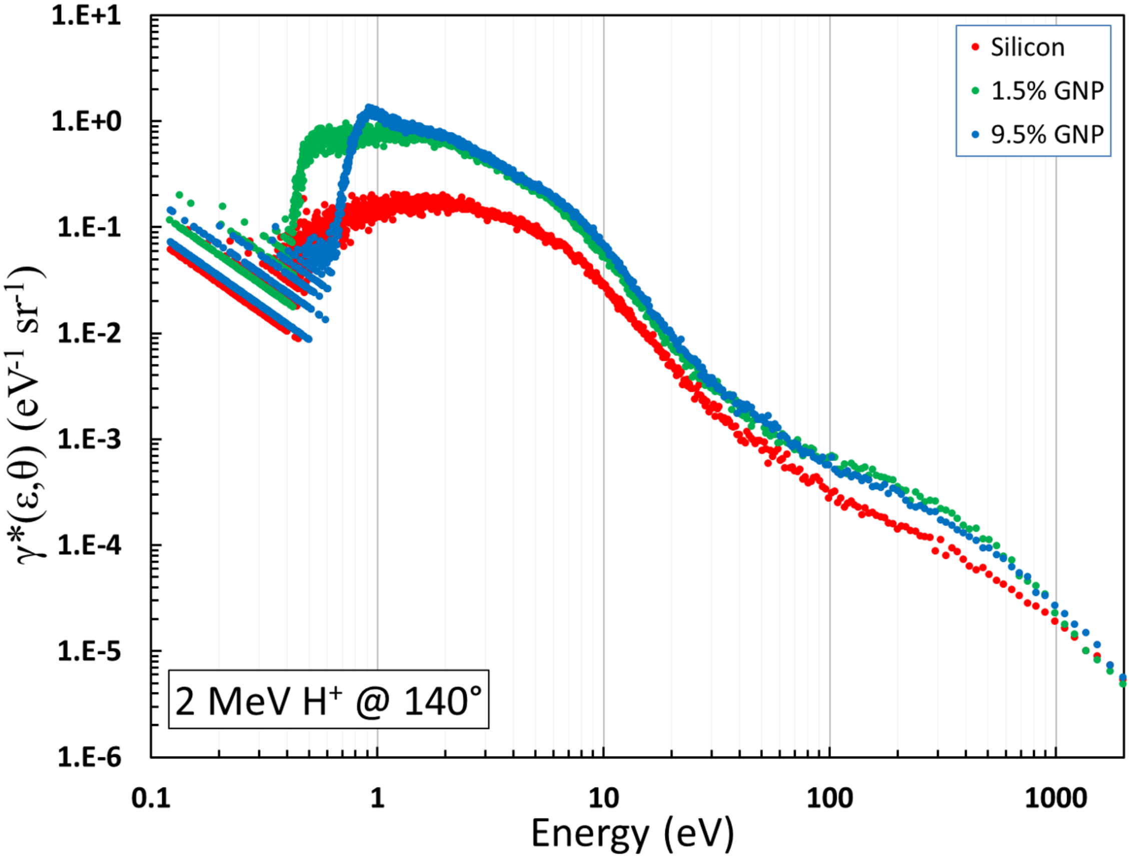

Figure 54: Relative doubly differential electron yield comparisons for 2 MeV proton interactions with silicon, 1.5% Si-GNP, and 9.5% GNP targets at 140°.

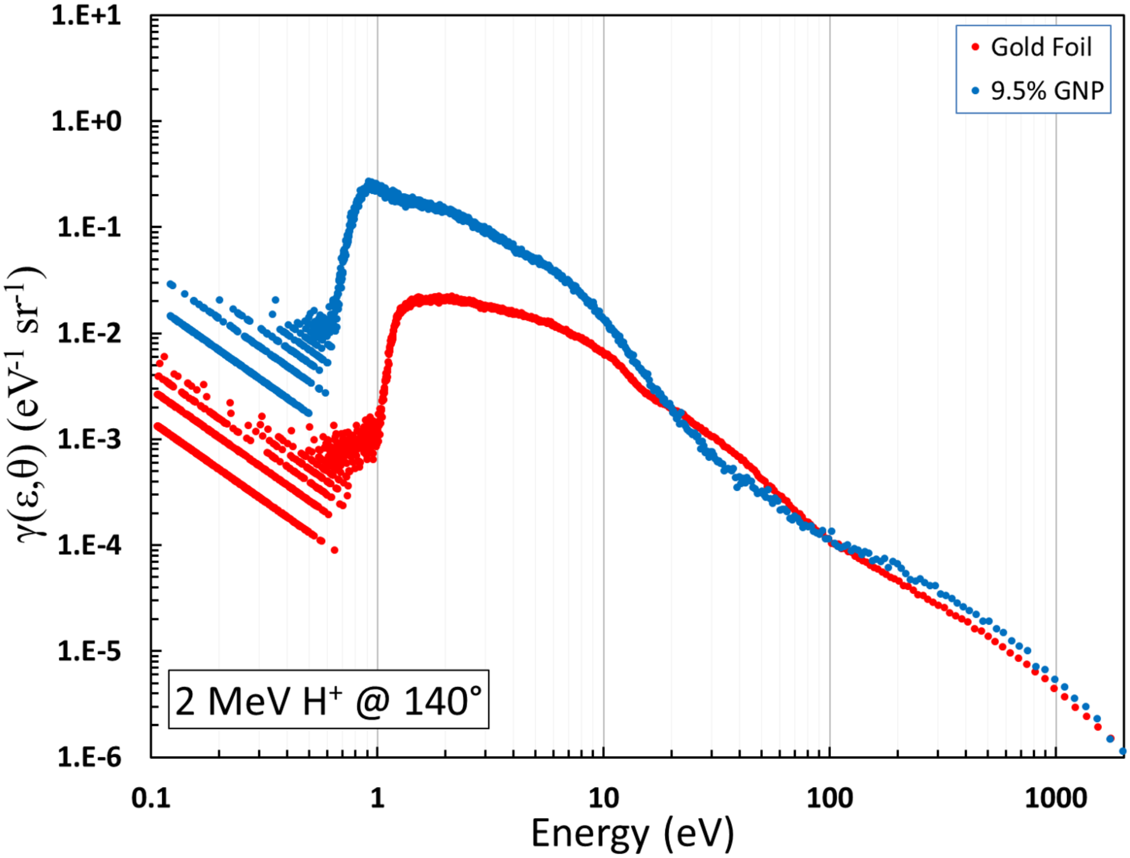

Figure 55: Electron yield spectra from 2 MeV proton interaction with 9.5% GNP on silicon yield-scaled at 100 eV to normalized electron yield spectra of 2 MeV proton interaction with gold foil.

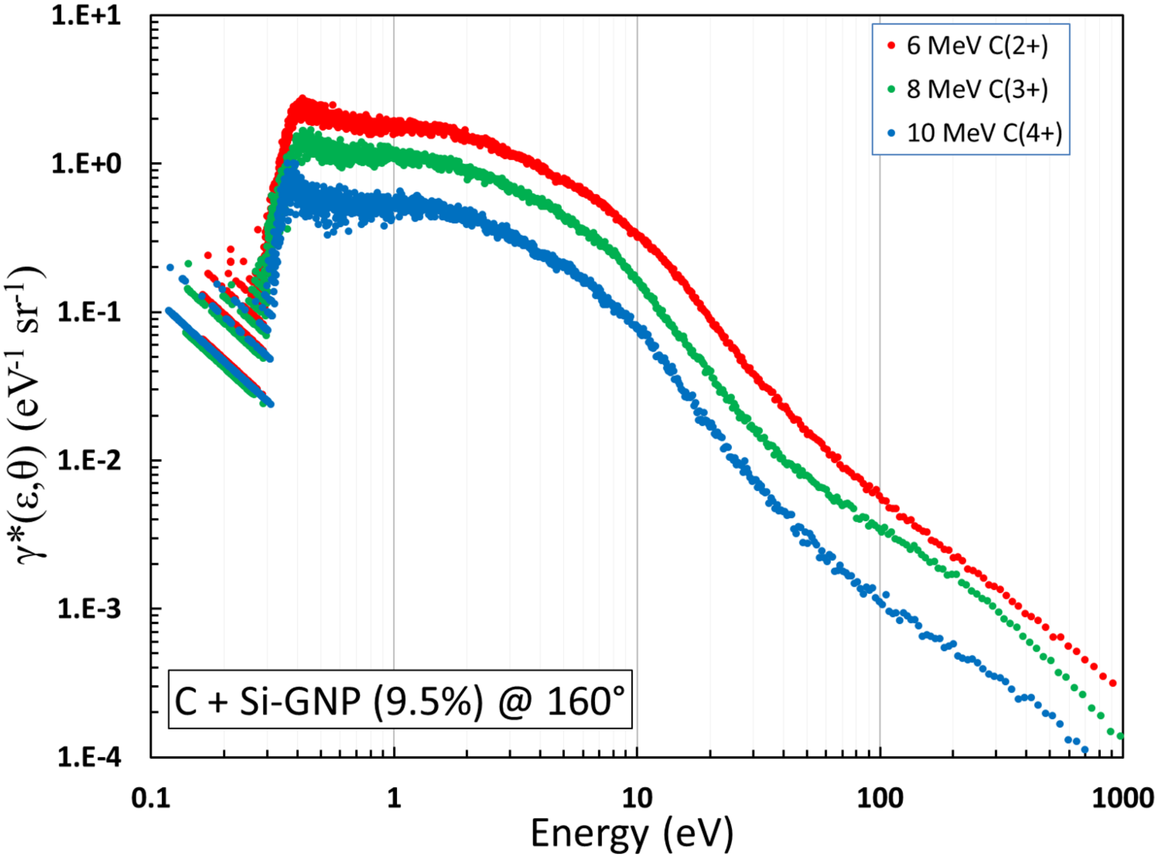

Figure 56: Relative doubly differential electron yield comparisons for 6, 8, and 10 MeV C^{2+} interactions with 9.5% GNP on silicon target at 160°.

the charge state tests performed on gold foil, shown previously, and the observations made by Itoh et.al [25].

A direct comparison of 6 MeV C^{2+} induced electron yields between the 9.5% silicon GNP target and gold foil is shown in Fig.57. The relative doubly differential electron yields from 6 MeV C^{2+} interaction with the 9.5% GNP target was scaled using the previously mentioned yield-based technique by equating the 100 eV yields for both spectra. Again, the assumption made here is the high energy projectile production depends more heavily on the projectile energy, rather than the target type. Given this assumption, a dramatic difference in low energy electron yields can be observed between the targets as the 9.5% GNP target shows a higher low energy electron yield by over an order of magnitude.

3.4 Doubly Differential Electron Yields from GNP Film

GNP film on TEM grid substrate targets, as described in the previous chapter, were used to measure relative doubly differential electron yields from fast proton and carbon ion projectiles. Visual inspection of the GNP film targets were performed using an optical microscope to ensure target quality. A reflective surface was observed in the open hole regions of the grid, providing evidence of GNP film. For many target samples, the manufacturing, shipping, and handling of these 4 - 6 nm film targets resulted in significant film loss. Only targets with few (10 or so) grid holes of GNP film missing were used for data collection. Some new targets analyzed showed roughly half (out of hundreds) of grid holes lacking a reflective surface, meaning that roughly half of the GNP film was lost in shipping and handling. Many tests were done to find an optimal procedure for GNP film irradiation including beam exposure time, ion sputter gun cleaning, and temperature tests. Exposure of the GNP film to unpulsed beam for any amount of time resulted in a near total loss of GNP film. Similarly, exposure to Argon gas during ion sputter cleaning completely destroyed the GNP target. Visual inspections from these tests showed less than 10% grid holes with a reflective surface, meaning a near complete target loss. To compensate, unpulsed beam optics optimization

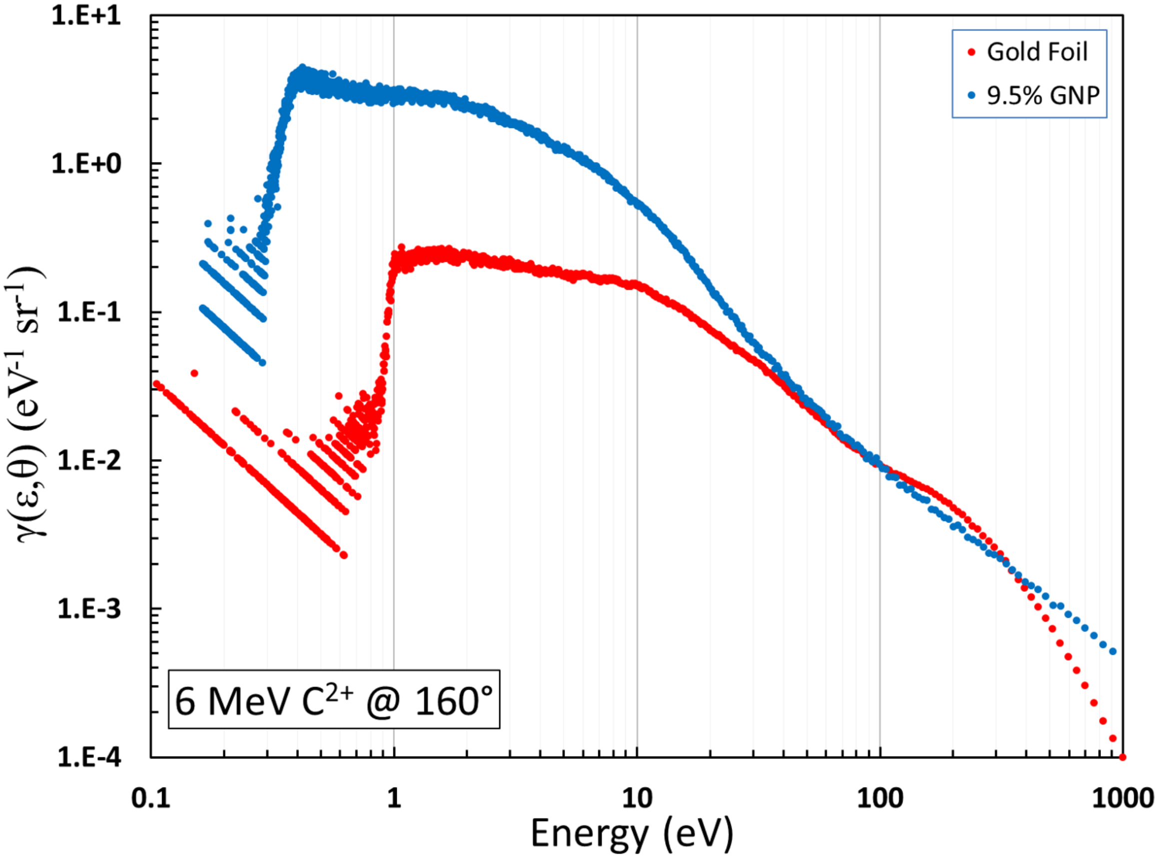

Figure 57: Electron yield spectra from 6 MeV C^{2+} interaction with 9.5% GNP on silicon yield-scaled at 100 eV to normalized electron yield spectra of 6 MeV C^{2+} interaction with gold foil.

was performed with gold foil targets prior to GNP installation, meaning the UHV chamber was opened and the target assembly was reconfigured for GNP film mid-run for each trial attempt, similar to the procedure used for silicon GNP irradiation. Also, neon gas was used for sputter cleaning as this lighter ion proved to cause less damage overall to the GNP film targets. Sputtered neon gas has been shown to be less effective at cleaning the surface of foils, meaning that longer exposure times are required to achieve the same convergence of “clean” spectra. This disclaimer serves to educate the reader on the assumptions made here for beam stability over a long period of time (hours). Also, extra consideration for scattered projectiles counted by the Rutherford detector for GNP film targets should be made as it is unclear what effects the TEM grid substrate has on the forward scattered projectiles.

3.4.1 Protons on GNP Film

Relative doubly differential electron yield measurements were made for fast proton interactions with GNP film on TEM grid targets. Cleaning the GNP film target proved to be challenging as only neon gas, a less effective sputter cleaning ion, was used instead of argon to preserve target integrity. Cleaning tests were performed, showing target resiliency (less than 10% target loss) over 5 minute exposure to neon sputtering, but suffering significant damage (greater than 50% target loss) after 20 minute exposure to neon sputtering. Any amount of pulsed proton beam exposure without cleaning showed little to no effect on target integrity. Both ambient temperature (280 K) and low temperature (40 K) electron yield spectra were measured in preparation of ASW buildup measurements (discussed in a later section). A series of relative doubly differential electron yield spectra from subsequent cleanings during 2 MeV proton irradiation at different temperatures is shown in Fig.58. The red spectrum was taken from a new, “dirty” GNP film target and the orange spectrum was taken after 5 minute exposure to neon sputtering. The dark blue spectrum was taken several hours later after the target temperature was lowered to 40 K, and the light blue spectrum was taken immediately after the dark blue spectrum after another 5 minute exposure to neon

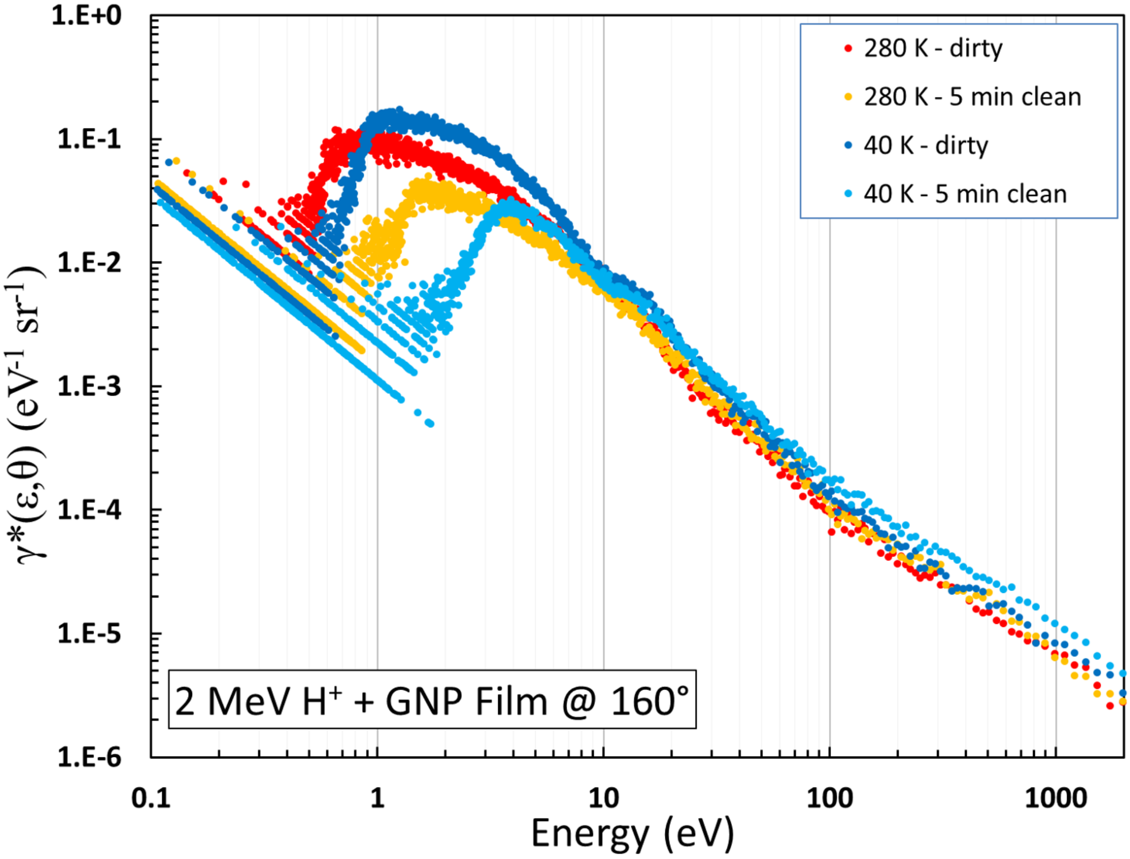

Figure 58: Sequential spectra taken from a single GNP film target starting with a new "dirty" GNP film (red), then a spectrum after a 5 minute neon sputtering exposure (orange), then again a "dirty" spectrum after 4 hours of target chilling to 40 K (dark blue), then finally a spectrum after another 5 minute neon sputtering exposure (light blue).

sputtering. No gases were introduced to the UHV chamber during the chilling process, meaning that the increase in low energy electron yield from the orange to dark blue spectrum was completely due to ambient particulates in the UHV chamber at a pressure of roughly 1×10^{-8} torr over a time span of 4 hours. A clear change in the electron yield shape was noted for 40 K conditions in both the "dirty" and "clean" spectra. A clear drop in low energy electron yields was observed from both cleanings, and the target was inspected after this trial to reveal less than 10% target loss.

Relative doubly differential electron yield spectra from 1, 2, and 3 MeV proton irradiation were measured and are shown in Fig.59. Unique GNP film targets were used for each of these spectra, all visually inspected to be less than 10% damaged both before and after irradiation. All spectra shown in Fig.59 were measured after 5 minute exposure to neon sputter cleaning. An increased electron yield is shown for lower projectile energies, as expected, with 2 MeV and 3 MeV proton spectra showing high energy electron yield convergence. A yield-based scaling of the 2 MeV proton irradiation of GNP film spectrum was performed to match normalized 2 MeV proton irradiation of gold foil spectrum and is shown in Fig.60. Unlike the silicon GNP target comparison to normalized gold foil spectra, only a slightly higher low energy electron yield was seen in the GNP film target comparison under the same 2 MeV proton irradiation conditions. This could be due to the gold TEM grid serving as the dominant electron producer, leading to an over population of high energy electrons, swamping the low energy electron spectrum, as previously discussed.

3.4.2 Carbon Ions on GNP Film

Relative doubly differential electron yield measurements were made for fast carbon ion interactions with GNP film on TEM grid targets. Sputter cleaning with neon yielded similar results to carbon interaction spectra as proton interaction spectra. A decrease in low energy electron yields and an increase in high energy electron yields can was observed and is shown in Fig.61. An energy comparison is shown in Fig.62. Here 2.4, 6, and 8 MeV carbon

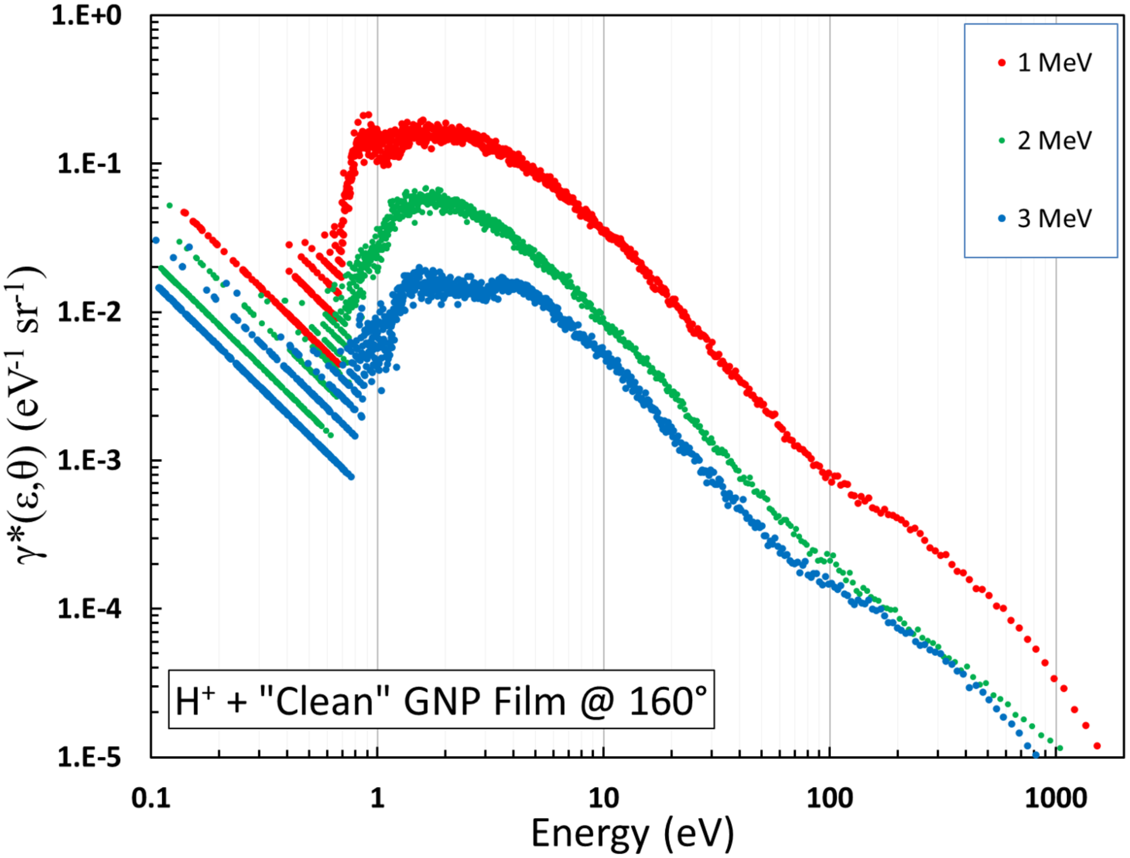

Figure 59: Relative doubly differential electron yield comparisons for 1, 2, and 3 MeV proton interactions with GNP film target at 160°.

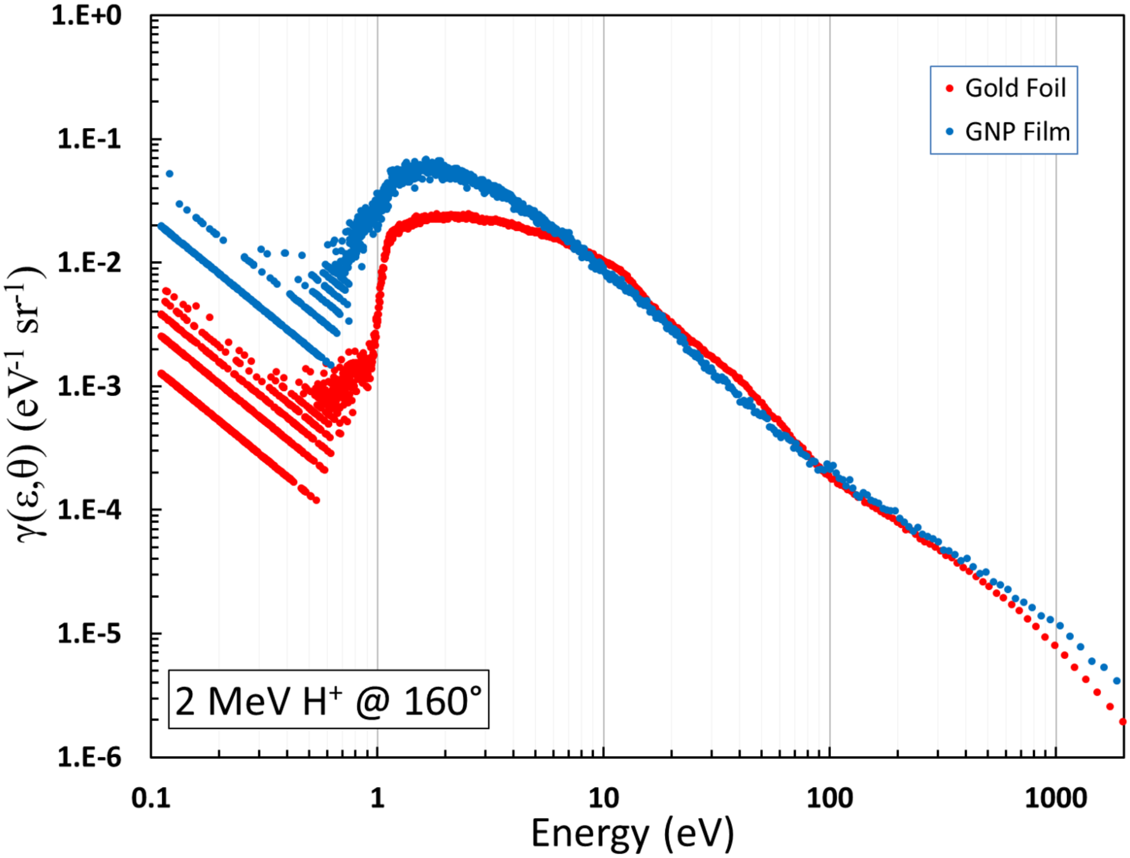

Figure 60: Electron yield spectra from 2 MeV proton interaction with GNP Film yield-scaled at 100 eV to normalized electron yield spectra of 2 MeV proton interaction with gold foil.

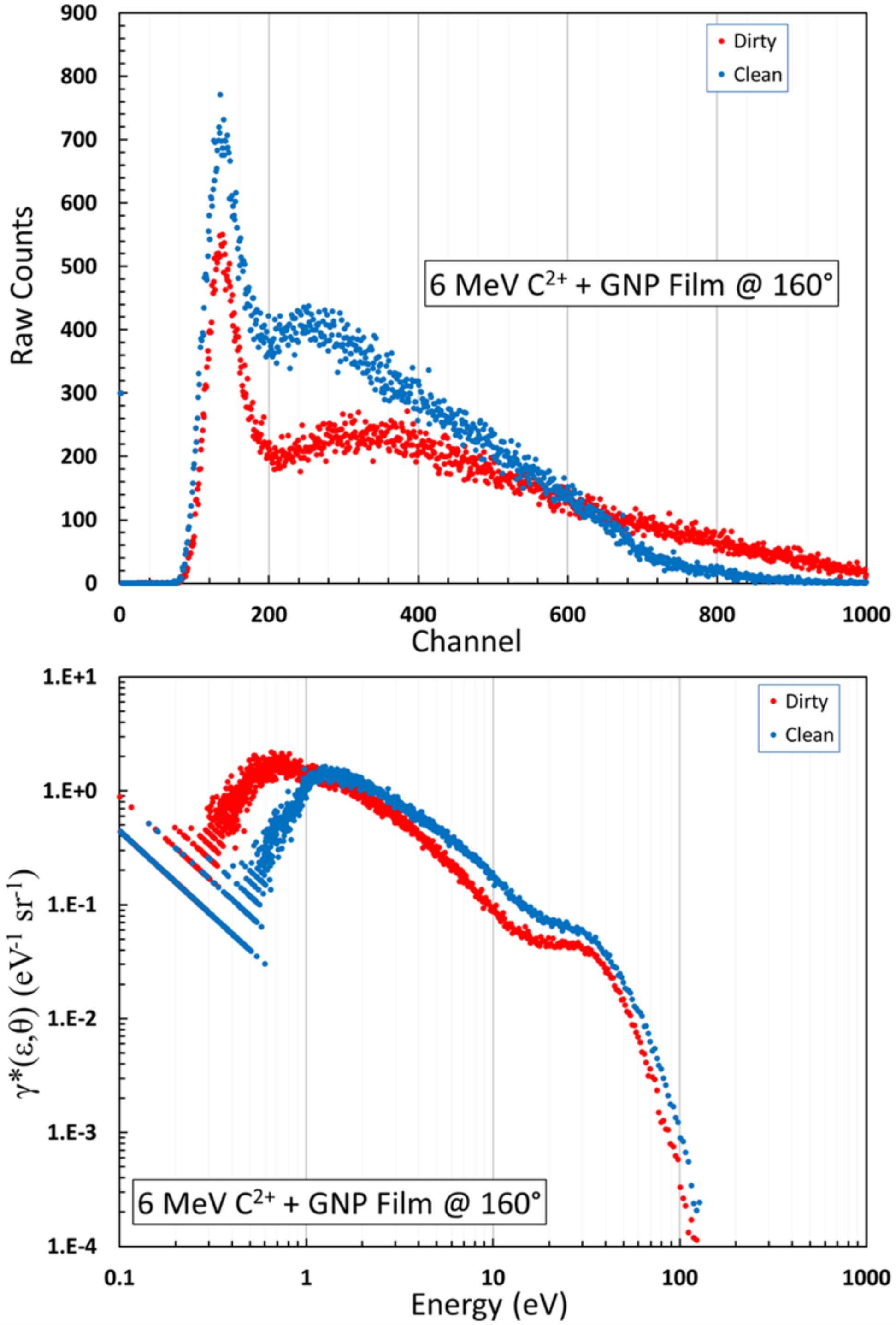

Figure 61: Comparison of “dirty” and “clean” spectra after 5 minutes of neon sputter cleaning. A decrease in low energy electron yields and an increase in high energy electron yields was noted. This was the same trend observed in both gold foil and Si-GNP cleaning tests.

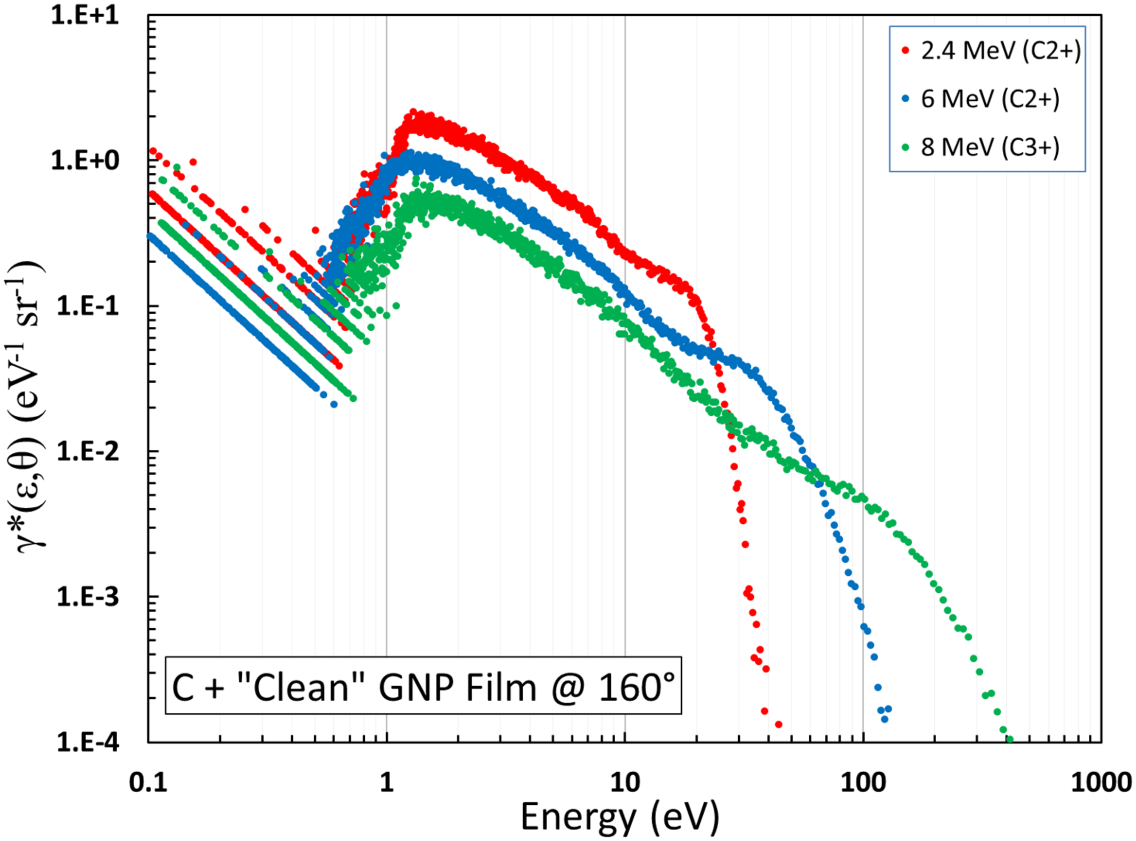

Figure 62: Relative doubly differential electron yield comparisons for 2.4, 6, and 8 MeV carbon ion interactions with GNP film target at 160°.

ion induced relative doubly differential electron yields all exhibit a steep drop off in high energy electron yields, all at different energies. This same behavior was observed for carbon ion interactions with gold foil. In the low energy range (1 - 11 eV) of this plot, a general decrease in low energy electron yields were observed for increasing projectile energies, which is to be expected. Due to the steep drop off in high energy electron yields for these low energy/AMU projectiles ion GNP film, the method of yield-based scaling at 100 eV, making the assumptions about high energy electron yields stated earlier, was not practical. Instead, a yield-based scaling of relative yields from 2.4 MeV carbon ions on GNP film to normalized yields from 2.4 MeV carbon ion on gold foil at 20 eV was plotted. This comparison to normalized yields, scaled at 20 eV is shown here, in Fig.63. Only a small increase in carbon ion induced low energy electron yields was observed, similar to the subtle increase in proton induced low energy electron yields. It is unclear if this difference in an artifact of the structure of the GNP film, or a result of surface changes due to sputter cleaning or the inability to sufficiently sputter clean without compromising GNP film target integrity.

3.5 Doubly Differential Electron Yields from Amorphous Solid Water

Optimal conditions for amorphous solid water (ASW) formation were investigated. Using the process described in the previous chapter, ASW was deposited in monolayers, or Langmuir (L), onto various targets acting as substrates during this investigation. A thickness of 100 L was previously determined to be optimal for electron emission measurements from "pure" ASW targets as this was believed to no longer contain electrons formed on the surface of the substrate due to ASW attenuation [3]. McLawhorn et.al. also postulated that ASW buildup beyond 100 L displayed evidence of target charging effects. A test of these forgone conclusions was performed by measuring electron yield spectra over a wide range of ASW thickness on a gold foil substrate, shown in Fig.64. Clean gold foil is shown in black, ASW buildup to 100 L is shown in red, the 100 L spectra that was used as a standard for this

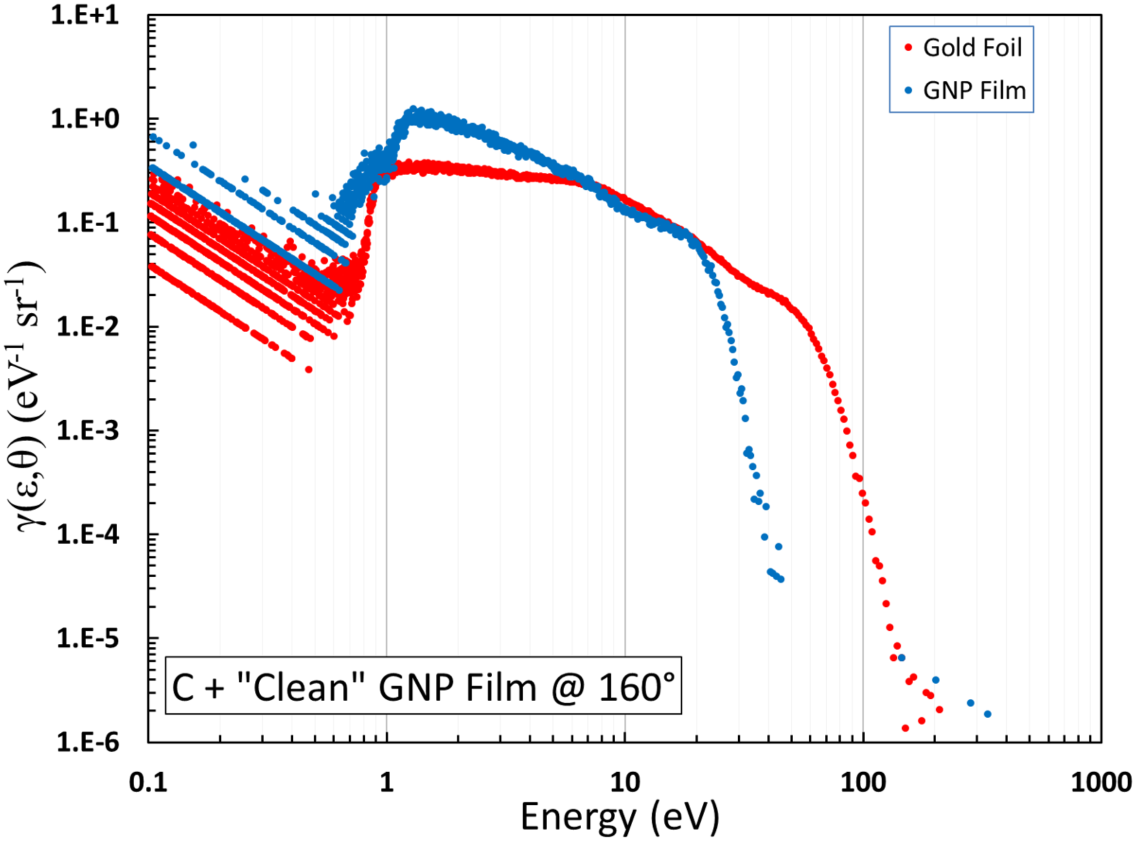

Figure 63: Electron yield spectra from 2.4 MeV C^{2+} interaction with GNP Film yield-scaled at 20 eV to normalized electron yield spectra of 2.4 MeV C^{2+} interaction with gold foil.

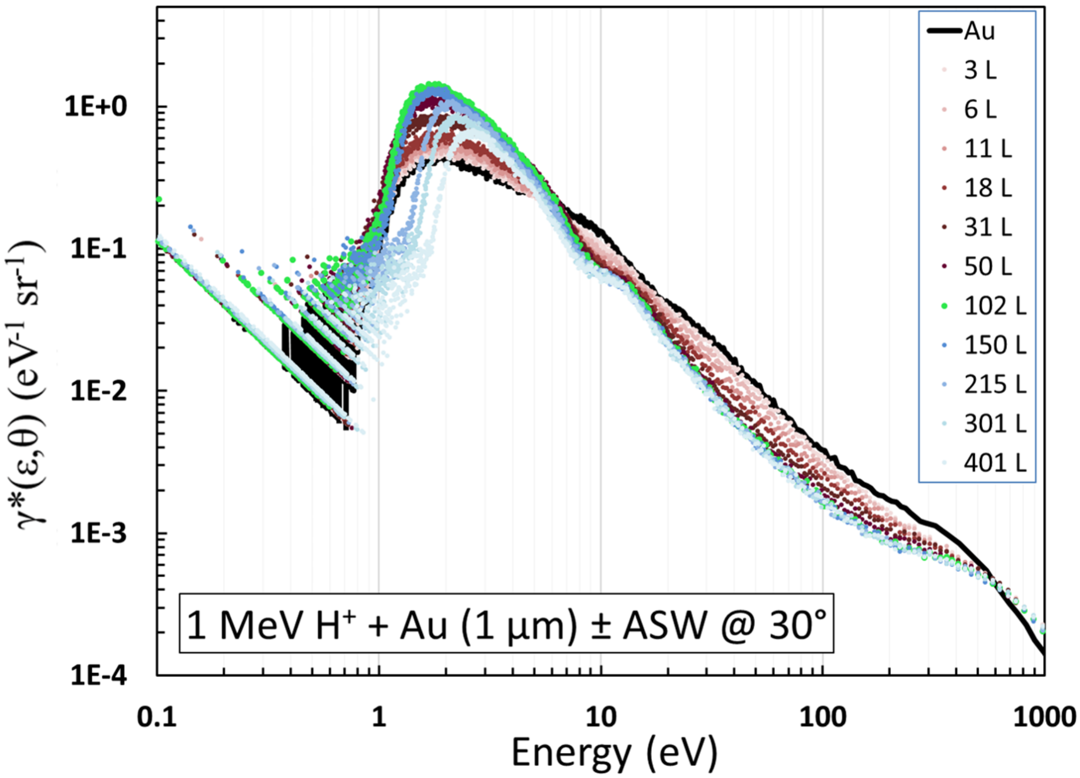

Figure 64: Electron yield spectra from 1 MeV proton impact on ASW for various ASW thicknesses. The initially clean foil substrate is shown in black and the optimal ASW thickness of 100 L is shown in green.

work is shown in green, and ASW buildup past 100 L is shown in blue. This test confirmed the trends seen in previous work and served as a justification for the selection of 100 L as the optimal thickness in electron yield from ASW measurements.

3.5.1 Protons on ASW

Relative doubly differential electron yields from proton interactions with 100 L ASW were measured for proton projectiles of incident energy 1, 2, and 4 MeV. These relative yields were normalized using the calculated scaling factor found from the normalization of proton interactions with gold foil to total yields, as discussed previously. This scaling was applied to compensate for the overestimation in yields of the TOF detector acceptance solid angle and any unknown electronics or detector efficiencies inherent in the experimental design. Plots of forward scattered and back scattered doubly differential electron yield measurements made for 1, 2, and 4 MeV proton interactions with 100 L ASW are shown in Fig.65, Fig.66, and Fig.67 respectively. The same characteristic scattered projectile peaks in the high energy range of the spectra, decreasing with increasing angle, seen in the golf foil measurements are present in the ASW measurements. A characteristic autoionization peak (8-11 eV) in the low energy electron yields of ASW was observed that was not present in the gold foil measurements. An energy comparison for 1, 2, and 4 MeV proton interactions with ASW for a single forward and a single backward scattered angle is shown in Fig.68. As seen in previous energy comparisons, the electron yields increase for lower incident projectile energies in both the forward and backward scattering directions.

A PARTRAC simulation of 2 MeV proton interactions with 20 nm films of water on the front and back side of a 1 μm thick water substrate, scaled to the density of copper, was performed by M. Dingfelder [85, 86]. This simulation recorded doubly differential electron yields from 220,000 incident proton events over the course of 2 weeks of computational time. The experimental results from 2 MeV proton interactions with 100 L ASW shown here were measured using a 1 μm thick gold foil substrate. The justification of this comparison

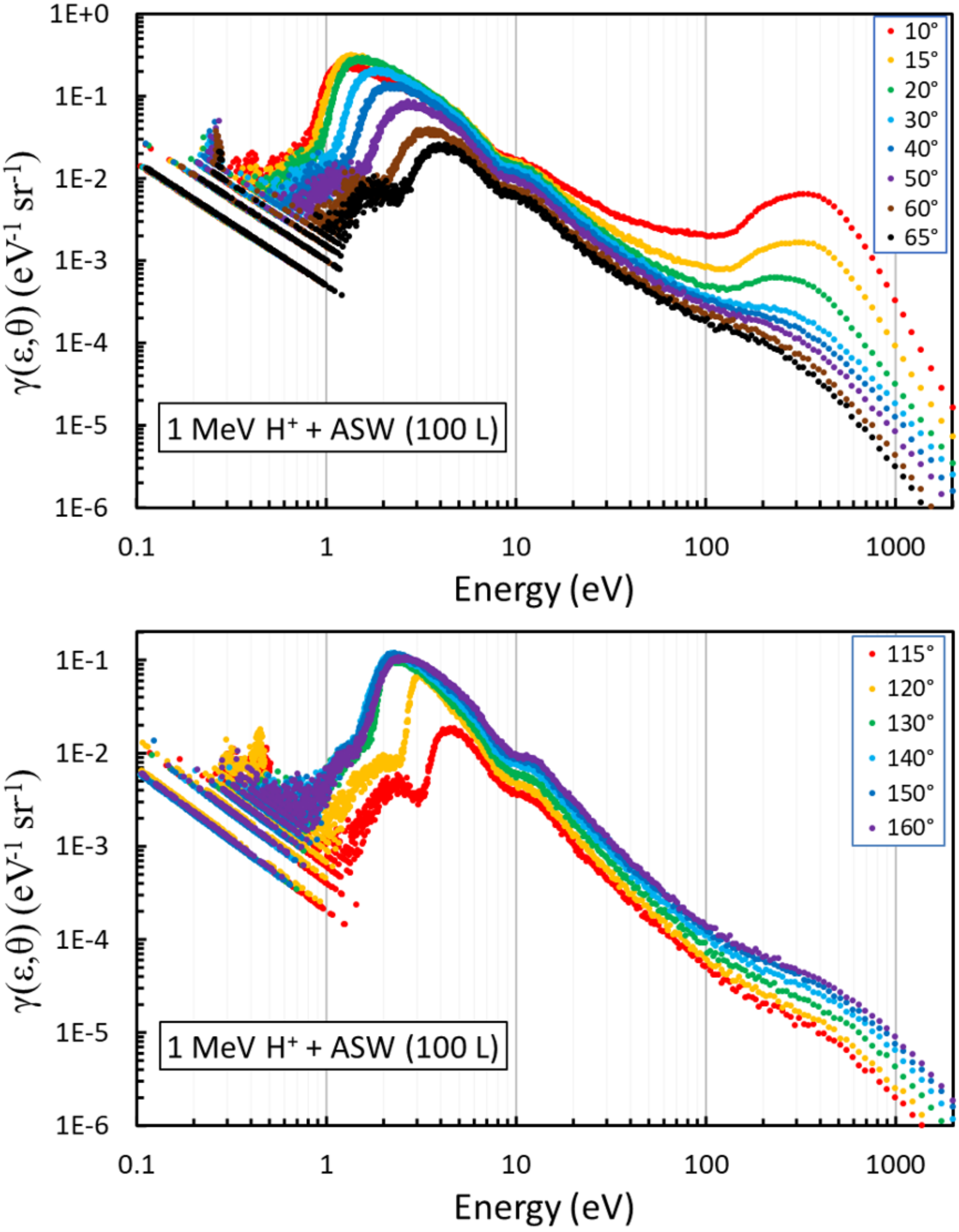

Figure 65: Doubly differential electron yields from 1 Mev proton interactions with 100 L amorphous solid water. Forward (top) and backward (bottom) scattered angles are normalized to total electron yields from gold foil.

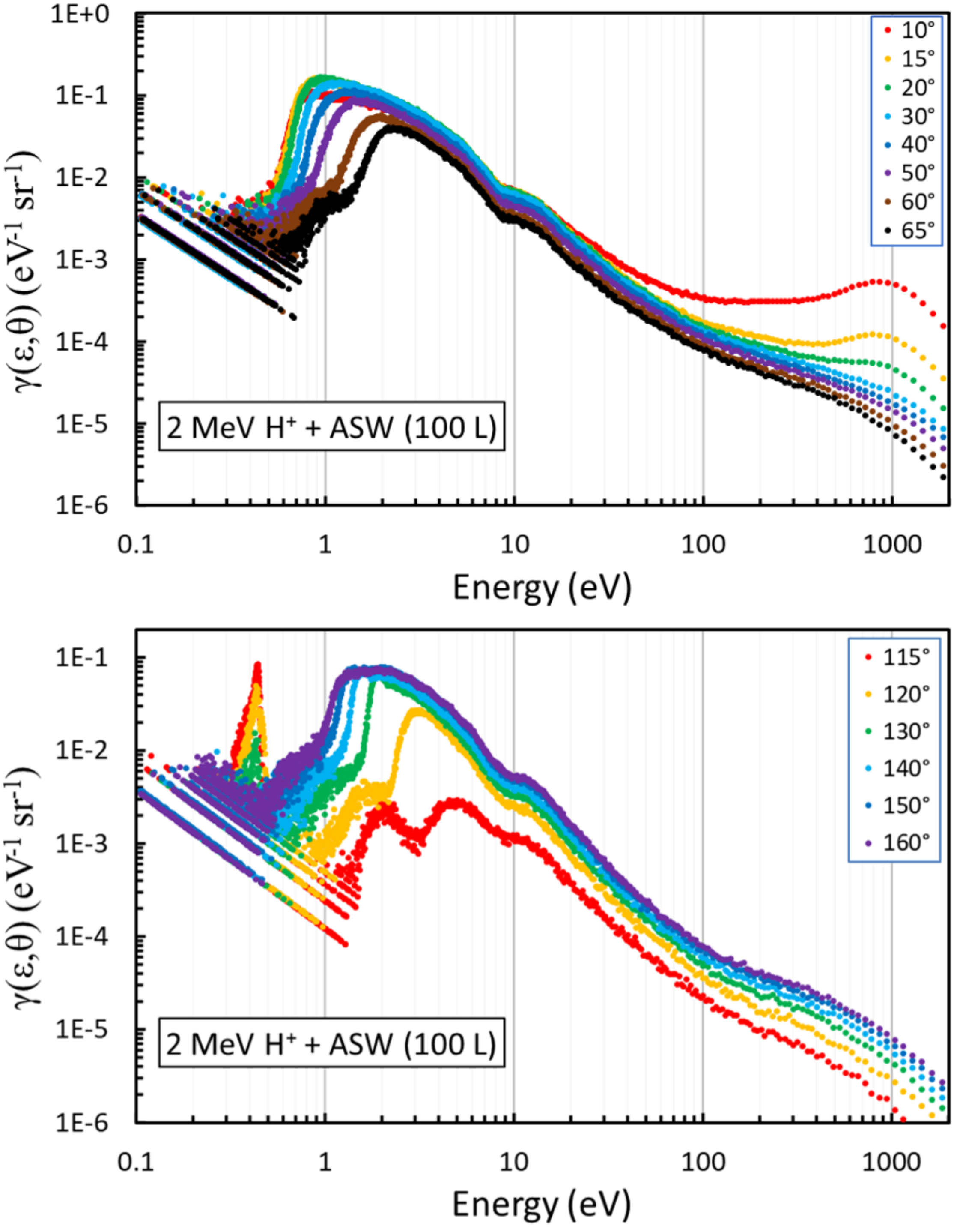

Figure 66: Doubly differential electron yields from 2 Mev proton interactions with 100 L amorphous solid water. Forward (top) and backward (bottom) scattered angles are normalized to total electron yields from gold foil.

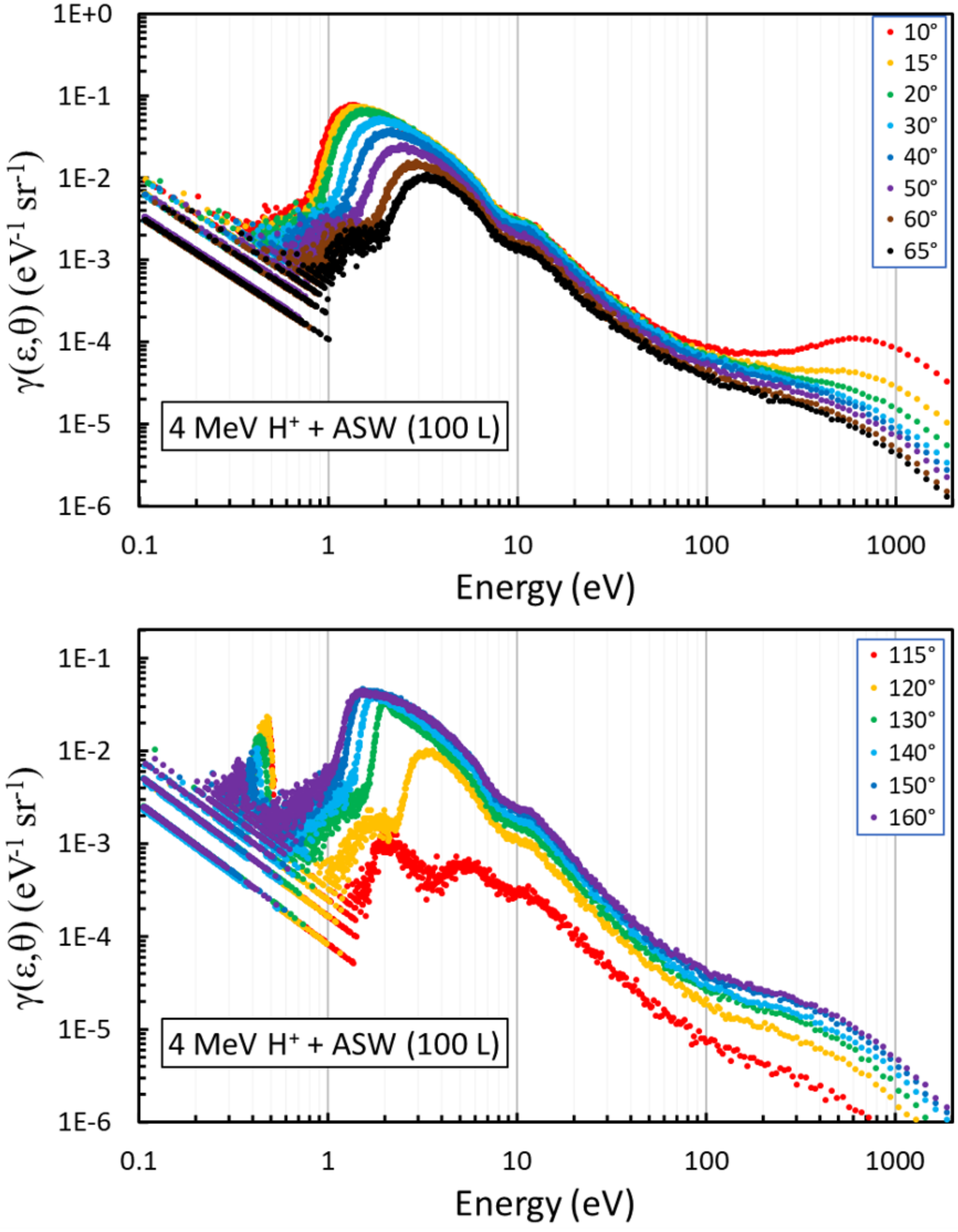

Figure 67: Doubly differential electron yields from 4 Mev proton interactions with 100 L amorphous solid water. Forward (top) and backward (bottom) scattered angles are normalized to total electron yields from gold foil.

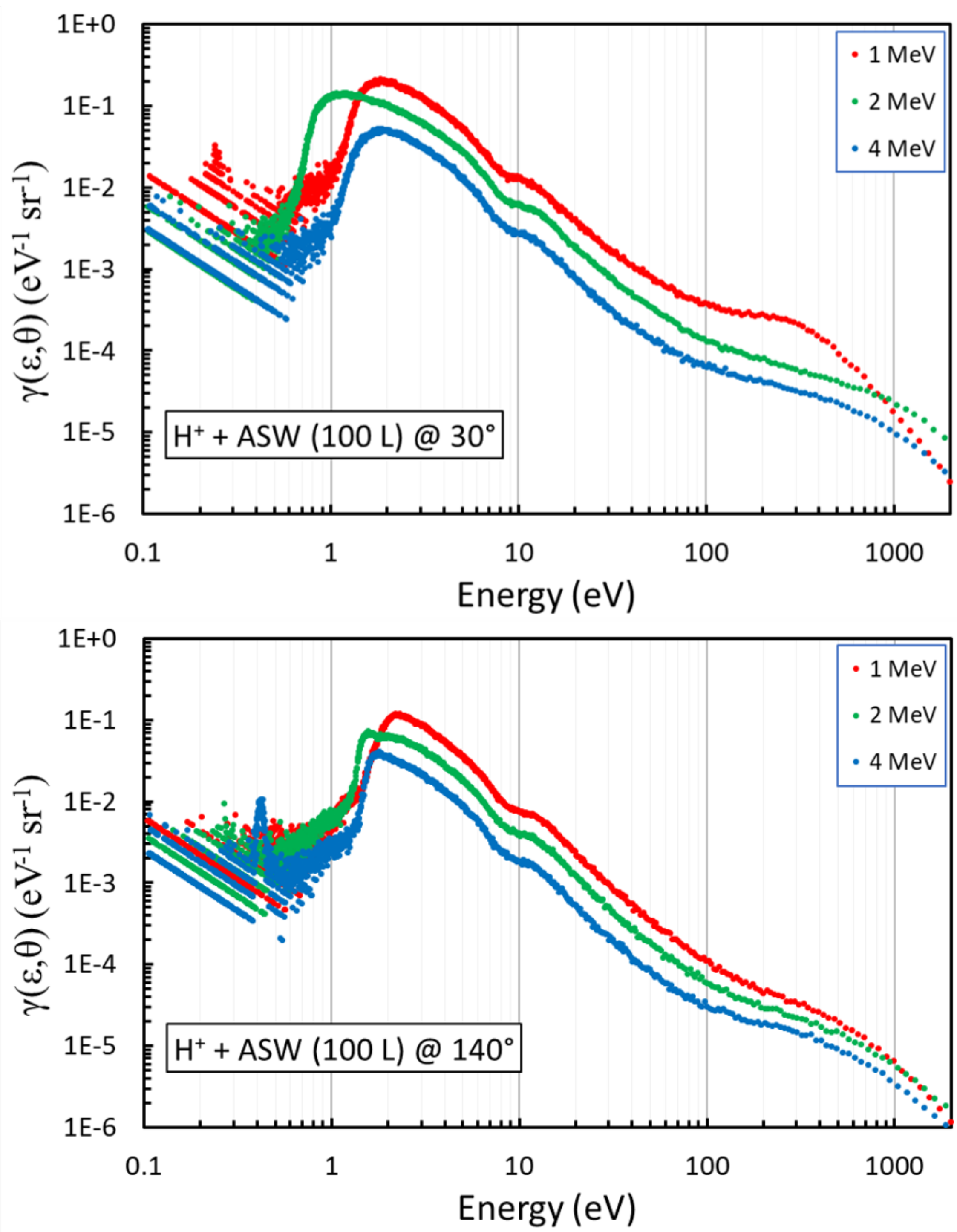

Figure 68: Doubly differential electron yield comparisons for 1 - 4 Mev proton interactions with ASW at 30° (top) and 140° (bottom).

stems from the assumption that 100 L of ASW completely attenuates any secondary electron emission from the substrate at a projectile energy of 2 MeV, regardless of the target material or density. A comparison of normalized doubly differential electron yields from 2 MeV proton interaction with 100 L ASW to simulated doubly differential electron yields from 2 MeV proton interaction with 20 nm liquid water is shown in Fig.69. The upper plot is a comparison of forward scattered electron yields and the lower plot is a comparison of backward scattered electron yields. One important distinction that must be made involves the way in which these electron yield measurements were made. The angles noted to be measured by experiment are the scaled yields from a solid angle formed by the entrance collimator of the TOF detector, while the simulation electron yields are events binned within a conical shell solid angle defined by a range of 10°. Angular comparisons are color coordinated in the plots for visual aid. The same characteristic autoionization peaks seen in experimental yields were present in the simulation. The same expected decrease in yields approaching 90° from both sides was also observed for both experiment and simulation. The region of highest interest in this comparison is from 1 - 100 eV. Experiment and simulation show agreement at around 70 eV, but diverge for lower energy electron yields. The simulation showed a higher yield for 1 - 70 eV electrons by about an order of magnitude on average. It is unclear if the simulation overestimates low energy electron yields or the experiment under measured electron yields in this range.

Relative doubly differential electron yields from 2 MeV proton irradiation during 5 - 400 L ASW buildup on GNP film were measured and are shown in Fig.70. The axes have been scaled in order to zoom the spectra for visual aid. Spectra taken during the buildup to 100 L are shown as darkening shades of red, the 100 L spectrum is colored neon green, and buildup over 100 L are shaded blue to match the color scheme in Fig.64, from forward scattered buildup tests on gold foil. The increase in low energy electron yields from increased monolayers of ASW up to 100 L observed during forward scatted gold foil buildup tests was not observed for GNP film. Although, the gradual attenuation of electron yields were

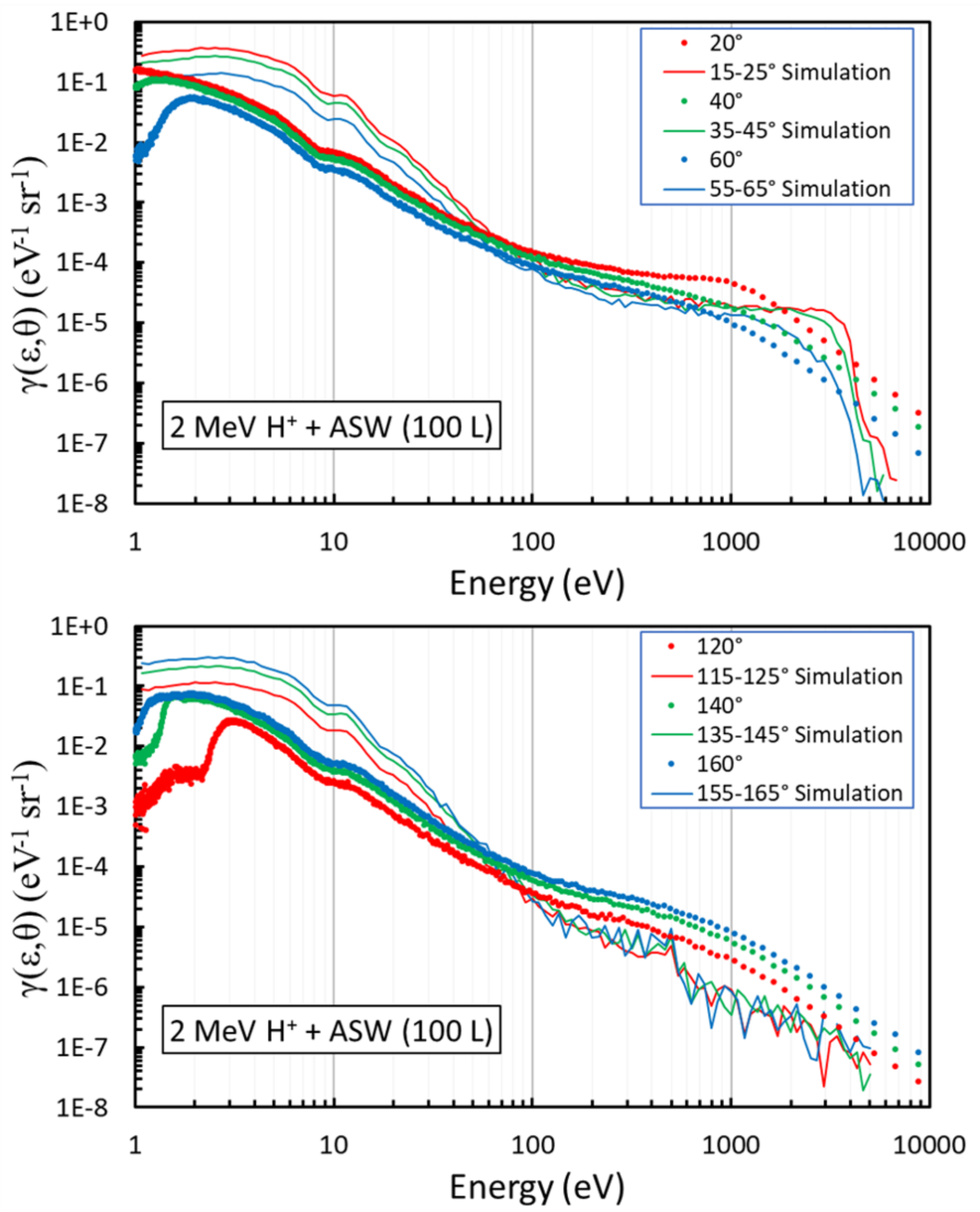

Figure 69: Shown is a comparison to simulation for doubly differential electron yields from protons on ASW. Forward (top) and backward (bottom) scattered angles are shown, with disagreement in both the low and high energy electron ranges.

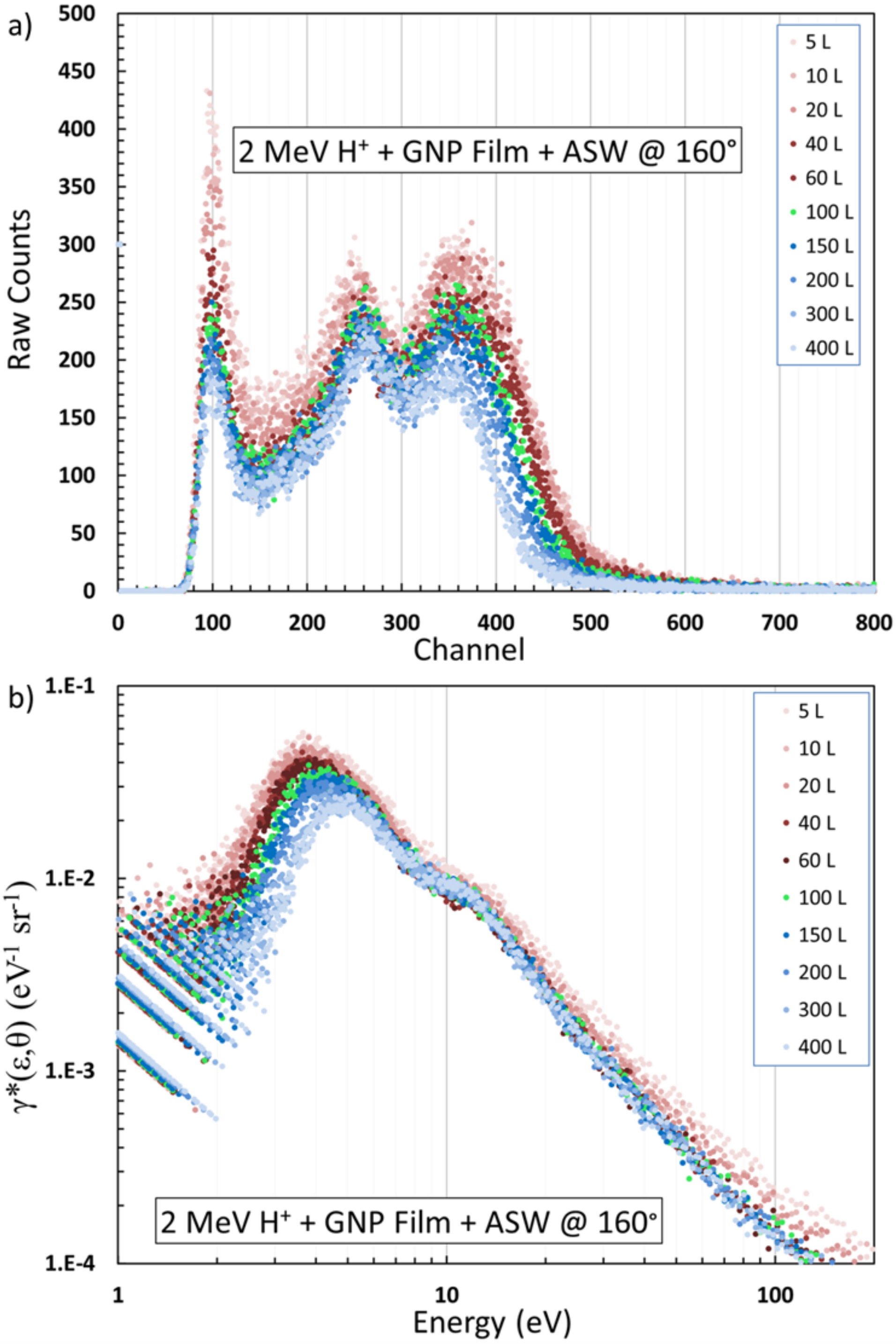

Figure 70: Raw count spectra (a) and relative doubly differential electron emission yields (b) from amorphous solid water buildup on GNP film. Measurements were made from 5 - 400 L and colored to visually match Fig.64.

observed over all energy ranges, similar to the gradual attenuation seen in the high energy (> 8 eV) region of Fig.64. Comparing this rate of attenuation from known thicknesses of ASW on GNPs could prove useful in testing more complex PARTRAC simulation configurations including amorphous GNP lattice environments.

3.5.2 Carbon Ions on ASW

Relative doubly differential electron yields from carbon ion interactions with 100 L ASW were measured for carbon ion projectiles of incident energy 2.4 and 6 MeV. These relative yields were normalized using the calculated scaling factor found from the normalization of carbon ion interactions with gold foil to total yields, as discussed previously. This scaling was applied to compensate for the overestimation in yields of the TOF detector acceptance solid angle and any unknown electronics or detector efficiencies inherent in the experimental design. Plots of forward scattered and back scattered doubly differential electron yield measurements made for 2.4 and 6 MeV proton interactions with 100 L ASW are shown in Fig.71 and Fig.72 respectively. A dramatic decline in high energy electron yields was observed for 2.4 MeV carbon ion on ASW spectra, similar to the carbon ion on gold foil spectra. An energy comparison for carbon ion interactions with ASW is shown in Fig.73. The expected trend of increasing low energy electron yields with decreasing projectile energy was not observed in this comparison. Due to the lack of high energy electron yields and relatively low low-energy electron yields in the 2.4 MeV carbon ion on ASW spectra, consideration should be taken when using this data for future comparisons to simulation. These suspicious characteristics may be due to a flaw in the experimental design or an artifact of near Bragg peak energy projectiles in general.

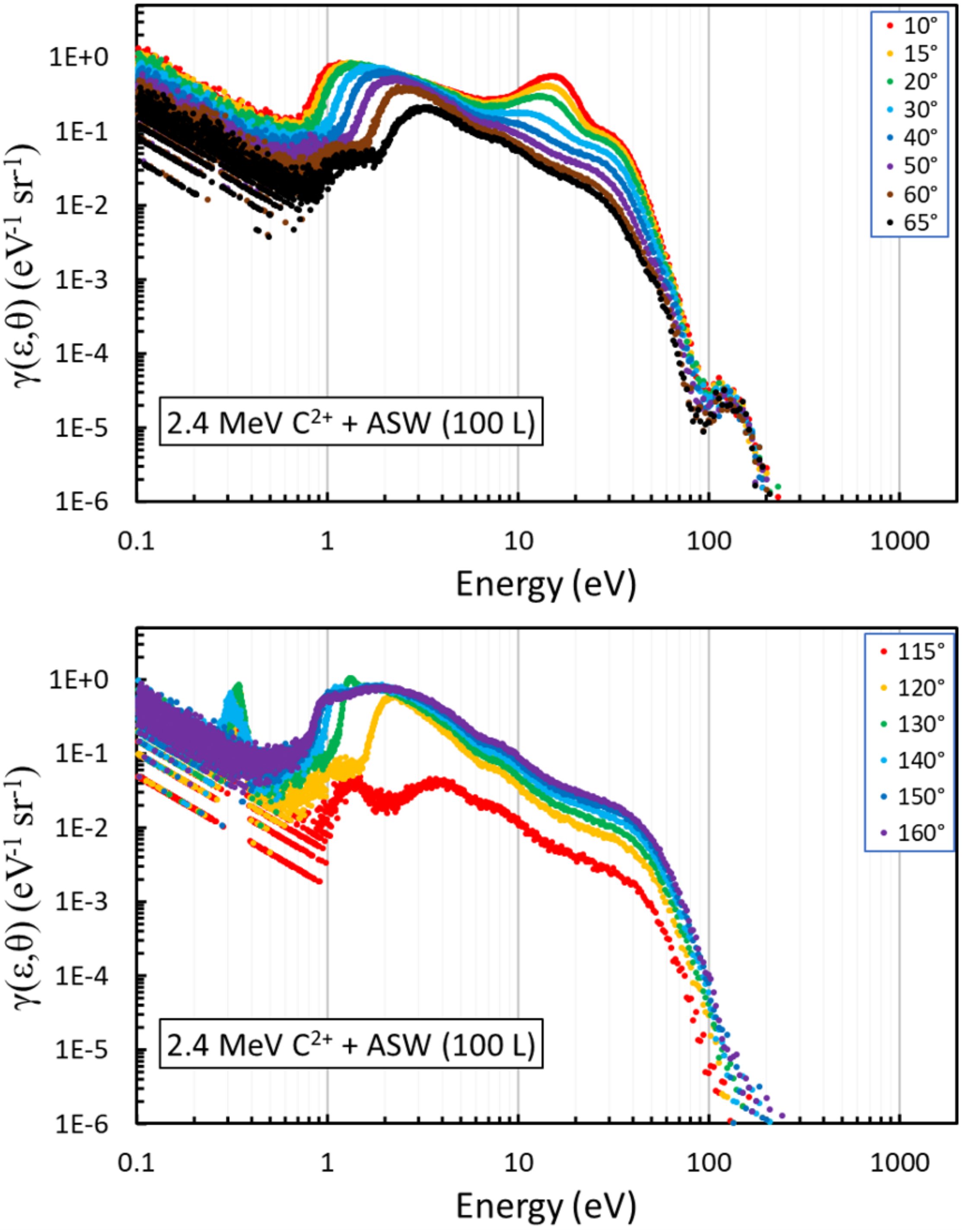

Figure 71: Doubly differential electron yields from 2.4 MeV carbon ion interactions with 100 L amorphous solid water. Forward (top) and backward (bottom) scattered angles are normalized to total electron yields from gold foil.

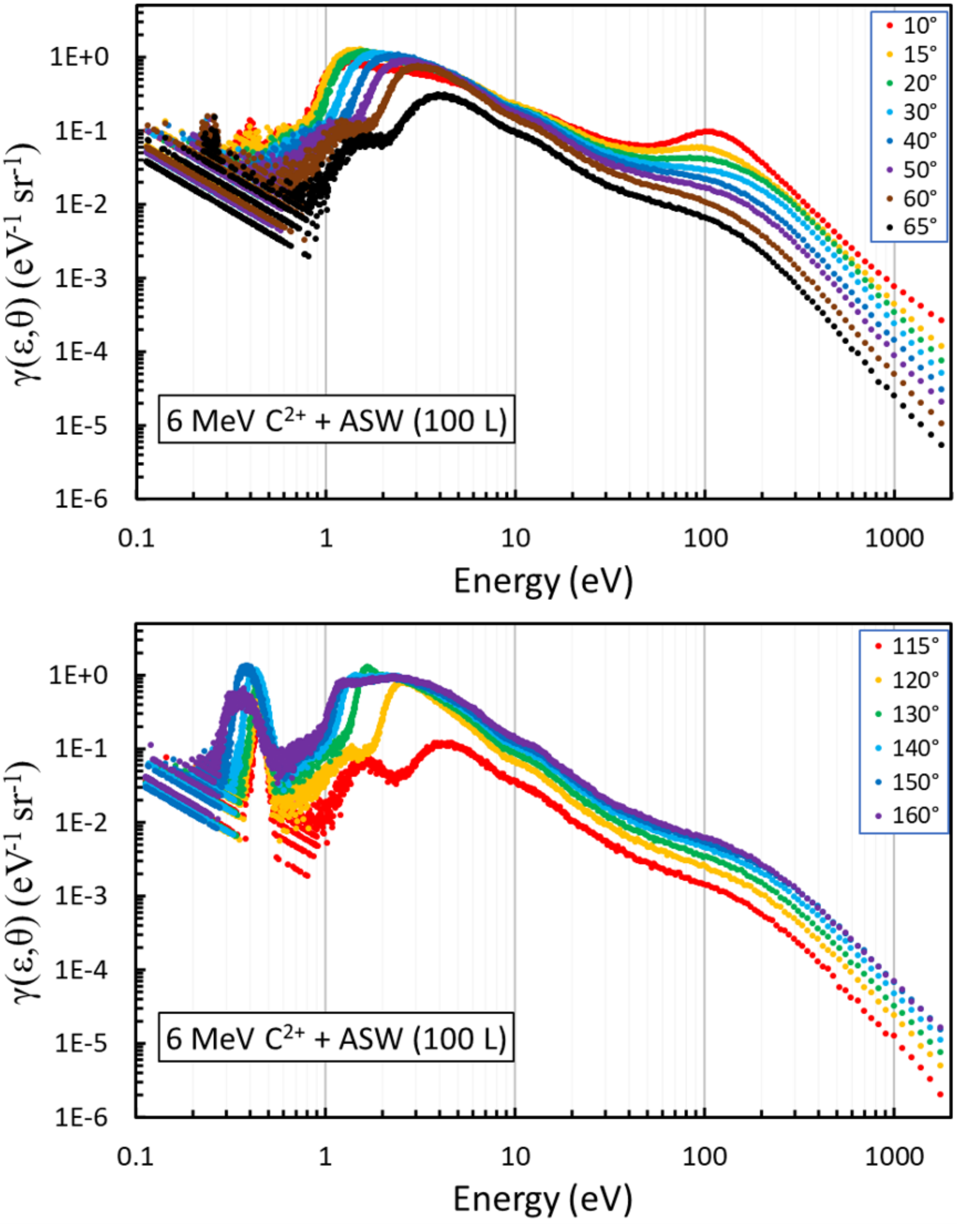

Figure 72: Doubly differential electron yields from 6.0 MeV carbon ion interactions with 100 L amorphous solid water. Forward (top) and backward (bottom) scattered angles are normalized to total electron yields from gold foil.

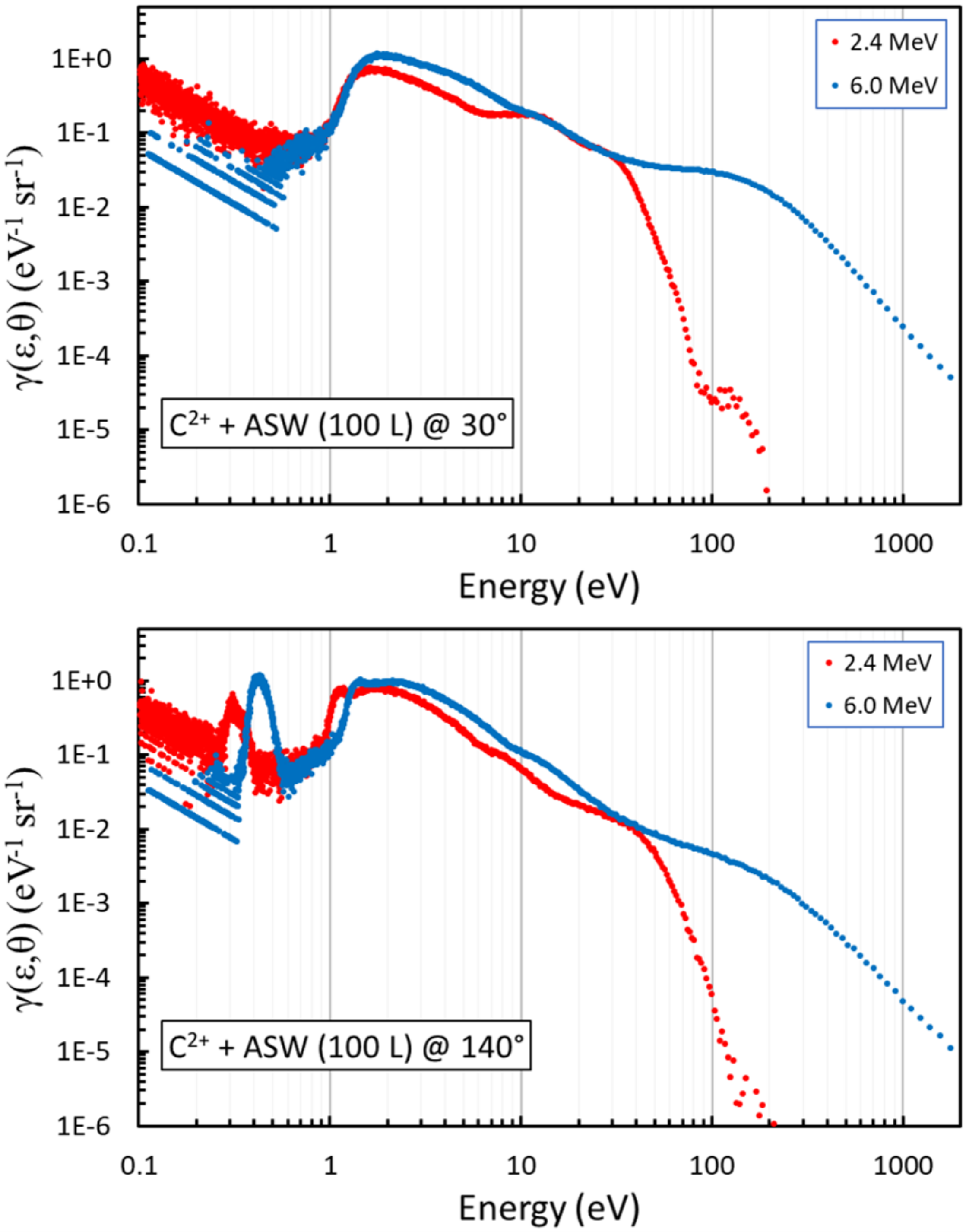

Figure 73: Doubly differential electron yield comparisons for 2.4 - 6.0 Mev carbon ion interactions with ASW at 30° (top) and 140° (bottom).

4 Conclusion

Doubly differential electron yields were measured for proton and carbon ion interactions with solid state targets for near Bragg-peak (0.2 - 4 MeV/AMU) projectile energy relevant to the study of ion therapy for the treatment of cancer. Low energy (1 - 100 eV) electron emission was precisely measured using time-of-flight analysis under ultra-high vacuum conditions. This study has served to establish a database of measurements to be used in comparison to Monte Carlo simulation outcomes.

Analysis of the proton on gold spectra shows a sharp drop in electron yields for electrons less than 1 eV, as expected. Electrons in this energy range are approaching thermal conditions and are highly influenced by stray electric and magnetic fields. Efforts were made to reduce stray magnetic fields in the UHV chamber by surrounding the area of interest with magnetic shielding metal and employing Helmholtz coils to cancel the vertical component of the earth's magnetic field. Further improvements could be made by precisely measuring horizontal magnetic fields and designing further field-canceling coils.

During normalization of doubly differential electron yields to previously measured total electron yields, spectra from small angles (< 20°) and angles near 90° (65 - 115°) were excluded. This is due to the inability of the TOF detector to distinguish between secondary electrons, convoy electrons, binary encounter electrons, and scattered projectiles. Scattered projectile peaks were seen in all forward scattered spectra in the 0 - 20° range. Also, spectra in the 65 - 115° range were considered unusable in normalization efforts due to the limiting design of the target assembly. A decreased yield in this range is to be expected as the beveled edge of the copper plates holding the foils prevent electrons from traversing extreme angles, creating a "shadow" around 90°.

Momentum-exchange driven binary-encounter electron peaks are seen in the 10 - 50 eV range for 1, 2, and 4 MeV proton interactions with gold foil. The resolution of these peaks will tend to be low as the TOF method results in lowered precision approaching 100 eV, as discussed previously. An increase in electron yields across all electron energies is seen for decreasing proton projectile energy as expected. This trend is in agreement with previously measured total yield measurements and is consistent with the dose-depth measurements made in ionization chambers and tissue samples for near Bragg-peak energy deposition.

Analysis of doubly differential electron yields for carbon ion interactions with gold foil showed a similar increase in low energy (< 10 eV) electron yields for decreasing carbon ion projectile energy, but a decrease in high energy (> 10 eV) electron yields for decreasing projectile energy. High energy (> 50 eV) electron yields from 2.4 MeV (0.2 MeV/AMU) carbon ion interactions fall off dramatically. A scattered projectile peak in the 200 eV range is apparant for forward scattered electron spectra, but is of low resolution and yield. This lack of high energy electron yields should be interpreted as an artifact of the low projectile incident energy, 0.2 MeV/AMU, of carbon ions in comparison to say the previously discussed low projectile energy, 1.0 MeV/AMU, proton interactions. This spectral feature could give insight into the proportion of low energy electrons to high energy electrons in the Bragg-peak energy range for ion interactions with matter. As these spectra were performed under the same experimental circumstances as the proton and other carbon ion projectiles on gold foil, the likelihood of this absence of high energy electrons may not be an artifact of experimental design.

Previously published total yield measurements showed little to no dependence in charge state for electron yields from carbon ion interactions. A comparison of 2+ and 3+ carbon ions at 6 MeV was performed and revealed subtle increases in electron yields for 3+ carbon ion interactions for multiple angles in the forward and backward direction. This is in contrast to the suggestion of Itoh that no difference in the 3+ carbon case should be expected. How much difference this would make in total yields is unclear and could be a parameter for investigation in future studies. A full investigation into the electron yields from a wide range of energies for singly ionized vs. bare carbon ions could be of clinical interest.

An investigation into the electron yields from gold nanostructures embedded onto the surface of silicon wafers provided insight into the low energy electron yield differences between amorphous gold matrix and clumped gold particle surfaces. An obvious increase in electron yields from the presence of gold nanoparticles across all electron energies was observed for both protons and carbon ions when compared to the silicon control. An angular distribution test for back scattered electrons from proton interactions was done for silicon control, 1.5% GNP, and 9.5% GNP targets to confirm the same decreasing electron yields approaching 90° seen in the foil measurements. The surface conditions for these targets were not optimal for investigating angular dependencies as the surfaces were etched and uneven from the manufacturing process, but an overall rough angular dependence was noted, showing evidence of similar surface conditions to previously used targets. An increase in electron yields across all electron energies for decreasing carbon ion projectile energy was observed as expected.

For both proton and carbon ion interactions with Si-GNPs, an increased low energy ($<$ 10 eV) yield was observed in comparison to the gold foil measurements. These observations should be considered carefully as the scaling done to normalized gold foil yields was a yield-based scaling at 100 eV, assuming the majority of high energy electron yields produced by either target are going to more heavily depend on the projectile energy than the target conditions. If this increased low energy electron yield observation for GNPs is an artifact of the surface conditions of gold nano structures, comparisons to simulation could provide insight into model improvements for the low energy electron cross section functions.

Further investigations into the electron yield from gold nanostructures led to the employment of GNP film on gold TEM grid substrates as a target material. This target material proved to be extremely difficult to work with as the 4 - 6 nm thick film was extremely fragile, easy to damage in handling, damaged by unpulsed beam, evaporated by argon sputtering gas, and dissolved under extreme heat. The high purity gold grid that acted as a substrate for this target could have contributed to a large amount of the electron yield spectra, but some interesting features were noted for this GNP film material. The presence of surface contaminates seemed to be inevitable as surface cleaning, even with neon gas, proved to cause sufficient target damage. Projectile energy dependency was tested and noted to be consistent with gold foil measurements when comparing 1, 2, and 4 MeV proton interactions as well as 2.4, 6, and 8 MeV carbon ion interactions. A similar high energy electron drop-off was observed for decreasing carbon ion energies similar to the gold foil experiments, providing a source of validation in the 2.4 MeV carbon ion on gold foil spectral features. In both proton and carbon ion interaction with GNP film spectra, an increase in low energy ($<$ 10 eV) electron yields was observed when yield-scaling to 100 eV, which is again consistent with the Si-GNP yield measurements.

Doubly differential electron yields from proton and carbon ion interactions with amorphous solid water were measured to provide direct comparison data to liquid water simulations and clinical applications. The optimal thickness of 100 L found in previous studies was tested and confirmed showing a decrease in high energy ($>$ 10 eV) electrons and an increase in low energy electrons ($<$ 10 eV) up to 100 L. A decrease in yields across all electron energies was noted from 100 to 400 L, including the low energy ($<$ 10 eV) range. This overall decrease in high energy electrons is believed to be attenuation of electrons generated inside of the gold foil substrate, while the increase in low energy electrons up to 100 L is believed to be due to the surface contamination effects seen in cleaning, while the decrease in low energy electron yields from 100 to 400 L is believed to be from surface charging effects.

An overall increase in doubly differential electron yields at all electron energies was observed for decreasing proton projectile energy in the forward and backward direction as expected. A simulation of this proton interaction spectrum for 2 MeV protons on 100 L amorphous solid water was performed at ECU and showed agreement in the 50 - 100 eV electron energy range. Disagreement in the electron yields at low energies is a matter of debate between experiment and theory, as it is unclear if experimental conditions are insufficient for measurement or low energy electron models are making over estimations. Amorphous solid water build up on GNP film was performed as a comparison test to gold foil substrate measurements and showed similar decreasing yield rates across high energy electrons, but did not show a local maximum around 100 L for low energy electrons.

Doubly differential electron yield measurements for carbon ion interactions with 100 L amorphous solid water showed similar spectral features when compared to gold foil measurements, but when normalized to carbon ion interactions on gold foil, showed a decrease in low energy electron yields with decreasing carbon ion projectile energy, which was not expected. This is in strong disagreement with near Bragg-peak dose distributions for carbon ion interaction measurements in liquid water.

Improvements that could be made for this investigation include further reduction of stray magnetic and electric fields inside the UHV chamber, improved target selection, and the use of electron spectroscopy techniques to measure high energy electrons with higher precision. Additional Helmholtz coils, designed to cancel out the horizontal components of stray magnetic fields, could improve the passage of low energy (< 1 eV) electrons. This improvement to low energy electron passage may lead to closer agreement with Monte Carlo simulation outputs. As a substitute for the GNP embedded in silicon target, a GNP embedded poly(methyl methacrylate) (PMMA) target could be used to more accurately simulate a GNP injected tumor site. PMMA is widely used as a phantom material in radiation dosimetry as the hydrocarbon distribution is very similar to human tissue. To further study the fundamental properties of GNPs with the use of films, a thicker target film should be manufactured that does not require the need for a grid substrate. In order to improve the resolution of high energy (> 100 eV) electron yields, measurement techniques involving electron spectroscopy, which is incapable of measuring low energy electrons, could offer precision measurements for the less prevalent but still important high energy electron production during ion interactions with matter.

References

1. Shinpaugh, J. *et al.* Electron Emission from Condensed Phase Material Induced by Fast Protons. *Radiation Protection Dosimetry* **143,** 135–138 (2011).
2. Toburen, L. *et al.* Electron Emission from Amporphous Solid Water Induced by Passage of Energetic Protons and Flourine Ions. *Radiation Research* **174,** 107–118 (2010).
3. McLawhorn, R. *Electron Emission from Condensed Phase Targets Induced by Fast Protons* PhD thesis (East Carolina University, 2008).
4. Wilson, R. R. Radiological use of fast protons. *Radiology* **47,** 487–491 (1946).
5. Kamada, T. Twenty years of carbon ion radiation therapy at the national institute of radiological sciences: accomplishments and prospects. *International journal of particle therapy* **2,** 459–463 (2015).
6. Operative Group, P. T. C. Facilities in Operation. *www.ptcog.ch* (2021).
7. Alvarado, F., Bari, S., Hoekstra, R. A. & Schlathölter, T. A. Interactions of neutral and singly charged keV atomic particles with gas-phase adenine molecules. *The Journal of chemical physics* **127** (2007).
8. Tabet, J. *et al.* Absolute total and partial cross sections for ionization of nucleobases by proton impact in the Bragg peak velocity range. *Physical review. A, Atomic, molecular, and optical physics* **82** (2010).
9. Toburen, L. H. & Wilson, W. E. Time-of-flight measurements of low-energy electron energy distributions from ion–atom collisions. *Review of scientific instruments* **46,** 851–854 (1975).
10. Toburen, L. H. *et al.* Charge transfer and ionisation by intermediate-energy heavy ions. *Radiation protection dosimetry* **122,** 22–25 (2006).
11. Bondarev, A. I., Kozhedub, Y. S., Tupitsyn, I. I., Shabaev, V. M. & Plunien, G. Doubly differential cross sections for ionization of lithium atom by protons and O8+ ions. *The European physical journal. D, Atomic, molecular, and optical physics* **73,** 1–7 (2019).
12. Edwards, J. L. & Thomas, E. W. Emissions from a molecular hydrogen target induced by the impact of fast protons. *Physical review* **165,** 16–17 (1968).
13. Baragiola, R., Alonso, E., Ferron, J. & Oliva-Florio, A. Ion-induced electron emission from clean metals. *Surface Science* **90,** 240–255. ISSN: 0039-6028 (1979).
14. Baragiola, R. A., Alonso, E. V. & Florio, A. O. Electron emission from clean metal surfaces induced by low-energy light ions. *Physical review. B, Condensed matter* **19,** 121–129 (1979).
15. Benka, O., Steinbauer, E. & Bauer, P. Kinetic electron emission yield induced by H+ and He2+ ions versus stopping power for Al, Cu, Ag and Au. *Nuclear instruments and methods in physics research. Section B, Beam interactions with materials and atoms* **90,** 64–66 (1994).
16. Benka, O., Schinner, A., Fink, T. & Pfaffenlehner, M. Electron-emission yield of Al, Cu, and Au for the impact of swift bare light ions. *Physical review. A, Atomic, molecular, and optical physics* **52,** 3959–3965 (1995).

17. Benka, O., Pfaffenlehner, M. & Schinner, A. Electron emission yield of Al, Cu, and Au targets induced by fast hydrogen and helium ions. *Nuclear instruments and methods in physics research. Section B, Beam interactions with materials and atoms* **117,** 350–356 (1996).

18. Benka, O., Pürstinger, J. & Koyama, A. Kinetic electron emission from Al, Cu, and Au surfaces exposed to oxygen. *Physical review. A, Atomic, molecular, and optical physics* **58,** 2978–2984 (1998).

19. Christou, C. I. *Electron emission from condensed phase targets by 2-MeV proton impact* PhD thesis (East Carolina University, 2004).

20. Da Silveira, E. F. & Jeronymo, J. M. F. Secondary electron emission from the entrance and exit surfaces of thin aluminium foils under fast light ion bombardment. *Nuclear instruments and methods in physics research. Section B, Beam interactions with materials and atoms* **24,** 534–537 (1987;1986;).

21. Hasselkamp, D., Lang, K. G., Scharmann, A. & Stiller, N. Ion induced electron emission from metal surfaces. *Nuclear instruments and methods* **180,** 349–356 (1981).

22. Hasselkamp, D., Hippler, S. & Scharmann, A. Ion-induced secondary electron spectra from clean metal surfaces. *Nuclear instruments and methods in physics research. Section B, Beam interactions with materials and atoms* **18,** 561–565 (1986).

23. Hespeels, F. *et al.* Backscattered electron emission after proton impact on gold nanoparticles with and without polymer shell coating. *Physics in medicine and biology* **64,** 125007–125007 (2019).

24. Obata, F., Majima, T., Hamamoto, Y., Yogo, A. & Itoh, A. Secondary Electron Emission Statistics by Fast Molecular Ion Impact. Japanese. *Meeting Abstracts of the Physical Society of Japan,* 89 (2001).

25. Itoh, A., Majima, T., Obata, F., Hamamoto, Y & Yogo, A. Secondary electron emission from Au by medium energy atomic and molecular ions. *Nuclear Instruments and Methods in Physics Research Section B: Beam Interactions with Materials and Atoms* **193,** 626–631 (2002).

26. Koyama, A., Shikata, T. & Sakairi, H. Secondary electron emission from al, cu, ag, and au targets under proton bombardment. *Japanese Journal of Applied Physics* **20,** 65–70 (1981).

27. Sato, Y. *et al.* Projectile charge dependence of electron emission from foils. English. *Physical review. A, Atomic, molecular, and optical physics* **61,** 529011–529016 (2000).

28. Koyama, A. Contribution of Directly Excited Electrons to the Secondary Electron Emission From Al by High Energy Proton or Alpha-particle Bombardment. English. *Japanese Journal of Applied Physics* **16,** 431–440 (1977).

29. Koyama, A., Yagi, E. & Sakairi, H. Secondary Electron Emission from Ni and Al by High-Energy Proton and alpha-Particle Bombardment. English. *Japanese Journal of Applied Physics, Part 1: Regular Papers and Short Notes and Review Papers* **15,** 1811–1812 (1976).

30. Suszcynsky, D. M. & Borovsky, J. E. Secondary-electron emission from metals impacted by high-velocity particles: molecular-effect deviations from a single-particle picture. *Nuclear instruments and methods in physics research. Section B, Beam interactions with materials and atoms* **53,** 255–266 (1991).

31. Lei, J., Zhu-Ying, Z. & Guo-Qing, Z. Backward Secondary Electron Emission Yield of Thick Targets Induced by MeV Ions. *Chinese physics letters* **17,** 691–693 (2000).

32. Baragiola, R., Shi, M., Vidal, R. & Dukes, C. Fast proton-induced electron emission from rare-gas solids and electrostatic charging effects. *Physical Review B - Condensed Matter and Materials Physics* **58,** 13212–13218 (1998).

33. Clouvas, A. *et al.* Role of projectile electrons in secondary electron emission from solid surfaces under fast-ion bombardment. *Physical review. B, Condensed matter* **55,** 12086–12098 (1997).

34. Drexler, C. G. & DuBois, R. D. Energy- and angle-differential yields of electron emission from thin carbon foils after fast proton impact. *Physical review. A, Atomic, molecular, and optical physics* **53,** 1630–1637 (1996).

35. DuBois, R. & Drexler, C. Differential Electron Emission from Solids and Frozen Gases. *Proceedings of the 17th Werner Brandt Workshop on the Penetration of Charged particles in Matter,* 95–104 (1997).

36. Mechbach, W., Braunstein, G. & Arista, N. Secondary-electron emission in the backward and forward directions from thin carbon foils traversed by 25-250 keV proton beams. *Journal of physics. B, Atomic and molecular physics* **8,** L344–L349 (1975).

37. Ogawa, H., Sorai, K., Amano, S., Ishii, K. & Kaneko, T. Forward-backward correlated secondary-electron emission depending on the angle of emergence of protons transmitted through a thin carbon foil. *Journal of physics. B, Atomic, molecular, and optical physics* **47,** 85201 (2014).

38. Shinpaugh, J. L., Toburen, L. H. & Justiniano, E. L. B. Fluorine Auger-electron production in collisions of H+ and Li2+ with fluorocarbon targets. *Physical review. A, Atomic, molecular, and optical physics* **60,** R4213–R4216 (1999).

39. Scifoni, E., Surdutovich, E. & Solov'yov, A. V. Spectra of secondary electrons generated in water by energetic ions. *Physical Review E* **81,** 021903 (2010).

40. Kreipl, M., Friedland, W. & Paretzke, H. Interaction of ion tracks in spatial and temporal proximity. *Radiation and Environmental Biophysics* **48,** 349–59 (Nov. 2009).

41. Bragg, W. & Kleeman, R. On the ionization curves of radium. *The London, Edinburgh, and Dublin Philosophical Magazine and Journal of Science* **8,** 726–738 (1904).

42. Brown, A. & Suit, H. The centenary of the discovery of the Bragg peak. *Radiotherapy and Oncology* **73,** 265–268 (2004).

43. Gerweck, L. E. & Kozin, S. V. Relative biological effectiveness of proton beams in clinical therapy. *Radiotherapy and oncology* **50,** 135–142 (1999).

44. Blomquist, E. *et al.* Relative biological effectiveness of intermediate energy protons. Comparisons with 60Co gamma-radiation using two cell lines. *Radiotherapy and Oncology* **28,** 44–51 (1993).

45. Tang, J. *et al.* Comparison of radiobiological effective depths in 65-MeV modulated proton beams. *British journal of cancer* **76,** 220–225 (1997).

46. Levy, R., Schulte, R., Miller, J. S. D. & Slater, J. Stereotactic Radiosurgery: The Role of Charged Particles. *Acta Oncologica* **38,** 165–169 (1999).

47. Health, S. Bragg Peak and the Proton Difference. *https://www.scripps.org/services/cancer-care__proton-therapy/what-is-proton-therapy__bragg-peak* (11-6-2017).

48. Tsujii, H. *et al.* Carbon-ion radiotherapy. *Carbon-ion radiotherapy. Springer* (2014).

49. Kamada, T. *et al.* Carbon ion radiotherapy in Japan: an assessment of 20 years of clinical experience. *The Lancet Oncology* **16,** e93–e100 (2015).

50. Shinoto, M. *et al.* Carbon ion radiation therapy with concurrent gemcitabine for patients with locally advanced pancreatic cancer. *International Journal of Radiation Oncology* Biology* Physics* **95,** 498–504 (2016).

51. Okada, T. *et al.* Carbon Ion Radiotherapy in Advanced Hypofractionated Regimens for Prostate Cancer: From 20 to 16 Fractions. *International Journal of Radiation Oncology*Biology*Physics* **84,** 968–972 (2012).

52. Durante, M., Orecchia, R & Loeffler, J. Charged-particle therapy in cance:clinical uses and futer perspectives. *Clinical Oncology* **14,** 483–495 (2017).

53. Her, S., Jaffray, D. A. & Allen, C. Gold nanoparticles for applications in cancer radiotherapy: Mechanisms and recent advancements. *Advanced drug delivery reviews* **109,** 84–101 (2017).

54. Singh, P. *et al.* Gold nanoparticles in diagnostics and therapeutics for human cancer. *International journal of molecular sciences* **19,** 1979 (2018).

55. Yeh, Y.-C., Creran, B. & Rotello, V. M. Gold nanoparticles: preparation, properties, and applications in bionanotechnology. *Nanoscale* **4,** 1871–1880 (2012).

56. Nagi, N., Khair, Y. & Abdalla, A. Capacity of gold nanoparticles in cancer radiotherapy. *Japanese Journal of Radiology* **35,** 555–561 (2017).

57. Shrestha, S., Cooper, L. N., Andreev, O. A., Reshetnyak, Y. K. & Antosh, M. P. Gold nanoparticles for radiation enhancement in vivo. *Jacobs journal of radiation oncology* **3** (2016).

58. Zhang, X.-D. *et al.* Size-dependent radiosensitization of PEG-coated gold nanoparticles for cancer radiation therapy. *Biomaterials* **33,** 6408–6419 (2012).

59. Samadian, H., Hosseini-Nami, S., Kamrava, S. K., Ghaznavi, H. & Shakeri-Zadeh, A. Folate-conjugated gold nanoparticle as a new nanoplatform for targeted cancer therapy. *Journal of cancer research and clinical oncology* **142,** 2217–2229 (2016).

60. Yang, C., Neshatian, M., van Prooijen, M. & Chithrani, D. B. Cancer nanotechnology: enhanced therapeutic response using peptide-modified gold nanoparticles. *Journal of nanoscience and nanotechnology* **14,** 4813–4819 (2014).

61. Hu, C., Niestroj, M., Yuan, D., Chang, S. & Chen, J. Treating cancer stem cells and cancer metastasis using glucose-coated gold nanoparticles. *International journal of nanomedicine* **10,** 2065 (2015).

62. Chen, Y., Yang, J., Fu, S. & Wu, J. Gold Nanoparticles as Radiosensitizers in Cancer Radiotherapy. *International Journal of Nanomedicine* **15,** 9407 (2020).

63. Chithrani, D. B. *et al.* Gold nanoparticles as radiation sensitizers in cancer therapy. *Radiation research* **173,** 719–728 (2010).

64. Chang, M.-Y. *et al.* Increased apoptotic potential and dose-enhancing effect of gold nanoparticles in combination with single-dose clinical electron beams on tumor-bearing mice. *Cancer science* **99,** 1479–1484 (2008).

65. Wang, C., Jiang, Y., Li, X. & Hu, L. Thioglucose-bound gold nanoparticles increase the radiosensitivity of a triple-negative breast cancer cell line (MDA-MB-231). *Breast cancer* **22,** 413–420 (2015).

66. Liu, Y. *et al.* The dependence of radiation enhancement effect on the concentration of gold nanoparticles exposed to low-and high-LET radiations. *Physica Medica* **31,** 210–218 (2015).

67. Hainfeld, J. F., Slatkin, D. N. & Smilowitz, H. M. The use of gold nanoparticles to enhance radiotherapy in mice. *Physics in Medicine & Biology* **49,** N309 (2004).

68. Liu, S. *et al.* Radiosensitizing effects of different size bovine serum albumin-templated gold nanoparticles on H22 hepatoma-bearing mice. *Nanomedicine* **13,** 1371–1383 (2018).

69. Mozumder, A & Hatano, Y. *Charged particle and photon interactions with matter: chemical, physicochemical, and biological consequences with applications* (CRC press, 2003).

70. Ziegler, J. Stopping of energetic light ions in elemental matter. *Journal of applied physics* **85,** 1249–1272 (1999).

71. Ziegler, J. F., Biersack, J. P. & Littmark, U. *The Stopping and Range of Ions in Solids* (Pergamon, New York, 1985).

72. Ziegler, J. F., Ziegler, M. D. & Biersack, J. P. SRIM–The stopping and range of ions in matter (2010). *Nuclear Instruments and Methods in Physics Research Section B: Beam Interactions with Materials and Atoms* **268,** 1818–1823 (2010).

73. Rothard, H. *et al.* Secondary-electron velocity spectra and angular distributions from ions penetrating thin solids. *Nuclear Instruments and Methods in Physics Research Section B: Beam Interactions with Materials and Atoms* **48,** 616–620 (1990).

74. Frischkorn, H. *et al.* Ion induced electron ejection from solids. *Nuclear Instruments and Methods in Physics Research* **214,** 123–128 (1983).

75. Ferry, J. Recent developments in electrostatic accelerator technology at NEC. *Nuclear Instruments and Methods in Physics Research Section A: Accelerators, Spectrometers, Detectors and Associated Equipment* **328,** 28–33. ISSN: 0168-9002 (1993).

76. Middleton, R. *A Negative-Ion Cookbook* (Department of Physics, University of Pennsylvania, 1989).

77. Norton, G. New developments in design and applications for pelletron accelerators. *Pramana* **59,** 745–751 (2002).

78. Van de Graff, R. Tandem Electrostatic Accelerators. *Nuclear Instruments and Methods* **8** (1960).

79. Wiza, J. Microchannel plate detectors. *Nuclear Instruments and Methods* **162,** 587–601 (1979).

80. Mallory, G. & Tibbets, K. One-step femtosecond laser ablation synthesis of sub-3 nm gold nanoparticles stabilized by silica. *Applied Surface Science* **475,** 1048–1057 (2019).

81. Fojtik, A. & Henglein, A. Laser ablation of films and suspended particles in a solvent : formation of cluster and colloid solutions. *Phys. Chem.* **97,** 252–255 (1993).

82. Allred, D. *et al.* Direct nanofabrication and transmission electron microscopy on a suite of easy-to-prepare ultrathin film substrates. *Thin Solid Films* **515,** 5341–5347 (2007).

83. Allred, D. & Schwartz, D. Unsupported, electron transparant films and related methods. *U.S. Patent 7 348 570* (March 25, 2008).

84. Masel, R. *Principles of adsorption and reaction on solid surfaces* (John wiley and Sons Inc., 1996).

85. Dingfelder, M. Personal communication.

86. Dingfelder, M., Travia, A., McLawhorn, R. A., Shinpaugh, J. L. & Toburen, L. H. Electron emission from foils and biological materials after proton impact. *Radiation Physics and Chemistry* **77,** 1213–1217 (2008).

87. Alloni, D., Campa, A., Friedland, W., Mariotti, L. & Ottolenghi‘, A. Track structure, radiation quality and initial radiobiological events: Considerations based on the PARTRAC code experience. *International journal of radiation biology* **88,** 77–86 (2012).

88. Townsend, L. W. Secondary Electron Spectra from Charged Particle Interactions. *Radiation Research* **147,** 273–273 (1997).

89. Schou, J. Secondary electron emission from solids by electron and proton bombardment. *Scanning Microscopy* **2,** 607–632 (1988).

90. Carlson, N. *Protection and Sensitization of Humal Cells to Proton Radiation by Cerium Oxide Nanoparticles* PhD thesis (East Carolina University, 2017).